Department of Energy
Washington, D.C. 20545

Docket No. 50-537
HQ:S:82:090

SEP 8 1982

Mr. Paul S. Check, Director
CRBR Program Office
Office of Nuclear Reactor Regulation
U.S. Nuclear Regulatory Commission
Washington, D.C. 20555

Dear Mr. Check:

RESPONSES TO REQUEST FOR ADDITIONAL INFORMATION

Reference: Letters, P. S. Check to J. R. Longenecker, "CRBRP Request for Additional Information," dated April 9, April 30, and June 21, 1982

This letter formally responds to your request for additional information contained in the reference letters.

Enclosed are responses to Questions CS 421.37, 38, and 57, and CS 760.99, 178, and 179 which will also be incorporated into a future PSAR amendment.

Sincerely,

John R. Longenecker

John R. Longenecker
Acting Director, Office of the
Clinch River Breeder Reactor
Plant Project
Office of Nuclear Energy

D001

Enclosures

cc: Service List
Standard Distribution
Licensing Distribution

Question CS421.37

Discuss the provisions made for alarming a zero or negative differential pressure (PSAR Section 7.5.5.2.1) as to sensor type, location, setpoints, testability, and annunciation.

Response

The intermediate loop pressure to primary loop pressure is maintained at presssures greater than 10 psi. When the pressure on the intermediate loop drops to within 10 psi of the primary loop, the operator is alerted by an alarm. The alarm is on a positive pressure differential and not zero or negative pressure differential.

Each instrument channel includes provisions for insertion of a test signal on the sensor side of the signal conditioning electronics.

The sensor type, locations, setpoints and annunciation are described in PSAR Section 7.5.2.1.1. PSAR Pages 7.5-7, 7.5-8, 7.5-27 have been modified for clarification.

provide the required time response. The thermowell is also swaged at the tip. The thermocouples are spring loaded against the bottom of the well. Although failures of the wells are not expected, as confirmed by tests and analysis, the head of the thermowell, including the cable penetration, is sealed to provide a secondary boundary for the sodium. Tests have shown that this system will provide a time response less than 5 seconds. Flexible mica, polyimide and fiberglass insulated thermocouple extension wires in conduit are used to bring the signals out of the Heat Transport System Cell. The signals are then routed to the containment mezzanine into reference junctions and signal conditioning equipment. The conditioned signals are transmitted to the control room for the Reactor Shutdown System logic. The Reactor Shutdown System provides buffered signals to the PCS and PDH & DS.

Primary and Intermediate Hot and Cold Leg Temperature

The primary and intermediate hot and cold leg temperatures are measured to determine and record operating conditions and to calorimetrically calibrate the permanent magnet flowmeters. The measurement is made by two duplex element resistance temperature detectors (RTDs) per loop, installed in thermowells. Although failures of the wells are not expected, as confirmed by tests and analysis, the head of the thermowell, including the cable penetration, is sealed to provide a secondary boundary for the sodium. The signals from the RTDs are routed to signal conditioning equipment which converts the resistance variation to a standard signal level for transmission to the PDH & DS.

Primary and Intermediate Pump Discharge Pressure

The primary and intermediate pump discharge pressure measurements monitor pump performance. In addition the primary pump outlet in conjunction with the intermediate IHX outlet pressure provide the primary loop/intermediate loop differential pressure. The measurements are made by pressure elements installed in the elevated section of the drain line from the discharge piping of the sodium pump. NaK filled capillaries from the pressure elements are connected to pressure transducers which develop electrical signals proportional to the pressure. These pressure transducers provide a secondary boundary if the bellows in the pressure elements should fail. The conditioned signal is supplied to the PDH & DS. Since this pressure element is located in an inerted cell and replacement would require entry into the cell and draining of the loop, two pressure elements per loop are provided.

Intermediate IHX Outlet Pressure

The intermediate IHX outlet pressure measurement is used to monitor the loop and IHX operational performance history. The measurements are made by pressure elements installed in the intermediate loop piping between the IHX and the superheater. NaK filled capillaries from the pressure elements are connected to pressure tranducers which develop electrical signals proportional to the pressure. The pressure transducers provide a secondary boundary if the bellows in the pressure elements should fail. The conditioned signal is supplied to the PDH and DS.

IHX Differential Pressure

The primary sodium pump discharge pressure and the IHX Intermediate Loop outlet pressure detectors are used to provide a differential measurement of the IHX Primary/Intermediate pressure difference , which is maintained above 10 psi during normal operating conditions. The differential pressure measurement is alarmed if the intermediate loop pressure drops to 10 psi above the primary loop pressure to alert the operator for corrective action to assure intermediate to primary differential pressure is maintained above the minimum required.

Intermediate Pump Inlet Pressure

The intermediate pump inlet pressure measurements provide a signal to monitor pump performance. Used with the pump outlet pressure, the differential pressure across the pump is obtained. In the primary loop, the reactor pressure is used for this surveillance. The measurements are made by pressure elements installed on the piping between the evaporators and the pump inlet. NaK filled capillaries from the pressure elements are connected to pressure transducers which develop electrical signals proportional to the pressure. The pressure transducers provide a secondary boundary if the bellows in the pressure elements should fail. The conditioned signal is supplied to the PDH & DS.

Intermediate Expansion Tank Level

Two separate level measurement channels are provided; both channels are used for indication in the control room and DH & DS and for alarm. Alarm channels provide a broad range measurement that covers possible high and low levels during plant operation as well as the IHTS fill level. The PDH & DS uses measurements for intermediate loop sodium inventory (see also Section 7.5.5). The level probes are designed to be replaceable.

Evaporator Sodium Outlet Temperature

Three thermocouple (as described above in the paragraph on IHX outlet temperature) channels are provided to measure the sodium temperature at the outlet of the evaporators in each loop. The thermocouples are placed just after the pipes from each evaporator join to form two single lines. These three signals are conditioned separately and provided to the Reactor Shutdown System logic. The Reactor Shutdown System in turn provides buffered signals to the PDH & DS.

7.5.2.1.2 Sodium Pumps

Sodium Level

Sodium level is measured in each pump tank. The signal provides indication and alarm. The alarm is used to notify the operator of abnormal operation and allow initiation of action to prevent pump damage. The signal is also provided to the PDH & DS where it can be used in calculation of sodium inventory.

leaks (<1 gm/hr) will be detected by annuli monitors in several days. Tests during 1975 and 1976 showed that under environmental conditions typical of LMFBR operation, small leaks from typical piping configurations can be detected by both Sodium Ionization and Plugging Filter Aerosol Detectors. Continuity (cable or contact) detectors did not reliably detect small pipe leaks under these conditions. Testing in 1978 verified the performance of aerosol detectors using prototypic CRBRP cell atmosphere recirculation as well as pipe/insulation design.

It is deduced from the test results that the sodium vapor/aerosol systems will, in conjunction with existing radiation monitoring technology, provide adequate indication of the smallest sizes of leaks of interest.

Sodium Leaks into an Air Atmosphere

Test results (Reference 2) indicate that the methods applicable to sodium leaks in inerted cells will also operate when applied in an air atmosphere. The additional use of smoke detectors and the accessibility of piping located in an air atmosphere to visual inspection assist in the selection of an effective sodium-to-air leak detection system.

7.5.5.2 Intermediate to Primary Heat Transport System Leak Detection

7.5.5.2.1 Design Description

The IHTS pressure (see 7.5.2.1.1 for instrument details) is maintained at least 10 psi higher than the Primary Heat Transport System at the IHX to prevent radioactive primary sodium from entering the IHTS in the event of a tube leak. Maintaining a positive pressure differential across the IHX is a limiting condition for operation of the plant (Chapter 16 - Technical Specifications). This provides assurance that a zero or negative differential will not exist during any extended interval. A loss of this pressure or a reversal of it is not expected to occur except during accident conditions. Such an occurance would necessitate an orderly plant shutdown to correct the problem. Since a reverse differential cannot occur for a significant interval, the potential leakage of primary sodium into the intermediate system, through an IHX tube leak, is small.

Leakage of primary sodium into the IHTS, should it occur, will be detected by radiation monitors provided on the IHTS piping within the SGB. The radiation monitor system will provide an indication of the radiation level and will provide alarms for conditions of excessive radiation indicative of ingress of primary sodium. Since the only activity expected in the IHTS is a low level of tritium, the radiation monitors will be very sensitive to the presence of significant amounts of radioactive primary sodium in the intermediate system. For accidents which involve a loss of IHTS boundary integrity the radiological effects have been evaluated. The results of these evaluations are presented in Sections 15.3.2.3, 15.3.3.3 and 16.6.1.5.

Question CS421.38

Section 7.4.2.1.4 of the PSAR states: "Control interlocks and operator overrides associated with the operation of the superheater outlet isolation valves have not been completely defined." Have these interlocks and overrides now been defined?

Response

The need for control interlocks and operator overrides is currently being reviewed and a Project position will be reflected in the PSAR in November 1982.

Question CS421.57

PSAR Section 7.7.1.5 discusses steam drum water level control. Discuss the operation of this control system. Include information on what consequences (i.e., overfilling the steam generator system and causing water flow into the steam piping, etc.) might result from a steam generator level control channel failure.

Be sure to discuss hi-hi (12 inches) steam generator level logic for main feedwater isolation.

Response:

PSAR Section 7.7.1.5 has been updated in response to this question.

The control system for the purpose of responding to this question is subdivided into three parts. These are:

- o Input signals
- o level control circuit
- o control valve.

The steam drum level control circuit has a three element (steam flow, feedwater flow and steam drum level) controller and a median select module for each of the three redundant measurement channels for each input signal.

Failure of one of the input signals will result in the median select circuit selecting one of the two remaining good channels for control purposes.

Failure of the level control circuit (including median select circuit) which could result in flooding of the steam drum is mitigated by two independent Class 1E high steam drum water level trips which are set at 8 inches and 12 inches above normal water level. The 8 inch logic train closes the steam drum isolation valve and the main and startup bypass feedwater control valves. The 12 inch logic train closes the feedwater isolation valve.

Failure of the control valves which results in an increased steam drum water level will result in the same trips as discussed above for a failure in the level control circuit. Although the control valves may not respond to the 8 inch trip, the steam drum inlet isolation valve will still respond to the 8 inch trip.

The Class 1E trip circuits also isolate the steam generator auxiliary heat removal system, auxiliary feedwater (AFW). The 8 inch trip isolates the AFW steam isolation valves for the motor driven pumps and the 12 inch trip isolates the turbine driven pump AFW steam drum isolation valves.

The steam drum outlet nozzle which provides steam to the superheater is located 35 inches above normal water level and the steam dryers are also located well above the 12 inch trip setting. Since there are two redundant Class 1E logic trains which close redundant feedwater valves and since the steam drum can function properly at the 12 inch trip level the entry of water into the superheater inlet line need not be considered.

7.7.1.5 Steam Generator, Steam Drum Level Control System

The steam drum level control system regulates the feedwater flow to the steam drum to maintain a constant water level in the steam drum during plant operation.

The control system consists of a three element (steam flow, feedwater flow and steam drum water level) controller and a median select module. Each of the input elements have three redundant measurement channels. The median select module selects the median signal of the three channels as the input to the controller.

Independent Class 1E high steam drum level trip logic trains are provided at 8 inches and 12 inches above steam drum normal water level. Each logic train also uses three redundant inputs and a median select module.

The steam drum level control signal, the 8 inch high level signal and the 12 inch high level signal, have separate buffered signals provided from the PPS instrument channels for isolation and independence.

The control logic is shown in Figure 7.7-1.

7.7.1.5.1 Feedwater Flow Control Valve Control

The startup feedwater control valve conntrols flow in the range of 0 to 15% of rated flow. The control loop for this valve is a single element controller, using drum water level to control valve position. The main feedwater control valve is closed during this operation. When the flow rate increases to approximately 15%, the control system will automatically open the main feedwater control valve and close the startup control valve. A deadband is provided for this switchboard point to prevent cycling from one valve to the other.

The control loop for the main valve is a three element controller, using drum normal water level, steam flow, and feedwater flow, to control the valve position. Drum drain flow rate, which remains essentially constant at all power levels, is a manual input to the controller. The controller compares steam flow to feedwater flow, and the resulting net flow error signal is combined with the drum water level error signal, to control the valve position. Drum water level is controlled within ± 2 inches of the normal water level. Three redundant buffered signals are provided from the PPS for steam flow, feedwater flow and steam drum level. The median signal of each element is provided to the steam drum level controller. Manual control of the startup and main feedwater control valves is provided in the control room. Instrumentation required by this control system is obtained as follows:

- Steam Drum Level - Water level is measured by a differential pressure transmitter which senses the difference between the pressure resulting from a constant reference column of water and the pressure resulting from the variable height of water in the steam drum. The measurement is density compensated.

- o Steam Flow - Steam flow is sensed at a flow element in the outlet line from the superheater by a differential pressure transmitter. The differential pressure signal is compensated for temperature and pressure variations and linearized to provide a mass flow signal.

- o Feedwater Flow - Feedwater flow is sensed at a flow element in the inlet line to the steam drum by a differential pressure transmitter. The differential pressure signal is corrected for temperature variations and linearized to provide a mass flow signal.

7.7.1.5.2 Main Feedwater Isolation

Isolation of the main feedwater supply is provided to mitigate the consequence of the loss of feedwater to a steam drum, a steam line break, or to prevent superheater flooding.

Isolation of the feedwater supply to the affected loop in the event of a steam generator system feedwater leak will ensure integrity of the feedwater supply to the two unaffected loops and mitigates the consequence of flooding damage to other equipment. This protection is provided by automatic closure of the steam drum isolation valve and both feedwater control valves upon sensing a low steam drum pressure (500 psig) signal and automatic closure of both feedwater control valves and feedwater valve isolation upon sensing a steam generator building flooding (temperature and humidity) signal.

In the event of a steam line break, steam drum dryout may occur and would result in damage to the steam generator loop upon re-introduction of feedwater. Protection against the re-introduction of feedwater is provided by the closure of the feedwater isolation, the steam drum isolation, and control valves on low steam drum pressure (500 psig) signal.

In the event of a failure in the drum water level control components, an overfilling condition might result in flooding of the steam drum and superheater. Protection against this is provided by three redundant water level sensors and by trip functions which close the feedwater valves at two steam drum levels. The first trip level, 8 inches above normal water level, closes the feedwater steam drum isolation valve, and the feedwater control valves. The second trip level, 12 inches above normal water level, closes the feedwater isolation valve.

Protection against flooding of the superheater during steam generator auziliary heat removal is discussed in Section 5.6.1.

7.7.1.5.3 Operational Considerations

Normal Operations

The steam drum level controller utilized for feedwater control valve operation is located in the control room back panels. The operator control station for the controller is located on the main control panel in the control room.

During normal operation the steam flow and feedwater flows mismatch is summed with the drum level signal and compared to level setpoint. The resultant signal is sent to the main feedwater control valve to provide a feedwater flow balanced to steam flow plus drain flow to maintain drum levels.

Operator Information

Indicators and alarms are provided to keep the operator informed of the status of the system under control. The following measurements are continuously displayed on the Main Control Board:

Superheat steam pressure, temperature and flow;

Steam drum pressure, temperature, and level;

Feedwater pressure, temperature and flow.

7.7.1.6 Recirculation Flow Control System

The reference design calls for constant speed recirculation pumps.

7.7.1.7 Sodium Dump Tank Pressure Control System

The Sodium Dump Tank Pressure Control System functions to maintain the argon cover gas pressure over the sodium dump tank within prescribed limits. Pressure control of the sodium dump tank is maintained by the supplying or venting of argon gas to or from the cover gas region via a two-inch line. Two pressure transmitters are located on this line, one for indication and off-normal alarm, and one for control of the argon supply and vent valves.

Question CS760.99

What experiments have or will be performed to determine the heat transfer rate in the evaporator at conditions as expected at full power? How well is the heat transfer capacity known for these conditions (outlet quality approximately 0.5). How would a 20% error in heat transfer capability impact on the expected loop parameters vs. power level shown in Figures 5.7-1 and 5.7-2? What heat transfer correlations were used in those calculations?

Response:

A summary of all tests completed or planned is provided in amended PSAR sections 5.5.3.1.5.1 and 14.1.4.6. Although full power tests of the steam generators will not be performed until plant start-up, the minimum heat transfer capacity under these conditions should be known with 100% certainty. Due to conservative assumptions made in the analysis, actual performance may exceed that predicted. The analytical models used to predict the performance of the steam generator units are well established and accepted through out industry. The validity of these analytical tools has been demonstrated repeatedly through their use in the design of PWR's, LMFBR's (foreign and domestic) and non-nuclear equipment. The CRBRP steam generator test program will specifically demonstrate the accuracy and reliability of these models when used to analyze the CRBRP steam generators. Test data from the Prototype Steam Generator test program includes conditions covering the entire spectrum of CRBRP inlet sodium temperatures with exit water qualities varied from zero to 100%. Data from the in-situ testing of instrumented plant units will provide an absolute and final check of steam generator performance over the entire range of CRBRP operating conditions.

The response of the part load profile to a 20% reduction in evaporator performance should not be significant although it was not specifically analyzed. The IHTS hot-leg temperature would remain essentially unchanged since it is set by the turbine throttle temperature flow in the IHTS which would increase in response to the degradation in heat transfer coefficient, and thus the heat transfer potential ($\dot{m}\Delta T$) would increase.

Increasing the IHTS flow to maintain a constant power in the steam generators results in an increase in the IHTS cold leg (evaporator outlet) temperature. Duty split between evaporators and superheater remains virtually unchanged as do DNB location and recirculation flow. The net result of a degradation in evaporator heat transfer capacity at 100% power is an increase in IHTS flow and an increase in IHTS cold leg temperature. At lower power levels the steam generators are oversized and the results of a degradation in capacity become even less significant. At 40% power, the part load profile would be essentially unchanged.

The correlations used in the calculations of the part load profiles of PSAR Figures 5.7-1 and 5.7-2 are given in Table QCS760.99-1.

References:

QCS760.99-1 V. H. Gräber, H. Helger, Atomikerenergi 10, p.23, 1072.

QCS760.99-2 Engineering Sciences Data Unit Item 07016, "Forced Convection Heat Transfer to Circular Tubes - Part 1: Correlation for Fully Developed Turbulent Flow - Their Scope and Limitations," Inst. Mech. Engrs., London 1967.

QCS760.99-3 J.R.S. Thom, W. M. Walker, T.A. Fallon and G.F.S. Reising, "Boiling in Subcooled Water During Flow Up Heated Tubes or Annuli," Symposium on Boiling Heat Transfer in Steam Generating Units and Heat Exchangers, Inst. Mech. Engrs., Manchester 1965.

QCS760.99-4 A.A. Bishop, P.O. Sandberg, and L.S. Tong, "Forced Convection Heat Transfer at High Pressure After the Critical Heat Flux," ASME 65 HT-31, 1965.

QCS760.99-5 J.B. Heineman, "An Experimental Investigation of Heat Transfer to Superheated Steam in Round and Rectangular Channels," ANL 6213, 1960.

TABLE QCS760.99-1

REGION	CORRELATIONS USED	AUTHORS	*REFERENCE
Sodium Side	$Nu = C1 + C2 * (Pe)^{C3}$ $C1 = 0.25 + 6.20 * (P/D)$ $C2 = -0.007 + 0.032 * (P/D)$ $C3 = 0.8 - 0.024 * (P/D)$ for CRBRP; $Nu = 12.35 + 0.555\ (Pe)^{0.753}$	Gräber and Reiger	QCS760.99-1
Water Side Preheat	$Na = .0204\ Re^{0.805} Pr^{0.415}$	Engineering Sciences Data (ESD) Unit - British	QCS760.99-2
Subcooled Boiling and Nucleate Boiling	$h = \left[\frac{e^{P/1260}}{0.072}\right](q'')^{0.5}\left[\frac{T_w - T_{sat}}{T_w - T_b}\right]$ use if i) $T_w > T_{sat}$ or 2) $T_{w_{hom}} < T_{w_{ESD}}$	Thom, et al.	QCS760.99-3
Water Side DNB	$X_{crit} = \frac{A}{G^{1/3} q''^{1/8} D^{0.07}}$	Konkov	
Film Boiling	$N_{Lf} = 0.8\left[0.0193 Re_f^{0.8} Pr_f^{1.23}\right]\left[x + (1-x)(\rho_g/\rho_l)\right]_b^{0.68}\left[\frac{\rho_g}{\rho_l}\right]^{0.068}$	Bishop, Sandberg and Tong	QCS760.99-4
Superheat	$Nu_f = 0.0133\ Re_f^{0.84} Pr_f^{0.333}$	Heineman	QCS760.99-5
Tube Thermal Conductivity	$K = 24.246 - 0.005188\,T$		

Note: Except for subscript f which denotes "average film," parameters are evaluated at "stream bulk" conditions.

Question CS760.178A1

Can TOP accidents become prompt-critical in such a way that internal fuel motion in lower power channels is the key factor in the energetics determination? Is such an event possible only for midplane failures with low sweepout? How is the degree of sweepout determined? What is the effect of intrasubassembly incoherence on sweepout?

Response

The assessment of unprotected TOP events in the CRBRP (Chapter 6 of Ref. QCS760.178A1-1) concluded that a prompt-critical response would not occur for nominal conditions and would be very unlikely even for combinations of pessimistic assumptions on fuel rod failure location (i.e., midplane) and reactivity insertion rates. These conclusions are substantiated by additional considerations of likely reactivity insertion rates, fuel sweepout mechanisms and the effect of intra-assembly incoherence on fuel sweepout.

Reactivity Insertion Rate

The maximum reactivity insertion rate evaluated for TOP events is an important consideration in determining the potential for energetic consequences. Section 3.3.2 of Ref. QCS760.178A1-2 examined the abnormal reactivity insertion events which could lead to a TOP initiated HCDA. Both anticipated events (Table 15.2-1 of the PSAR) combined with failure of both shutdown systems and events beyond the protection system design bases were considered.

Reactivity insertion rates for the heterogeneous core have subsequently been analyzed. Anticipated events, unlikely events, and extremely unlikely events were considered. Based upon this analysis, there are no identified events that result in reactivity insertions greater than one dollar which occur at rates in excess of 12¢/s.

Fuel Sweepout Mechanisms and Incoherence Effects

For the nominally predicted upper fuel rod failure locations the initial fuel motion to the failure site results in negative reactivity effects such that the potential for a prompt-critical excursion doesn't exist and the core response is not sensitive to the degree and timing of fuel sweepout from the core. For this case the fuel sweepout response is more directly related to a determination of the potential for damaged core coolability and end state of the transient, as discussed in Sections 6.1.1 and 6.2.2 of Ref. QCS760.178A1-1.

If a fuel rod were assumed to fail at the core midplane (i.e., location of peak axial flux), the initial fuel motion response would result in the maximum positive reactivity feedbacks. This assumption, if coupled with very limited fuel motion in the sodium flow channel, is considered to be the only plausible way in which an unprotected reactivity insertion event in CRBRP could result in a prompt-critical transient.

In recognition of the importance of fuel rod failure location, calculations were performed which assumed coherent, fuel rod midplane failures (Chapter 6, Ref. QCS760.178A1-1). These calculations indicated that prompt-critical conditions did not result from assumed midplane failures in CRBRP. In reaching this conclusion it was recognized that the use of more realistic analytic methods (PLUTO-2) is important in determining the appropriate accident progression. These methods, which are experimentally supported, show that after a brief time interval the net effect of fuel motions (within and outside the fuel rod) lead to negative reactivity consequences, even at relatively high core powers. This is in contrast to the SAS/FCI model which, due to several unrealistic modeling assumptions, predicts incorrect, accelerating positive reactivity at high core powers.

The PLUTO-2 calculations which were performed (Ref. QCS760.178A1-1, Section 6.2 and Appendix E) are conservative in that the larger time-dependent SAS/FCI cavity was used. Although fuel plate-out parameters were not varied, parametric variations in fuel particle size, based on PLUTO-2 applications to TREAT experiments, were used to reduce the predicted amount of fuel sweepout. These calculations still indicated that a prompt-critical transient would not be expected in the CRBRP.

The application of PLUTO-2 to experiments and the phenomenological understanding gained in representing fuel sweepout is summarized in the following. A more detailed discussion of the PLUTO-2 modeling and its bases is provided as an attachment to this response.

Pre- and post-test analyses of TREAT tests E8, H6, and L8 have been performed with PLUTO-2 and its predecessor PLUTO. Although several modeling differences occur between the two computational techniques, reasonable compatibility in predicted conditions exist for the first 20 to 30 milliseconds. This is because none of the significant differences between the codes are physically required on this time frame.

TREAT tests E8 and H6 simulated TOP events in the FFTF at 3 \$/s and 50 ¢/s, respectively*. Test E8 conditions were unfavorable for sweepout in that the pump pressure drop and flow through the test section were very low compared to the reactor environment. Nevertheless, there was considerable early fuel sweepout observed by the hodoscope. The observed sweepout was faster than that calculated with PLUTO. This is considered to be due to the assumption of a single fuel particle size in PLUTO. On the whole, the comparison to experiment was very good and on the conservative side; that is slower and less sweepout.

The hydraulic parameters for Test H6 were closer to FFTF and CRBRP hydraulic conditions then Test E8 and had a lower reactivity insertion rate of 50 ¢/s. The test showed several FCI events separated by more than 100 msec. The first event in the H6 experiment was analyzed with PLUTO (Ref. QCS760.178A1-3). The failure of only one rod was assumed which led to a rapid fuel sweepout of about 10 g above the top of the active fuel. The final hodoscope data, which were available only after the PLUTO analysis, indicate that about 10 g of fuel moved beyond the top of the active fuel within 30 msec and 28 g

*Using 34 cm EBR-II irradiated fuel rods.

within 90 msec. This is an indication that more than one rod may have failed during this time interval.

The main pressure and flow event in test H6 was analyzed with PLUTO-2 (Ref. QCS760.178A1-3). Only a fair agreement with the flow and pressure data could be achieved. This was at least partially due to the limited knowledge about the initial conditions at the beginning of this last event of the experiment. The PLUTO-2 calculation, which assumed the simultaneous failure of three rods, resulted in a rapid upward sweepout of 66 g of fuel. The final hodoscope report (Ref. QCS760.178A1-4) puts the upward dispersal during this event at 78 ± 12 g within 30 msec.

The fuel sweepout during this event was relatively massive although the hodoscope data indicate that the rod failures were close to the midplane. Some of the fuel swept upwards may have been fuel which had collected near the midplane due to earlier rod failures. These had led to the failure of the flow tube surrounding the rod bundle which must have caused a low pressure situation near the midplane, reducing the potential for sweepout.

The L8 test simulated the condition in an assembly during a LOF-d-TOP event (Ref. QCS760.178A1-5). At the time of rod failure the sodium velocity had decreased to 1.3 m/sec and the pump pressure was around 0.05 MPa. Although these conditions are not typical for a slow ramp rate TOP accident, this test is nevertheless relevant for the investigation of fuel sweepout. Several features in this test potentially degraded the sweepout: (a) small pump pressure, (b) low initial coolant velocity, and (c) a near-midplane cladding failure location for which the ejected fuel has not much axial momentum; the upward sweepout was nevertheless very rapid. As in the E8 test simulation, the PLUTO-2 calculated sweepout above the top of the active fuel again lagged behind the measured one (see Appendix A).

In Fig. QCS760.178A1-1 normalized fuel reactivity histories of the measured and calculated fuel distributions are shown. These fuel reactivities are obtained by integrating the product of a fuel worth curve and the axial fuel distribution over the length of the pins. It is apparent from the figure that the significant fuel sweepout and dispersal which occurred in this test was well represented by PLUTO-2. According to the hodoscope results the fuel motion reactivity became negative about 20 msec after rod failure in this test (Ref. QCS760.178A1-6). The slight positive reactivity right after pin failure in the test data may be due to a lesser extension of the initial clad rupture above the midplane than assumed in the post-test simulation. However, this may also be due to the disregarding of the fuel self-shielding and can be altogether considered statistically insignificant when compared to earlier variations in the hodoscope reactivity curve.

In summary the available fuel motion data from the TOP in-pile tests in which fuel was injected into liquid sodium show a significant early fuel sweepout. The rapidity of the fuel sweepout does not seem to be strongly affected by the axial cladding failure location or the fraction of pins failing.

The modeling of fuel sweepout just discussed invokes the customary one-dimensional assumptions. This approach does not explicitly account for two-dimensional coolant bypass (incoherence effects) which introduces two

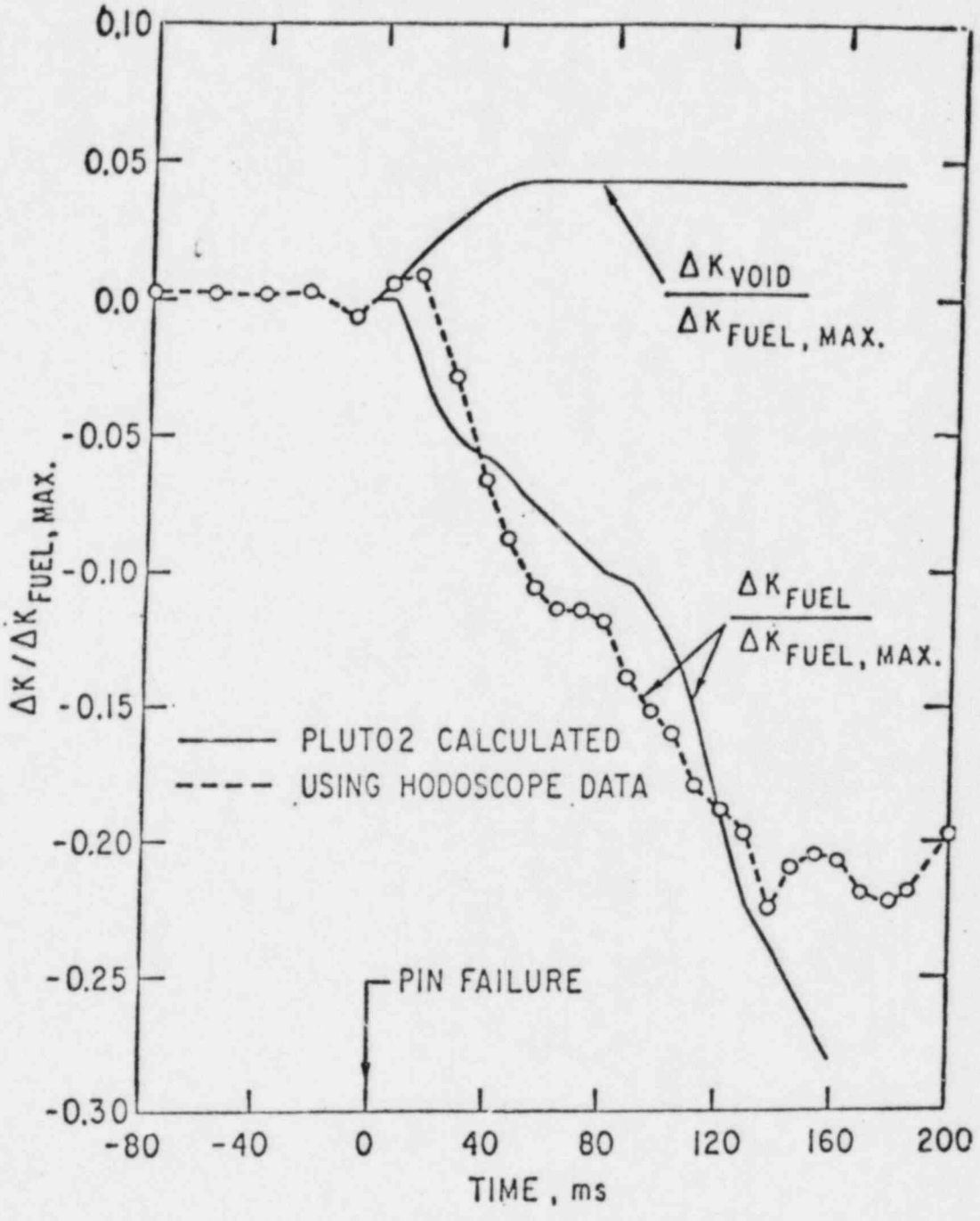

Fig. QCS760.178A1-1 Comparison of PLUTO-2 Calculated Reactivity History for TREAT Test L8.

opposing considerations for an assumed midplane failure at a low rate reactivity insertion. In a large rod bundle, coolant bypass effects will be significant in proportion to the time delay between individual intra-assembly fuel failure events. The first consideration is that any time delay between failure events results in a stretch-out of the positive reactivity effect of fuel motion and allows more time for fuel sweepout to occur and reduce reactivity as discussed in Ref. QCS760.178A1-7. The second consideration is the reduced rate of fuel removal. As noted in out-of-pile tests, coherent bundle flow conditions showed more sweepout of simulant fuel than less coherent flow conditions Ref. QCS760.178A1-8. However, it was shown that even under the less coherent test flow conditions neutronically significant sweepout occurred. It is also noted that the TREAT tests used for calibration of the fuel sweepout modeling introduced some degree of incoherence into the calibration process itself.

In considering both effects, the current Project position is that neither the positive effect of delayed failure events nor the retarding effect of coolant bypass on fuel sweepout introduce a significant uncertainty into the reference calculations performed. Again, it is noted that it was possible to simulate the observed fuel sweepout in three experiments fairly well with the PLUTO-2 code (usually the very early sweepout was somewhat underestimated by the code).

The NRC staff review pointed out that the degree of lead assembly failure coherence would be greatest at EOC-3, whereas the Project examined the EOC-4 core configuration in Ref. QCS760.178A1-1. However, initial calculations performed by staff consultants at ANL, which assumed midplane failures and weak fuel sweepout (PLUTO-2 parameters used in these calculations were similar to those used in a successful post-test analysis of the TREAT L8 test except that the parameter controlling fuel plate-out was more conservative), concluded that a sustained prompt-critical condition would not occur for reactivity insertion rates less than 20 ¢/s (Ref. QCS760.178A1-9). This conclusion, which is consistent with the Project understanding, will be further confirmed following detailed determination of the EOC-3 neutronics safety parameters.

Hence, for the amount of expected incoherence among fuel assembly failures in response to an unprotected, $\leq$ 12 ¢/s reactivity ramp insertion, and for the limited positive fuel motion prior to sweepout dominance, a sustained prompt-critical state would not occur in the CRBRP. This nonenergetic response is considered generic to a CRBRP type core driven by a low rate reactivity insertion.

References

QCS760.178A1-1 S. K. Rhow, et al., "An Assessment of HCDA Energetics in the CRBRP Heterogeneous Reactor Core," CRBRP-GEFR-00523, General Electric Company, December 1981.

QCS760.178A1-2 "Hypothetical Core Disruptive Accident Consideration in CRBRP; Energetics and Structural Margin Beyond the Design Base," CRBRP-3, Vol. 1.

QCS760.178A1-3 H. U. Wider and L. A. Semenza, "Analysis of TREAT Transient Overpower Experiments Using the PLUTO Codes," Proc. Specialists Workshop on Predictive Analysis in LMFBR Safety, Los Alamos, New Mexico, LA-7938-C, March 1979.

QCS760.178A1-4 C. L. Fink, "Final Hodoscope Report for H6," Argonne National Laboratory, ANL/RAS, Report H6.T, May 1980.

QCS760.178A1-5 C. H. Bowers, et al., "Analysis of TREAT Tests L7 and L8 Using SAS3D, LEVITATE and PLUTO-2," Proc. Specialists Workshop on Predictive Analysis of Material Dynamics in LMFBR Safety, Los Alamos, New Mexico, LA-7938-C, March 1979.

QCS760.178A1-6 H. U. Wider, et al., "The PLUTO-2 Overpower Excursion Code and a Comparison with EPIC," Proc. Int'l. Mtg. on Fast Reactor Safety, Seattle, Washington, August 1979.

QCS760.178A1-7 A Padilla, et al., "On the Consequences of Axial Midplane Failures during Hypothetical Transient Overpower Accidents," Proc. Int. Topical Meeting on LMFBR Safety and Related Design and Operational Aspects, July 19-23, 1982, Lyon, France.

QCS760.178A1-8 B. W. Spencer, et al., "Fuel Motion in the CAMEL TOP-Simulation LMFBR Safety Tests," Proc. Int'l Meeting on Fast Reactor Safety, Seattle, Washington, August 1979.

QCS760.178A1-9 H. Hummel, P. Pizzica, and P. Garner, Quarterly Report, April-June, 1982, Argonne National Laboratory, ANL-82-24, Vol. II.

APPENDIX A TO: Question CS760.178A1

Fuel Sweepout Modeling in PLUTO-2 and Its Experimental Bases

This Appendix provides additional detail on the important PLUTO-2 modeling parameters and relevant experimental data used to make judgements on fuel sweepout in the CRBRP during low ramp rate TOP events.

The available fuel motion data from the TOP in-pile tests in which fuel was injected into liquid sodium show a significant early fuel sweepout. The rapidity of the fuel sweepout does not seem to be strongly affected by the axial cladding failure location or the fraction of rods failing.

It is noted that it was possible to simulate the observed fuel sweepout in several experiments fairly well with the PLUTO-2 code (usually the very early sweepout was somewhat underestimated by the code). The important parameters in these post-test simulations are the fraction of rods failing, the axial failure location, and the sodium void fraction below which transition to annular fuel flow is allowed. Somewhat less important are the rod failure pressure, the fuel particle size and fuel plate-out and crust release parameters. One could decrease the calculated negative fuel motion considerably by not allowing the particulate flow regime. However, this would make it impossible to match experimental data.

Two out-of-pile test series to investigate fuel sweepout have been performed. In the ANL-CAMEL experiments (Ref. A-1) about 30% of the injected UO_2-Mo thermite mixture is typically swept upwards in particulate form and the remaining fuel is plated out near the injection location. In contrast, KFK experiments using electrically heated UO_2 rods (Ref. A-2) show a nearly complete sweepout of the injected fuel. The KFK results, which are in close agreement with the modeling of the early sweepout in PLUTO-2, are more prototypic of the reactor environment in some important respects.

The following sections provide the additional analytic and experimental detail.

In-Rod Fuel Motion and Fuel Ejection Modeling in PLUTO-2

The schematic in Fig. A-1 shows the in-rod and channel fuel motion which are modeled in PLUTO-2. The flow of the molten fuel/fission-gas mixture inside the fuel rods is treated as a homogeneous (i.e., no-slip), compressible, and one-dimensional flow with variable flow cross section.

The assumption of a homogeneous flow inside the rod becomes questionable after an extensive blowdown has led to a sizeable internal void fraction; annular or slug fuel flow may be more appropriate. Homogeneous flow probably exaggerates the in-rod fuel motion towards the clad failure for longer times and for midplane failures is therefore conservative.

The calculation of the ejection through a clad rupture is based on local pressure equilibrium between the fuel rod cell and the adjacent coolant. The

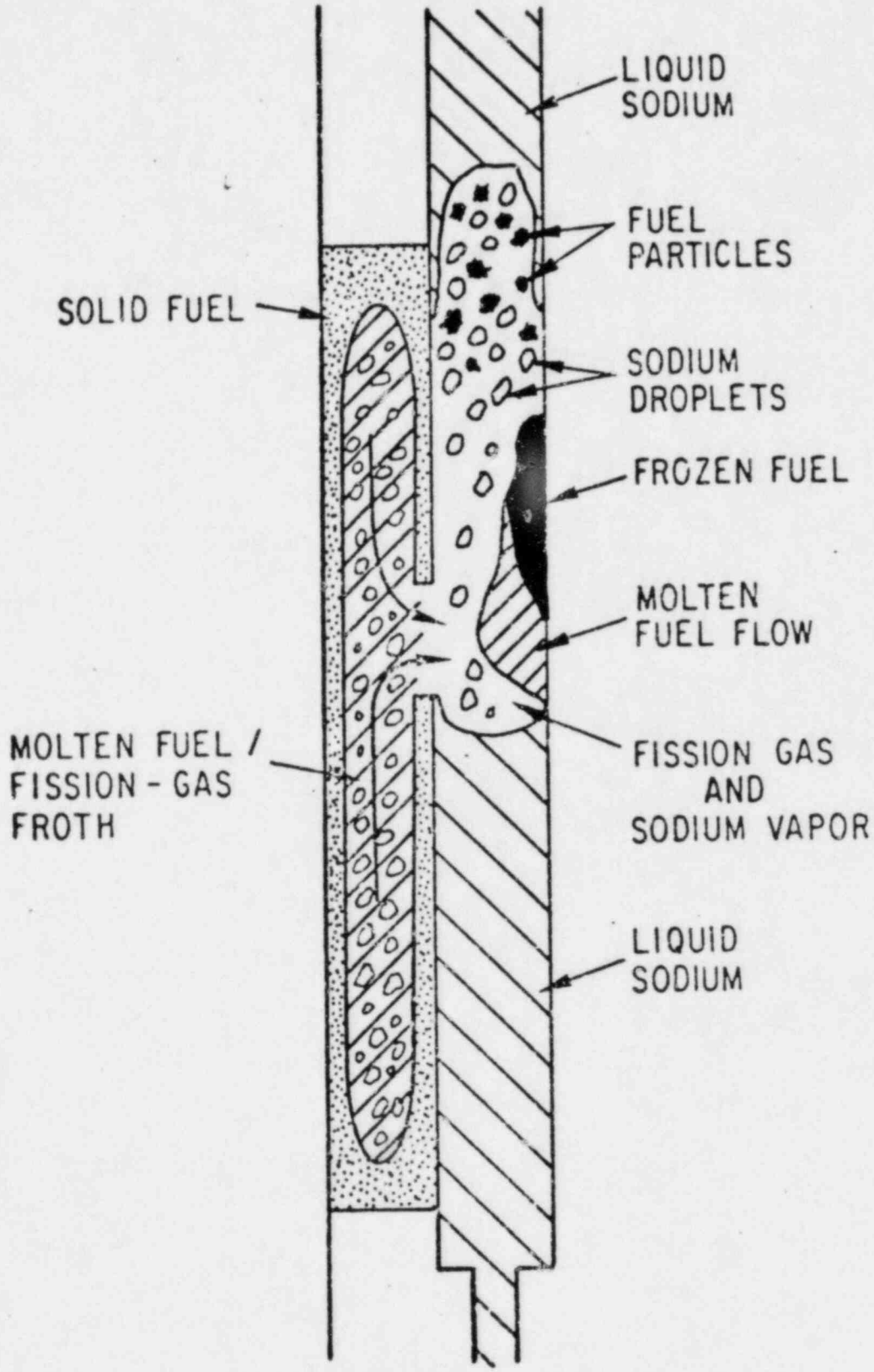

Fig. A-1 Schematic of PLUTO-2.

QCS760.178A1-A2

mass ratio of ejected fuel to fission gas is assumed to be the same as that in the ejecting rod mesh cell. A key factor for the ejection rate is the rate of in-rod fuel motion into the ejection cell which is controlled by the small cross section of the molten cavity. The latter is considerably smaller than clad rupture sizes found in the post-test examinations of TREAT tests H5 and R12. For longer times (i.e., tens of milliseconds) a preferential ejection of fission gas may take place based on a PLUTO-2 analysis of the TREAT L8 test (Ref. A-3).

In the context of PLUTO-2 the most conservative assumption is a simultaneous failure of all rods at the midplane. This assumption maximizes the total in-rod fuel motion. The larger fuel masses ejected then promote the transition to an annular fuel flow and subsequent fuel plate-out, and thus, minimize the fuel particle sweepout relative to the fuel mass ejected from the failed rods. This is discussed in more detail in the following sections.

Fuel Fragmentation, Transition to Annular Fuel Flow and Fuel Plate-Out

In PLUTO-2 the molten fuel injected into the coolant with a liquid sodium fraction greater than the input value CIBBMN will fragment instantaneously into droplets of one size. These droplets can further fragment into smaller ones after a time delay which is input. Molten fuel ejected into a coolant node with a liquid sodium fraction below CIBBMN will be deposited on the cladding and structure and move as a partially or fully annular film. Molten fuel droplets already existing at a certain elevation will also be deposited on clad and structure if the liquid sodium fraction drops below CIBBMN. Figure A-2 illustrates the possible fuel configurations and flow regimes in an equivalent coolant channel. What fraction of the channel perimeter is wetted by a partially annular flow is determined by a linear interpolation between zero and an input volume fraction CIANIN which defines the volume fraction above which the entire perimeter is wetted. If the bulk temperature of the annular fuel film drops below an input energy EGBBLY and if the outer clad temperature has not yet reached an input temperature TECLMN, which should be at or below the clad solidus, fuel plate-out will be initiated. Additional fuel moving into a node with plated-out fuel may have a higher energy than EGBBLY and may move through this node without plating-out. Existing crusts can remelt due to fission heating and crusts which have completely melted the underlying clad can slide into a neighboring node. For high fuel fractions in the channel the fuel flow regime can also become bubbly in PLUTO-2. However, this flow regime is not relevant for the early sweepout.

The fuel sweepout in PLUTO-2 depends strongly on the flow regimes, and thus, on the parameters controlling the flow regime transitions. For example, if the sodium liquid fraction CIBBMN, below which a transition to annular fuel flow is allowed, is set to a relatively small number, more fuel particles will be generated and swept out. A value of 0.33 was used in the reasonably successful L8 and H6 simulations (Refs. A-3 and A-4). A value of CIBBMN which is below the initial sodium film fraction (usually set to 0.15) can change the calculational results significantly because part of the liquid film has to be evaporated or entrained before the transition to annular fuel flow is possible.

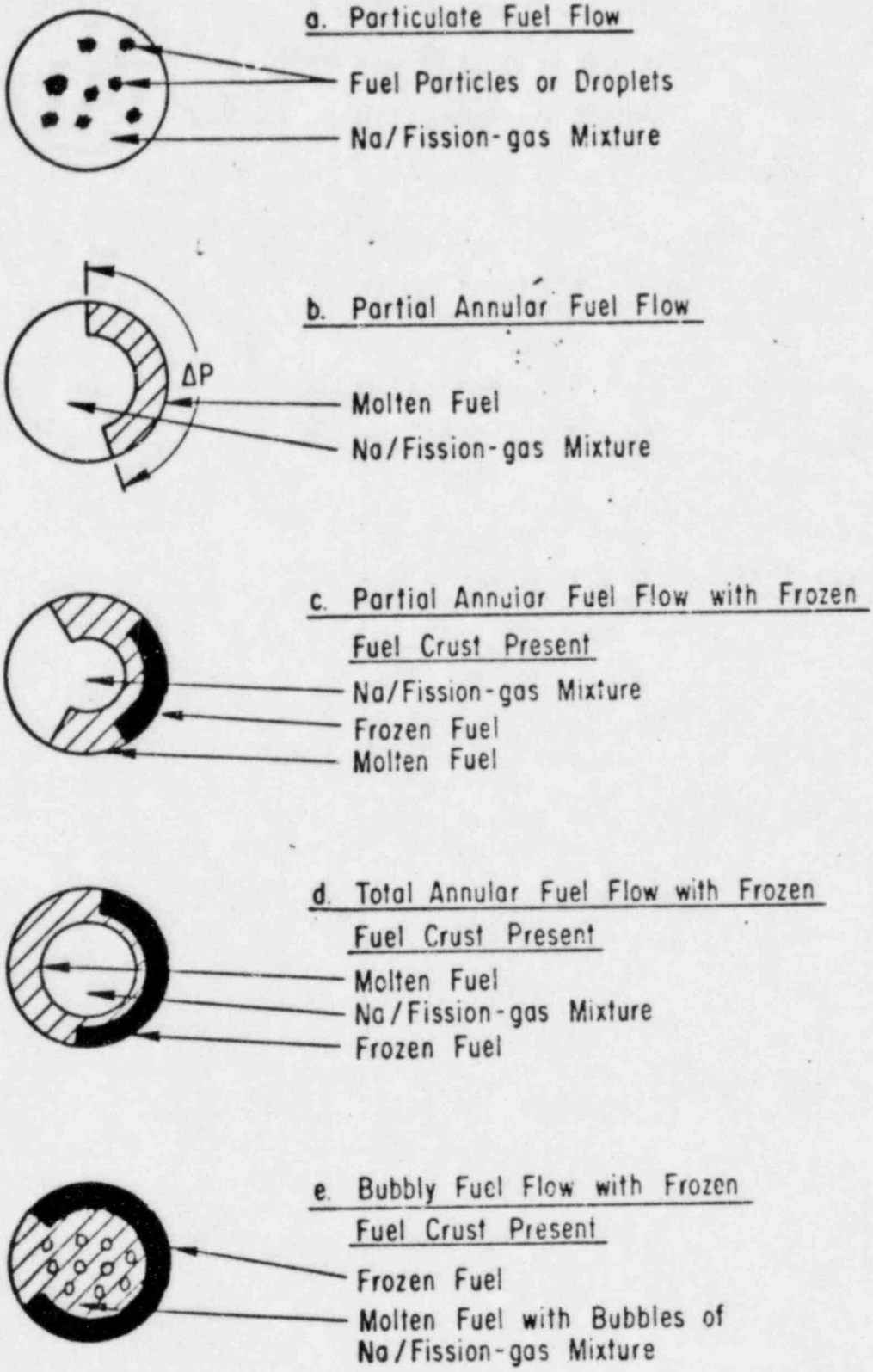

Fig. A-2 Fuel Flow Regimes in PLUTO-2.

Fuel-to-Coolant Heat Transfer

In the particulate flow regime the choice of droplet diameter, which is input, is fairly significant. Although the particle drag force changes with the radius, the main effect is on the fuel-to-coolant heat transfer which is assumed to be of the following form in PLUTO-2:

$$h_{f,Na} \cdot A_{f,Na} = \frac{k}{r} \cdot \frac{M_f}{4/3\pi r^3} \cdot 4\pi r^2 \cdot (1 - \alpha_{Na})^{CIA2}$$

$A_{f,Na}$ contact area between fuel and liquid sodium,

r fuel particle or droplet radius,

k fuel thermal conductivity,

M_f total fuel particle mass in a numerical node,

α_{Na} Na void fraction,

CIA2 input constant - a value of 2.0 was used in the H6 and L8 TREAT test analyses.

The fuel particle radii used for successful simulations of TOP experiments were relatively large (0.25-0.17 mm) for tests in which the initial sodium flow velocities and inlet pressures were considerably smaller than expected for realistic TOP conditions. For more prototypical conditions particle radii of 0.1 mm were found to give better agreement. The PLUTO-2 results are not very sensitive to the choice of the above-mentioned input constant CIA2 because the above heat transfer formulation is not used for most nodes in which a high void fraction exists. In nodes containing molten fuel and little liquid sodium the fuel flow regime is partially or fully annular. For this flow regime the fuel-to-sodium heat transfer coefficient is of the form:

$$\frac{1}{h_{f,Na}} = \frac{1}{h_f} + \frac{1}{h_m}$$

where

$$h_f = CIA3 \cdot v_f \cdot C_f \cdot Re_f^{0.8}/D_f$$

and

$$h_m = \begin{cases} \text{HCFFMI} & \text{for } \alpha_{Na} < 0.5 \\ 2(\text{HCFFMI} \cdot (1 - \alpha_{Na}) + & \\ \text{HCFFMI} \cdot 0.01 \cdot (\alpha_{Na} - 0.5)) & \text{for } 0.5 < \alpha_{Na} < 1 \\ (C1 \cdot (D_m \cdot \rho_m \cdot |u_f - u_m| & \\ C_m/k_m)^{C2} + C3)\ k_m/D_m & \text{for } \alpha = 1 \end{cases}$$

where:

subscript f fuel,

subscript m sodium-fission gas mixture,

Re Reynolds number,

$Re_f = \rho_f |u_f - u_m| D_f/(2v_f)$

CIA3, C1, C2, C3 input constants,

C specific heat,

k conductivity,

v viscosity,

D hydraulic diameter,

α void fraction

HCFFMI boiling heat transfer coefficient.

The main reason why the heat transfer between fuel and sodium in the annular fuel flow regime is smaller than in the particulate flow regime is however, due to the considerably smaller fuel-to-sodium interaction area in the annular flow regime.

PLUTO-2 Applications to In-Pile Tests

Pre- and post-test analyses of TREAT tests E8, H6, and L8 have been performed with PLUTO-2 and its predecessor PLUTO. PLUTO models only a fuel particle flow regime, does not treat fuel plate-out and has a significantly different numerical treatment than PLUTO-2. For TOP conditions the two models nevertheless compare reasonably well up to 20 to 30 milliseconds after rod failure. This is because no extensive fuel flow regime changes and fuel plate-out take place in PLUTO-2 during the early post-failure time in a TOP.

TREAT Test E8

The E8 test simulated a 3$/sec TOP accident in FFTF using the MK-II loop. The pressure drop provided by the pump was only about 0.2 MPa and the initial sodium velocity only 3.5 m/sec. Both values are significantly smaller than prototypic ones and have rather certainly decreased the fuel sweepout potential in this test. Nevertheless, there was considerable early fuel sweepout observed by the hodoscope. This is shown in Figs. A-3a and A-3b along with the post-test calculations performed with PLUTO (Ref. A-5). The failure location in this test was probably above the midplane which may have enhanced the sweepout. However, as discussed later, tests such as H6 and L8 with near midplane failures also showed rapid fuel sweepout. From the figures it can be seen that the sweepout in the experiment was faster than in the calculation. This is probably due to the fact that only one particle size is treated in the PLUTO codes. In the experiment there was probably a particle distribution including very small fragments which were swept upwards more rapidly than the average particle. The magnitude of the experimentally observed sweepout is also larger than calculated. This may be partially due to an overestimation by the hodoscope which does not take into account the "un-self-shielding" of fuel which has moved above the active fuel.

A PLUTO pre-test analysis also gave a fair agreement with the early sweepout by assuming simultaneous failure of 3 of the 7 rods. In the test 3 rods probably failed within 15 milliseconds.

TREAT Tests H6 and L8

Test H6 simulated a 50 cent/sec TOP accident in FFTF using an improved MK-II loop. The pressure drop of 0.76 MPa and the initial flow velocity of 6.7 m/sec were nearly prototypic. The test showed several events which were separated by more than 100 milliseconds. The hodoscope was radially misaligned in this test and covered only half of the rod bundle. Therefore, no attempt was made to compare the calculated and measured fuel distributions in detail. However, the final hodoscope report indicates that most of the fuel motion took place in the half of the bundle which was covered by the hodoscope. This makes the comparison with the calculated sweepout more meaningful.

The L8 test simulated a LOF-d-TOP condition using three GETR-irradiated rods of 86 cm length, and a maximum power of 43 times nominal. The PLUTO-2 calculated sweepout again lagged behind the measured one (see Fig. A-4). For the later times this was probably related to the simplified fuel plate-out and fuel crust release modeling in PLUTO-2. In the pre-test analysis no fuel crust release upon melting of the underlying clad was considered. This led to the discrepancies in the sweepout above the top of the active fuel and modeling changes for the post-test calculation (Ref. A-3).

The relatively good agreement on early fuel sweepout between PLUTO-2 and both TREAT tests H6 and L8 was discussed in the main response to this question.

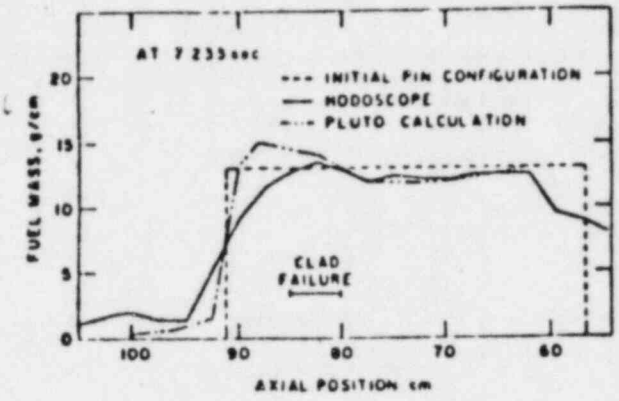

Fig. A-3a Hodoscope-Determined and PLUTO-Calculated Fuel Distributions in E8 at 23 msec after First Fuel Ejection (Top of Initial Fuel at 91 cm).

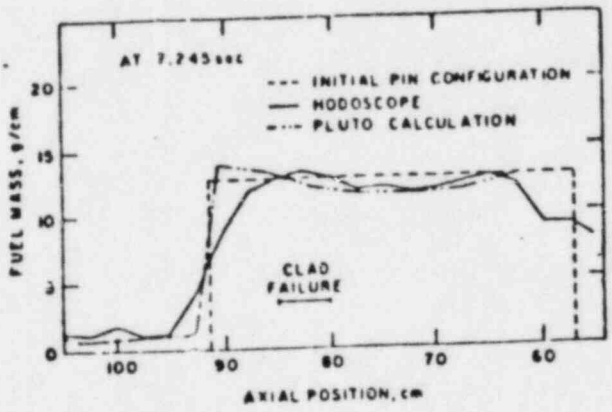

Fig. A-3b Hodoscope-Determined and PLUTO-Calculated Fuel Distributions in E8 at 35 msec after First Fuel Ejection (Top of Initial Fuel at 91 cm).

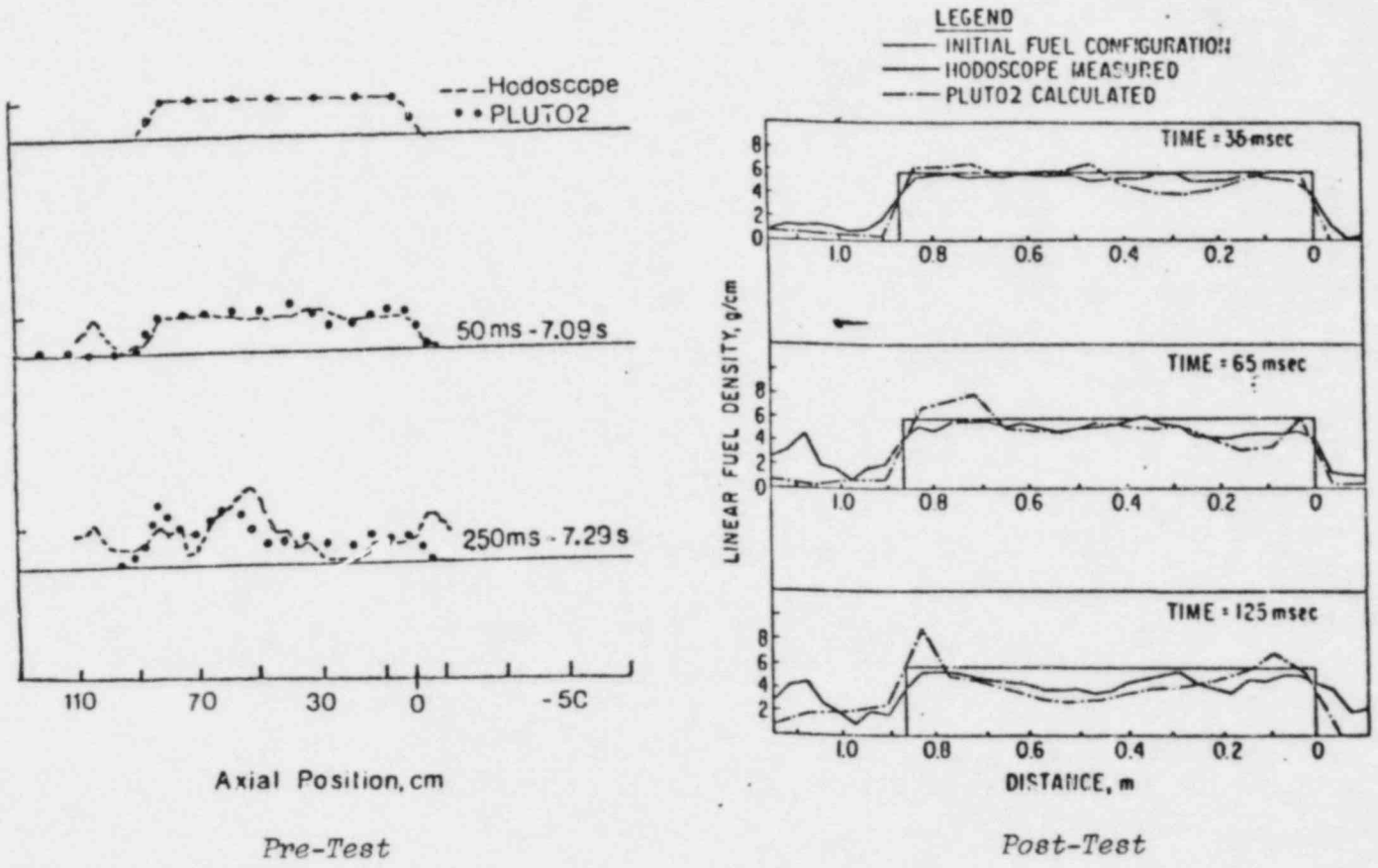

Fig. A-4 Fuel Motion Analysis for L8.

Out-of-Pile Phenomenological Evidence on Sweepout

Two series of out-of-pile experiments have been performed to investigate fuel sweepout (Refs. A-1 and A-2). In the CAMEL tests performed at ANL, a UO_2 - molybdenum mixture, generated by a thermite reaction, was injected laterally into flowing sodium in single and seven-pin bundles. Typically about 30% of the injected 25 g of fuel (in 7 rod tests) got swept upwards in particulate form. The remaining fuel plated out near the injection location. X-ray pictures show that the fuel accumulated at least momentarily in the sub-channels, occupying a progressively larger fraction of the channel cross

section as it spread among the rods. Local, small-scale FCI's appear to initiate the fuel dispersal in the form of fuel particles. This is in contrast to the early fuel motion modeling in PLUTO-2 which assumes that all the fuel injected into a liquid sodium stream fragments into droplets.

References

A-1 B. W. Spencer, et al., "Fuel Motion in the CAMEL-TOP Simulation LMFBR Safety Tests," Proc. Int'l Meeting on Fast Reactor Safety, August 1979, Seattle, Washington.

A-2 E. Bojarski, et al., "Results of Out-of-Pile Experiments on Fuel-Sodium Interaction Using X-Ray Technique," Proc. Int'l Meeting on LMFBR Safety, July 1982, Lyon, France.

A-3 C. H. Bowers, et al., "Analysis of TREAT Tests L7 and L8 Using SAS3D, LEVITATE and PLUTO-2," Proc. Specialists Workshop on Predictive Analysis of Material Dynamics in LMFBR Safety, March 1979, Los Alamos, New Mexico, LA-7938-C.

A-4 H. U. Wider, et al., "The PLUTO-2 Overpower Excursion Code and a Comparison with EPIC," Proc. Int'l Meeting on Fast Reactor Safety, August 1979, Seattle, Washington.

A-5 H. U. Wider and L. A. Semenza, "Analysis of TREAT Transient Overpower Experiments Using the PLUTO Codes," Proc. Specialists Workshop on Predictive Analysis in LMFBR Safety, March 1979, Los Alamos, New Mexico, LA-7938-C.

Question CS760.178A2

An LOF-d-TOP might still occur if the sodium void worth is 50-60 percent higher and internal fuel motion in TOP type channels can occur. What are the reactivity uncertainties of sodium void, Doppler, axial expansion and lead channel fuel motion? How do you interpret the significance of these uncertainties?

Response

A detailed review of the reactivity uncertainties used by the Project has been performed. The conservative values previously used (Ref. QCS760.178A2-1) for the Doppler ($\pm$ 20%) and fuel expansion ($\pm$ 40%) are still considered appropriate. The lead channel fuel motion behavior is extensively addressed in the response to QCS760.178A3 and the conclusions on nominal behavior are incorporated herein. The positive sodium void reactivity effect is the most important reactivity insertion mechanism to be considered in the study of loss-of-flow accidents without scram leading to overpower-induced rod failures in unvoided low-power assemblies (LOF-d-TOP). The sodium void has been re-evaluated for the CRBRP BOC-1 and EOC-4 configurations using the same data base and computational methodology as those employed in the analysis of the zero-power experiments at the ZPPR critical facility. The evaluation yields an experimentally-based, best estimate value for the sodium void reactivity and its associated uncertainty.

The impact of the derived coolant void reactivity data on the potential for LOF-d-TOP behavior in CRBRP has been assessed. The EOC-4 core would be the most likely to have LOF-d-TOP potential, due to the occurrence of the maximum positive void reactivity at the end-of-life. Detailed analysis of the loss-of-flow event in the EOC-4 core using the best estimate coolant void reactivity worths upwardly adjusted to very conservatively envelop uncertainties has demonstrated the absence of LOF-d-TOP potential. Recent analysis and results from TREAT test L8 suggest that the autocatalytic reactivity effects previously associated with whole-core LOF-d-TOP events were overestimated.

The remainder of the response has been divided into two sections dealing first with the sodium void worth and uncertainty determination, followed by a whole-core effect analysis, which supports the absence of LOF-d-TOP.

Sodium Void Uncertainties

The uncertainties assigned to calculated values of the sodium void reactivity worth are of interest because of their impact on the probability of an LOF-d-TOP. Large uncertainties are often quoted since the sodium void reactivity involves a competition between two large and opposite signed effects; a positive non-leakage component and a negative leakage component. Calculated worths are therefore sensitive to the computational methods, modeling and data which are used. If attempts are made to assess the uncertainties based upon sensitivities to alternative computational models, the results of the study would be quite dependent on the particular methodology. An alternative approach makes use of the available experimental data to deduce a predicted value with associated uncertainties which are independent of the particular methodology. Such an approach has been adopted herein.

During the past decade a large experimental data base has been established on sodium-void reactivity effects in LMFBRs. An assessment of these data has recently been completed at ZPPR and provides the input required to establish an uncertainty for the CRBRP sodium-void reactivity effect (Ref. QCS760.178A2-2). The assessment included analysis of over 100 critical experiments in LMFBR-type assemblies of CRBR size or larger. The same data base (ENDF/B-IV) and methods were used for all of the analyses. Bias factors and uncertainties were obtained as a function of reactor type, size, zone, enrichment, and blanket fissile buildup. By applying such bias factors for CRBR analysis to calculations which use the same methodology as that applied in the critical experiment analysis, a best estimate of physically observable void reactivities can be determined for a specific void configuration. The best estimate value and its uncertainty would be independent of both computational method and differential data base. The results could then be used to assess the accuracy of other analyses such as those used in previous CRBR safety studies. In assigning total uncertainty to the best estimate value, consideration must be given to those effects which are not completely addressed by the critical experiments. Such effects include the impact of fission products, temperature distribution, fuel rod rather than plate geometry, and sequence of voiding.

The reference method used in the analysis of both the critical experiments and the power reactor include exact-perturbation diffusion theory, three-dimensional modeling, twenty or more energy groups, Benoist treatment of neutron streaming, energy and spatial self-shielding corrections, ENDF/B-IV cross section data* and ENDF/B-V delayed neutron data. Various methods approximations were investigated as part of the assessment study and the only improvements that were found to be significant relative to this reference method were for transport and mesh effects in a few isolated cases.

A comparison of the results of calculation against experiment for different subsets of the ZPPR critical experiment data base is given in Table QCS760.178A2-1. Studies made explicitly for CRBRP during the engineering mockup critical (EMC) experiment program, BOC-1 and EOC-4, are included in the table. The difference between the BOC-1 and EOC-4 results are explained by transport effects that are significant for the clean heterogeneous core, but not for the more homogeneous EOC core.

The approach chosen for biasing the calculated CRBRP sodium coefficients and for assigning uncertainties was to divide the reactor into four zones, and to preserve the integral parameters for those zones. The zones chosen were:

1. Core zones with a positive reactivity signal (central core zones),
2. Core zones with a negative reactivity signal (external core zones),
3. Axial blanket zones,
4. Internal blanket zones.

---

*Although not relevant for the critical experiment analysis, the power reactor calculations used the ENDF/B-V fission product data.

Table QCS760.178A2-1

RATIOS OF CALCULATED TO MEASURED REACTIVITIES FOR SODIUM VOIDING

Cases	C/E Before Biasing	% Standard Deviation After Biasing[a]
CRBR-EMC[b] BOC-1, Positive Part of Core	0.98	10
CRBR-EMC EOC-4, Positive Part of Core	1.23	6
101 Mixed Zones[c]	1.08	12
Axial Blankets without Control Rods	0.91	1
Axial Blankets with Control Rods	1.23	2
Core Zones with Negative Reactivity Signals	1.02	9

[a]Separate bias factors applied to positive and negative components of reactivity. For any subset, the average C/E is 1.0 after biasing.

[b]Engineering mockup critical experiments for sodium-void reactivity in CRBR; reactor geometry and composition closely matched.

[c]This and the following entries are LMFBR-type configurations but not CRBRP specific.

Table QCS760.178A2-2 lists the bias factors and the calculational uncertainties assigned to CRBR. In fact, only the central core region of the EOC-4 void reactivity is biased. Because the calculations tend to be more positive than measured reactivities, it is both conservative and easier to use a 1.0 bias factor if the best estimated value is less than unity by an amount significantly smaller than the assigned uncertainty. The uncertainties assigned to external core zones and axial blanket zones are larger than would be indicated by Table QCS760.178A2-1, but these zones were not specifically included in the CRBR-EMC studies.

Table QCS760.178A2-2

BIAS FACTORS AND UNCERTAINTIES FOR
SODIUM-VOID REACTIVITY IN CRBRP

Zone	Bias Factor[a] BOC-1	Bias Factor[a] EOC-4	Calculational Uncertainty[b] % BOC-1	Calculational Uncertainty[b] % EOC-4
Central Core	1.0	0.82	10	6
External Core	1.0	1.0	10	10
Axial Blankets	1.0	1.0	20	20
Internal Blankets	1.0	1.0	20	20

[a] To be multiplied times the calculated value.

[b] To be added in quadrature with uncertainties from other sources (see Table QCS760.178A2-4).

When extrapolating the above zero-power results to a power reactor, additional effects require consideration. Since differences in sodium-void between ZPPR and the CRBR are implicitly accounted for in the calculational models, such effects lead only to additional uncertainties.

The ZPPR assemblies are built of fuel plates whereas the power reactor uses rods. The effects of the different geometry on the calculational uncertainty were investigated by analyzing small zone critical experiments in rod geometry using the reference methods. No significant change in ability to calculate the void worth in the different geometries was noted. As a consequence, no additional uncertainty is required to account for the change in fuel geometry.

The void worth in the power reactor is calculated by assuming that flowing sodium has been voided from all fuel assemblies. The worth tables so derived are used to determine the sodium-void reactivity for the specific reactor configurations throughout the voiding sequence. The uncertainty introduced by this approximation was determined by comparing ZPPR calculation with experiment using both the exact sequence modeling and the more approximate model. An uncertainty of $\pm$ 3.5% can be ascribed to this effect.

Although the CRBR-EMC critical experiments matched the nuclide compositions very well, no attempt was made to simulate the build-up of fission products during the fuel cycle. Therefore, an uncertainty arising from the fission product inventory is introduced for the EOC-4 configuration. The fission products increase the non-leakage term in the sodium-void effect through changes in the real and adjoint neutron flux. Calculations were performed to investigate this effect. If an uncertainty of $\pm$ 20% is assumed

in the absorption cross section of the fission product data, an uncertainty of ± 4% is introduced in the calculated sodium-void reactivity. There is considerable evidence to suggest that such an uncertainty is very conservative. The reference calculation made use of a lumped fission product derived from the ENDF/B-V data files. A second calculation was run using lumped fission product data from ENDF/B-III which are based on a 20 year old evaluation of Garrison and Roos (Ref. QCS760.178A2-3). The difference in the calculated sodium void reactivity for the two sets of data is less than 0.5%. A recent NEACRP benchmark calculation compared fast reactor spectrum averaged fission product capture data and some of the results are given in Table QCS760.178A2-3. It is of interest to note that the ANL results are ∿ 9% higher than the mean of all the countries participating in the exercise, and ∿ 20% higher than the French results which are adjusted to PHENIX operating data. A larger fission product cross section yields a larger sodium-void reactivity since the larger absorption in the middle and low energy regions will reduce the adjoint flux at these energies making the slope more positive and thus increasing the non-leakage component. Hence, a reduction in the ANL fission product capture cross section consistent with the French data would decrease the calculated sodium void reactivity worth. Based upon such results, it seems conservative to assume that the sodium-void reactivity calculated from the reference fission product data has an uncertainty of ± 3%.

Table QCS760.178A2-3

NEACRP BENCHMARK SPECTRUM AVERAGED PSEUDO FISSION PRODUCT CAPTURE CROSS SECTION (barns)

Mean of All Participants*	.5002
St. Deviation	.0807
ANL	.5466
France	.4400
United Kingdom	.5200
Japan	.5613

*Only four of eight participants are shown in Table QCS760.178A2-3.

The zero-power experiments were performed with fuel temperatures near room temperature whereas the temperature in the CRBR may range from the normal operating conditions to much hotter in an accident scenario. Such variation in temperature is not represented in the sodium-void model. The main impact of raising the fuel temperature in a mixed oxide fueled core is to change the capture rate in ^{238}U and hence the shape of the adjoint flux and the magnitude of the real flux at resonance energies. The uncertainty in the sodium-void effect at high fuel temperature can be related to the room temperature results through the uncertainty in the Doppler reactivities. It is therefore possible to derive an additional uncertainty in the sodium-void effect at high

temperature relative to room temperature by applying the uncertainties in the Doppler effect. Such an analysis leads to an uncertainty of ~ 2.5% (Ref. QCS760.178A2-4).

Table QCS760.178A2-4 lists the percentage uncertainties due to effects other than those inherent in the calculational method. These uncertainties must be added with those given in Table QCS760.178A2-2 to give the total uncertainty.

Table QCS760.178A2-4

ADDITIONAL UNCERTAINTIES IN CRBR SODIUM-VOID REACTIVITY

Source	Uncertainty[a] % of Total Reactivity BOC-1	EOC-4
Fuel Rods Instead of Plates	0	0
Sequence of Voiding	3.5	3.5
Temperature Distribution	2.5	2.5
Fission Products	0	3.0

[a]To be added in quadrature with the values from Table QCS760.178A2-2.

Using the reference methods and the appropriate neutronics models, the sodium void reactivity was calculated for the BOC-1 and EOC-4 reactor configurations. Biased region-wise reactivity worths are given in Table QCS760.178A2-5. The data have also been processed in the form of SAS3D channel data to allow a comparison of these best-estimate predictions with earlier values used for CRBR safety analysis. In Table QCS760.178A2-6 the biased worths are compared with the values used in the CRBR analysis as documented in Tables 4-5 and 4-6 of Ref. QCS760.178A2-1. The large discrepancies can be attributed to differences in computational methodology; e.g., ENDF/B-II vs. ENDF-B/IV and First Order Perturbation Theory vs. Exact Perturbation Theory. While the differences may appear large, the new values, even with the uncertainties as discussed below, fall entirely within the uncertainty range documented in Ref. QCS760.A2-1.

Table QCS760.178A2-5

BEST ESTIMATE SODIUM VOID[a] REACTIVITY WORTHS ($)[b]

	BOC-1	EOC-4
Driver Assemblies		
Core	0.256	1.528
Lower Axial Blanket	-0.225	-0.160
Upper Axial Blanket	-0.177	-0.177
Total	-0.146	1.191
Internal Blanket Assemblies		
Core	1.381	1.593
Lower Axial Extension	0.008	-0.020
Upper Axial Extension	-0.007	-0.006
Total	1.382	1.567

[a]Void flowing sodium, within assemblies (82% of driver and 73% of blanket sodium removal per mesh cell.

[b]β = .0032

Whole-Core Analysis

To provide a measure of the sensitivity of predicted accident energetics to variations in the sodium void reactivity, the SAS3D analysis reported in the response to question QCS760.178A3 was repeated using the higher positive coolant voiding reactivity worths discussed above. The assumptions behind this case are identical to the best estimate EOC-4 case reported in Ref. QCS760.178A2-1, but with TREAT L6/L7 correlated fuel motion modeled as discussed in the response to QCS760.178A3. The EOC-4 core state was chosen because it has the highest positive coolant voiding reactivity effect, and would thus be the most likely to exhibit LOF-d-TOP behavior.

To establish an upper bound for the coolant void worth in the EOC-4 core, the uncertainties contained in Tables QCS760.178A2-2 and -4 were combined quadratically to yield a net uncertainty of 7.9% in the central core (positive reactivity) region, 11.3% in the external core (negative reactivity) region, and 20.7% in the axial and internal blanket regions. In each of the respective regions, an amount of positive reactivity corresponding to twice these uncertainties was then added to the biased, evaluated worth so that positive reactivities in the central core were increased by 15.9%, negative reactivities in the external core were decreased by 22.6% and positive and negative reactivities in the axial and internal blankets were increased and decreased,

Table QCS760.178A2-6 ACTIVE CORE REGION (91 cm) FLOWING SODIUM MATERIAL WORTH, DOLLARS[a]

SAS Channel Number	BOC1 Assembly Type	BOC1 Number Assemblies	BOC1 GEFR[b] 00523	BOC1 Current Best Estimate	EOC4 Assembly Type	EOC4 Number Assemblies	EOC4 GEFR[b] 00523	EOC4 Current Best Estimate
1	B	7	.056	.089	B	7	.100	.142
2	F	12	.096	.159	F	21	.386	.454
3	B	15	.152	.229	B	21	.330	.463
4	F	18	.191	.291	F	9	.160	.189
5	B	30	.373	.534	B	36	.559	.735
6	B	6	.068	.101	F	6	.085	.103
7	F	24	.144	.287	F	12	.165	.198
8	B	24	.303	.415	B	12	.125	.158
9	F	18	.090	.183	F	6	.027	.042
10	F	9	.002	.051	F	12	.113	.141
11	F	9	.002	.052	F	24	.366	.425
12	F	12	-.071	-.025	F	12	-.038	-.011
13	F	12	-.072	-.027	F	18	.116	.141
14	F	18	-.454	-.453	F	18	-.200	-.186
15	F	24	-.282	-.263	F	24	-.082	-.059
Total Driver		156	-0.354	0.255		162	1.098	1.438
Total Internal Blankets		82	0.952	1.368		76	1.114	1.498
Total Core		238	0.598	1.623		238	2.212	2.936

[a] β = .0034 value used for consistency in comparison with Ref. Q760.178A2-1.

[b] Ref. QCS760.178A2-1.

respectively, by 41.4%. The net results of these changes are summarized in Table QCS760.178A2-7 which shows the maximum positive (i.e., sum of all positive spatial values) coolant voiding reactivity as derived from the SAS3D EOC-4 input deck, the current best estimate biased worths, and the biased worths upwardly adjusted with uncertainties of 15.9%, 22.6%, and 41.4%. The most conservative result shows an effective increase of 31% in the driver subassemblies, 84% in the internal blankets, and 52% overall, when compared to the original void worths used in Ref. QCS760.178A2-1.

Table QCS760.178A2-7

COMPARISON OF MAXIMUM POSITIVE COOLANT VOIDING REACTIVITIES IN DOLLARS

Region	Ref. QCS760.178A2-1	Current Best Estimate	Current Best Estimate Plus 2 x Uncertainty	Net Increase Over Ref. QCS760.178A2-1
Driver	1.67	1.89	2.19	31%
Internal Blankets	1.12	1.45	2.06	84%
Total	2.79	3.34	4.24	52%

The event sequence predicted by SAS3D using the upwardly adjusted coolant void worths is given in Table QCS760.178A2-8. This event sequence can be directly compared to the event sequence given in Table QCS760.178A3-4 of the response to QCS760.178A3. As the comparison shows, increasing the void worths caused an increase in the maximum power and a shortened time frame for whole core involvement. Coolant boiling begins in every driver assembly before fuel in the hottest assemblies, channel 6, melts and begins to move. The core-wide voiding pattern just prior to the time of fuel motion initiation in channel 6 is shown in Fig. QCS760.178A2-1. As this figure shows, at the time of fuel motion in channel 6, complete core voiding of all the driver assemblies has been achieved in channels 2, 4, 6, 7, 9, 10, and 11. LOF-d-TOP type failures are thus ruled out in these channels. Partial voiding has occurred in channels 12, 13, 14, and 15, and failures into liquid sodium are therefore not ruled out. However, the core power is only a factor of ten above nominal power, and failure conditions are far from being met in these low-power channels. As time progresses, coolant voiding continues until fuel melting in driver channels 2, 4, and 7 at approximately 8.5 P_o leads to fuel dispersal and initial neutronic shutdown at 17 seconds following loss-of-flow initiation.

At the time of termination of the calculation, the core was subcritical and negative fuel motion reactivity was being added at a rate of -6.9 $/sec. The core-wide voiding pattern at termination is given in Fig. QCS760.178A2-2. This figure shows that at this point in time, all of the driver assemblies

Table QCS760.178A2-8

WHOLE CORE ANALYSIS RESULTS WITH ENHANCED COOLANT VOID REACTIVITY WORTHS*

Time	Event	CHN	P/PO	RHO	RHOD	RHOE	RHOV	RHOF	RHOC
11.9448	Coolant Boiling	6	0.891	-0.059	-0.168	-0.077	0.186	0.0	0.0
13.5350	Coolant Boiling	2	0.936	0.006	-0.193	-0.091	0.289	0.0	0.0
13.8150	Coolant Boiling	4	0.927	-0.011	-0.200	-0.096	0.286	0.0	0.0
14.2150	Coolant Boiling	7	0.920	-0.022	-0.210	-0.103	0.291	0.0	0.0
15.4115	Coolant Boiling	10	1.611	0.367	-0.276	-0.167	0.811	0.0	0.0
15.4365	Coolant Boiling	11	1.656	0.381	-0.280	-0.170	0.831	0.0	0.0
15.7603	Coolant Boiling	9	2.004	0.433	-0.332	-0.221	0.987	0.0	0.0
15.8382	Coolant Boiling	13	2.172	0.466	-0.345	-0.235	1.046	0.0	0.0
16.1720	Coolant Boiling	12	3.610	0.641	-0.406	-0.306	1.353	0.0	0.0
16.2195	Clad Motion	6	4.274	0.686	-0.421	-0.325	1.432	0.0	0.0
16.3095	Peak Reactivity	-	8.711	0.823	-0.476	-0.396	1.648	0.0	0.047
16.3555	Coolant Boiling	15	7.645	0.777	-0.514	-0.439	1.664	0.0	0.067
16.3979	Coolant Boiling	14	6.045	0.702	-0.540	-0.465	1.639	0.0	0.068
16.5470	Fuel Motion	6	9.827	0.788	-0.607	-0.534	1.889	0.0	0.040
16.6258	Peak Power	-	10.877	0.785	-0.656	-0.576	1.977	0.001	0.039
16.6938	Coolant Boiling	5	9.217	0.723	-0.695	-0.605	1.971	0.013	0.039
16.7034	Fuel Motion	7	8.728	0.705	-0.699	-0.607	1.958	0.015	0.038
16.7072	Fuel Motion	2	8.565	0.698	-0.701	-0.608	1.953	0.016	0.038
16.7097	Fuel Motion	4	8.460	0.694	-0.702	-0.608	1.950	0.017	0.037
16.7705	Fuel Motion	10	7.602	0.650	-0.723	-0.613	1.930	-0.051	0.107
16.7805	Fuel Motion	11	8.337	0.679	-0.726	-0.615	1.943	-0.046	0.123
16.7916	Coolant Boiling	3	9.123	0.705	-0.731	-0.616	1.953	-0.038	0.137
16.8286	Fuel Motion	9	6.722	0.590	-0.742	-0.619	1.952	-0.171	0.170
16.8911	Coolant Boiling	1	5.442	0.482	-0.751	-0.623	1.978	-0.348	0.226
16.8911	Coolant Boiling	8	5.442	0.482	-0.751	-0.623	1.978	-0.348	0.226
16.9855	Fuel Motion	13	2.519	-0.109	-0.748	-0.623	2.081	-1.089	0.270
17.0392	Clad Motion	2	1.649	-0.675	-0.735	-0.622	2.292	-1.883	0.271
17.1280	Termination	-	1.393	-0.981	-0.716	-0.620	2.647	-2.510	0.308

*Nomenclature is as follows:
CHN - SAS channel number.
P/PO - Core power relative to nominal.
RHO - Net reactivity in dollars.
RHOX - Reactivity in dollars due to Doppler (D), axial expansion (E), sodium void (V), fuel motion (F), and cladding motion (C).

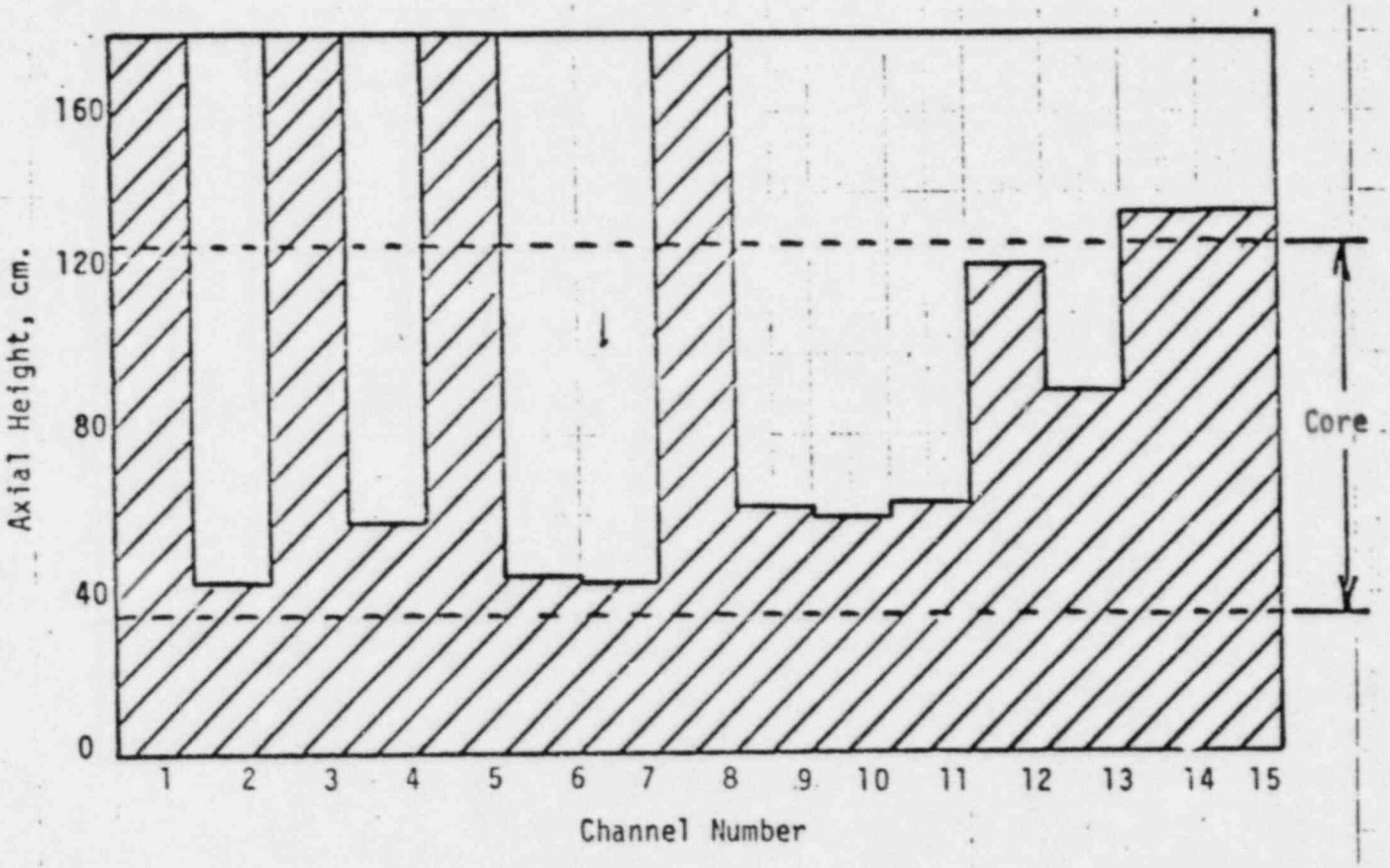

Fig. QCS760.178A2-1 Core Wide Voiding Pattern at Fuel Disruption in Channel 6.

QCS760.178A2-11

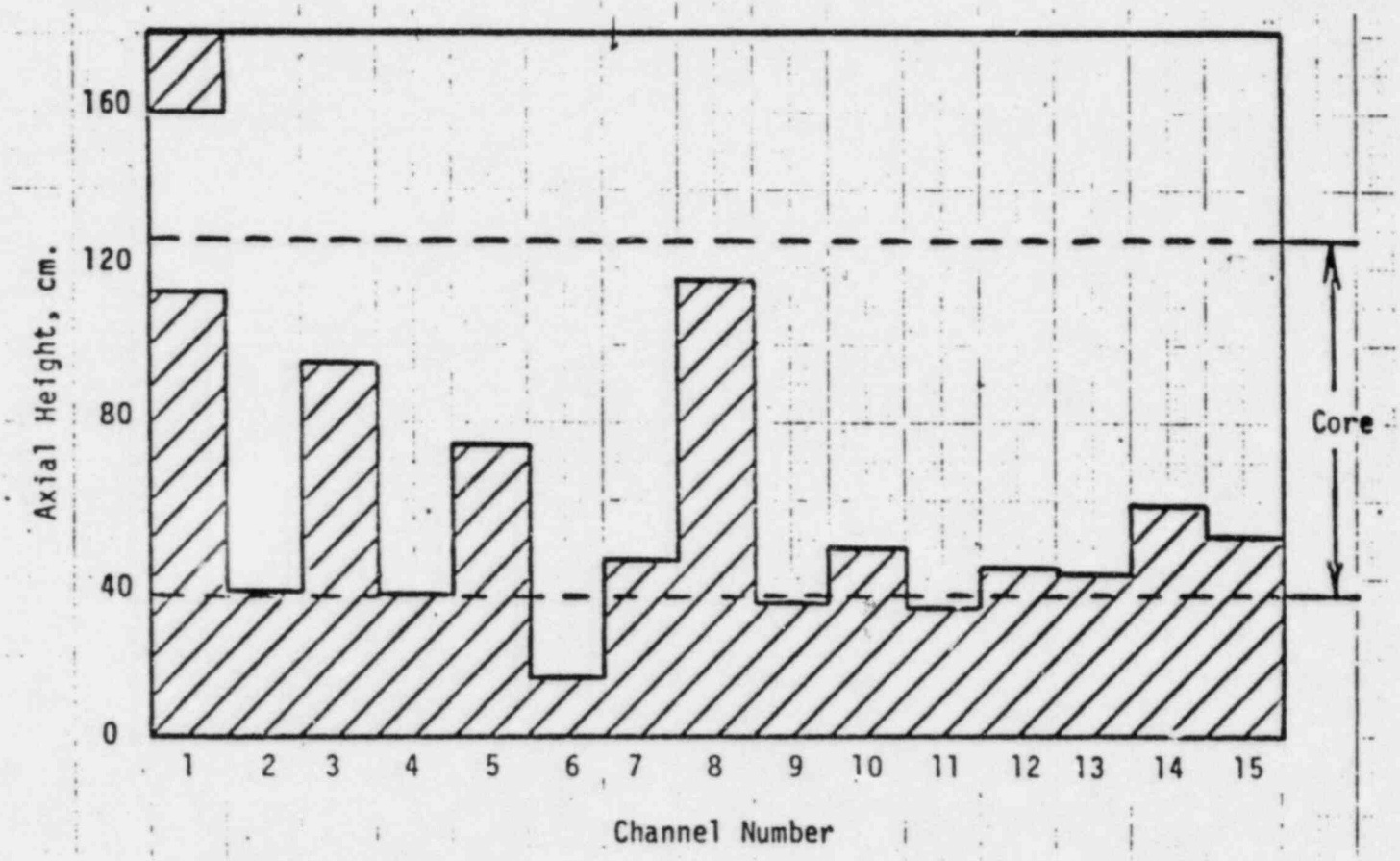

QCS760.178A2-12

Fig. QCS760.178A2-2 Core Wide Voiding Pattern at Termination.

have completely voided. In addition, internal blanket channels 1, 3, 5, and 8 have begun to void, and given the low power level, no subsequent blanket rod failures would be expected. Rather, continued coolant boiling would be expected, with the positive reactivity addition being offset by the negative fuel dispersal in the disrupted driver assemblies. At termination, the peak fuel temperature was less than 3500°C, and a gradual and benign entry into the melt-out phase would follow.

This analysis demonstrates that when appropriate and experimentally verified fuel motion behavior in voided assemblies is employed, conservative estimates of the uncertainties in the reactivity feedback associated with coolant voiding have little effect on predicted levels of initiating phase energetics. While some details (i.e., transient power levels, time scales, material motions) did change, no threshold for LOF-d-TOP events was found.

References

QCS760.178A2-1 S. K. Rhow, et al., "An Assessment of HCDA Energetics in the CRBRP Heterogeneous Reactor Core," CRBRP-GEFR-00523, General Electric Company, December 1981.

QCS760.178A2-2 C. L. Beck, et al., "Sodium Void Reactivity in LMFBRs; a Physics Assessment," APR-TM-400, Argonne National Laboratory, September 1981.

QCS760.178A2-3 J. D. Garrison and B. W. Roos, Nucl. Sci. Eng., 12, p. 115, 1962.

QCS760.178A2-4 A. T. D. Butland, W. N. Simmons, and J. M. Stevenson, "An Assessment of Methods of Calculating Sodium-Voiding Reactivity in Plutonium-Fueled Fast Reactors," Fast Reactor Physics 1979, Proceedings of an International Symposium on Fast Reactor Physics, Vol. 1, p. 281, Aix-En-Provence, pp. 24-28, September 1979.

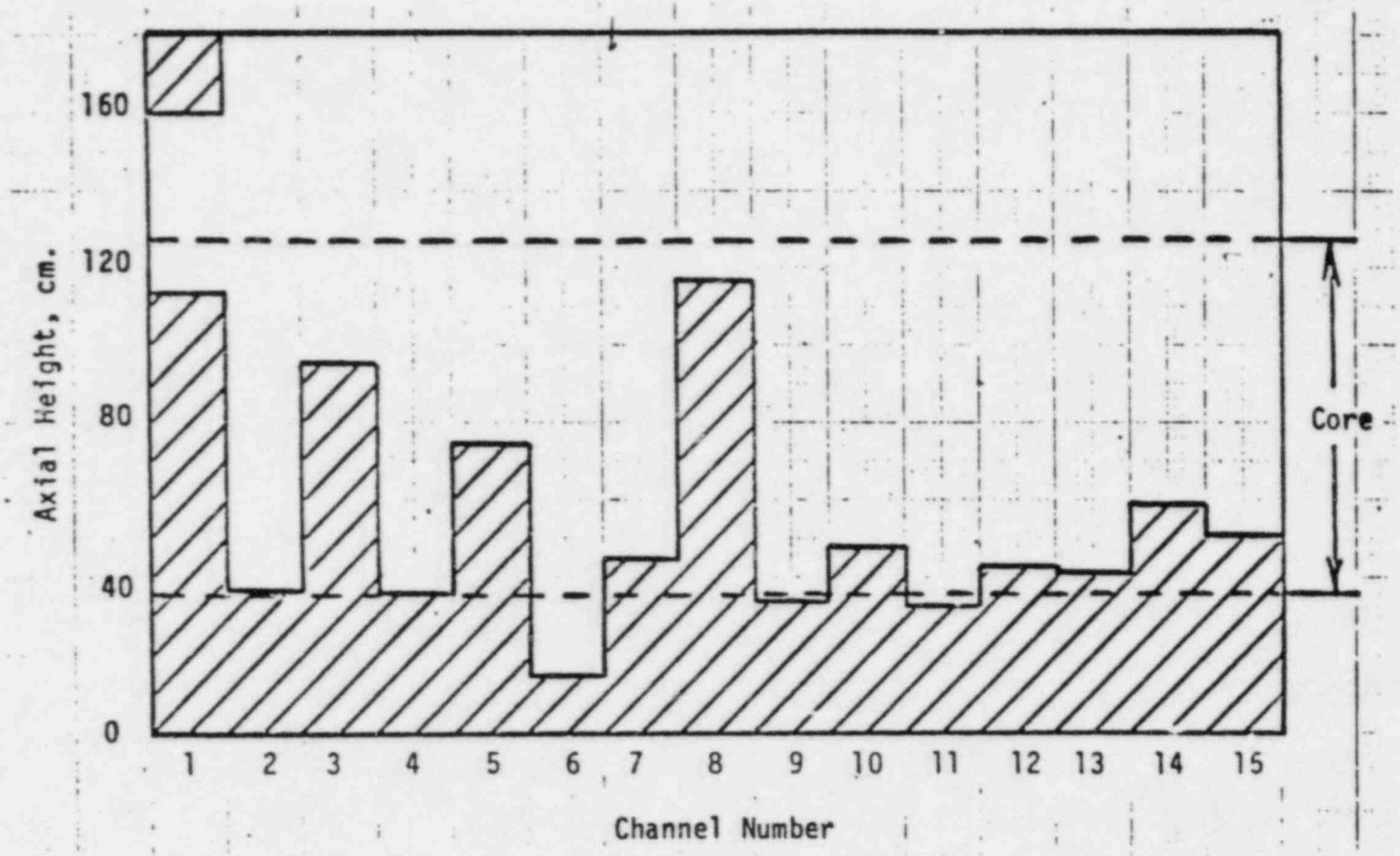

QCS760.178A2-12

Fig. QCS760.178A2-2 Core Wide Voiding Pattern at Termination.

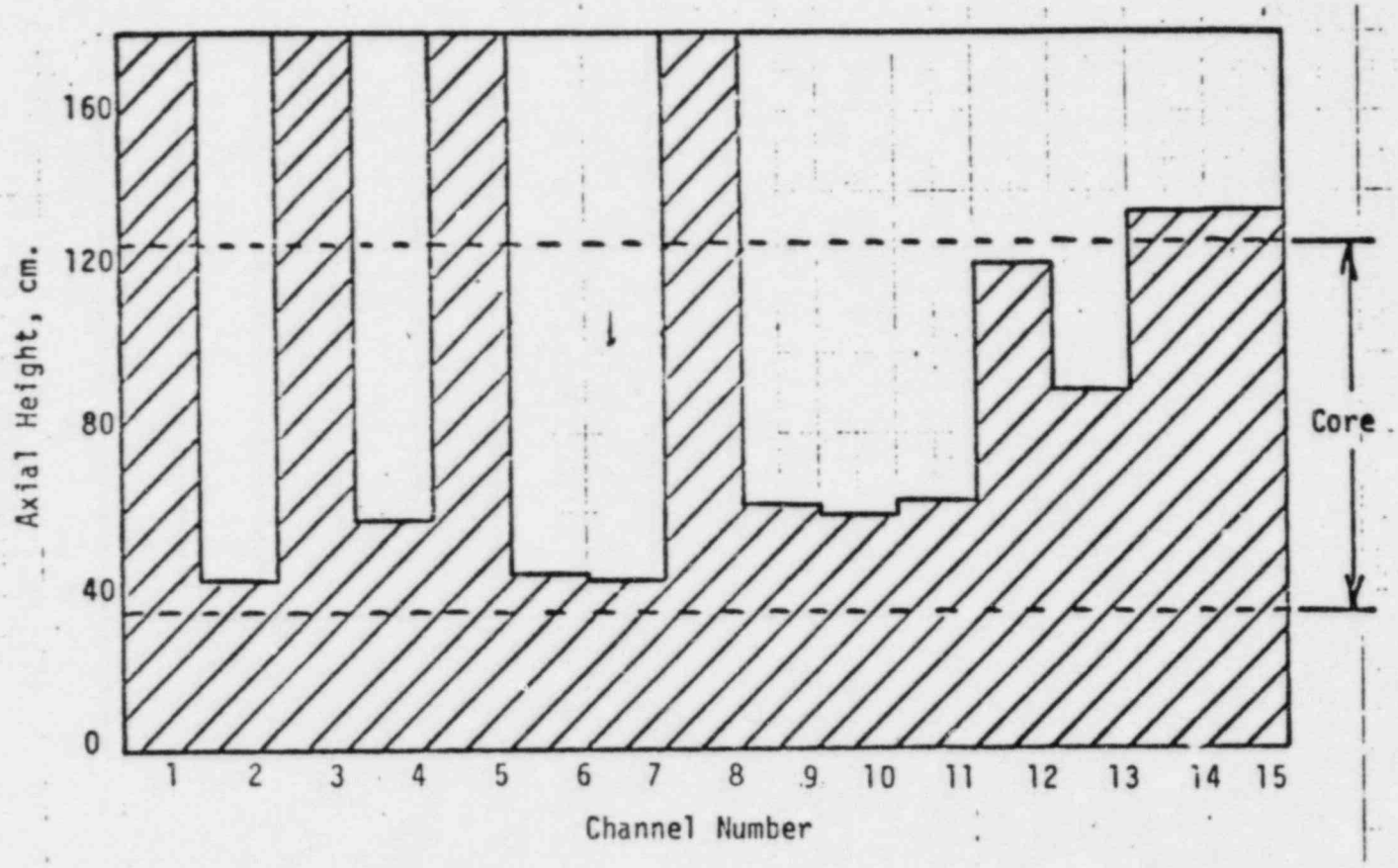

Fig. QCS760.178A2-1 Core Wide Voiding Pattern at Fuel Disruption in Channel 6.

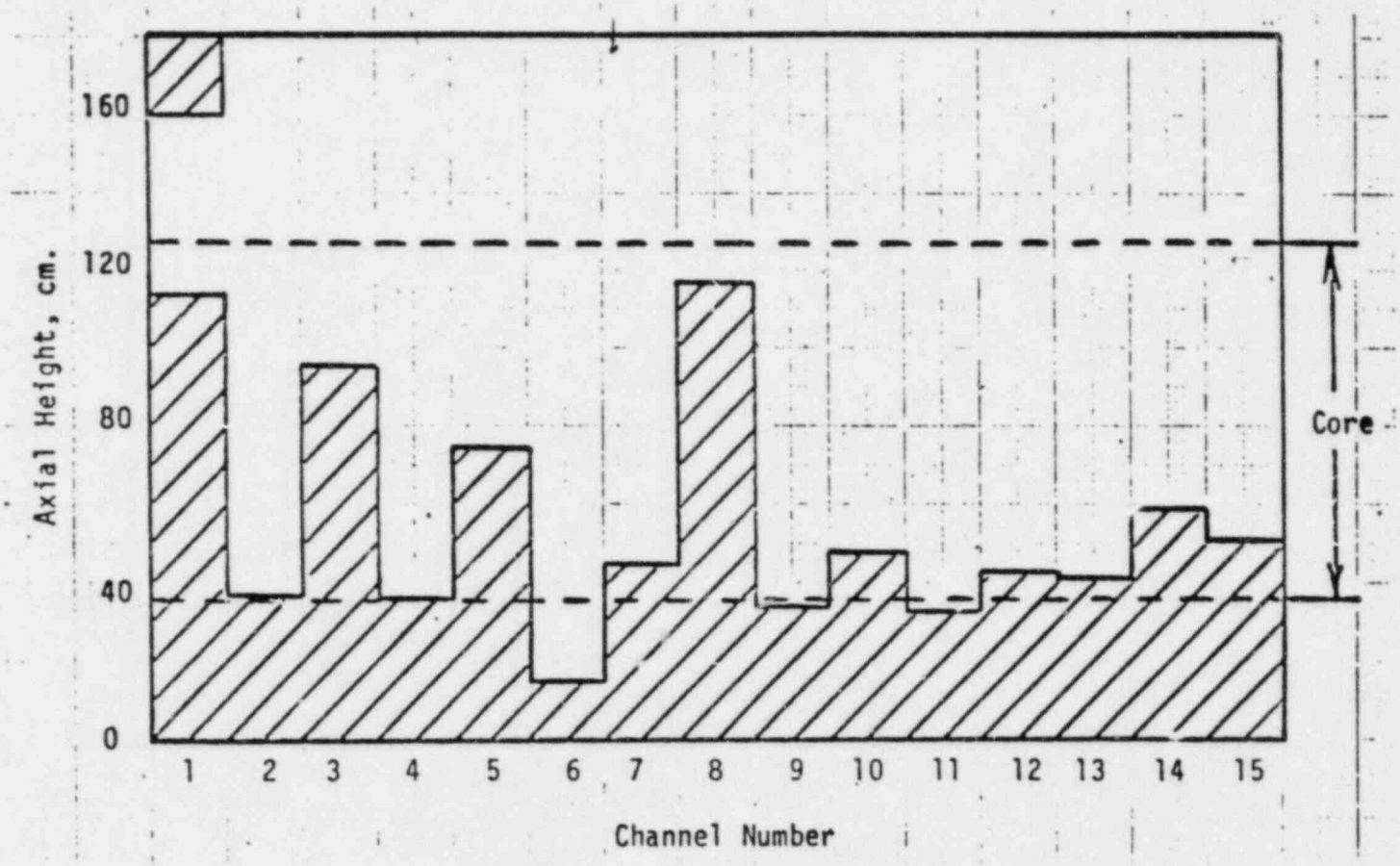

QCS760.178A2-12

Fig. QCS760.178A2-2 Core Wide Voiding Pattern at Termination.

have completely voided. In addition, internal blanket channels 1, 3, 5, and 8 have begun to void, and given the low power level, no subsequent blanket rod failures would be expected. Rather, continued coolant boiling would be expected, with the positive reactivity addition being offset by the negative fuel dispersal in the disrupted driver assemblies. At termination, the peak fuel temperature was less than 3500°C, and a gradual and benign entry into the melt-out phase would follow.

This analysis demonstrates that when appropriate and experimentally verified fuel motion behavior in voided assemblies is employed, conservative estimates of the uncertainties in the reactivity feedback associated with coolant voiding have little effect on predicted levels of initiating phase energetics. While some details (i.e., transient power levels, time scales, material motions) did change, no threshold for LOF-d-TOP events was found.

References

QCS760.178A2-1 S. K. Rhow, et al., "An Assessment of HCDA Energetics in the CRBRP Heterogeneous Reactor Core," CRBRP-GEFR-00523, General Electric Company, December 1981.

QCS760.178A2-2 C. L. Beck, et al., "Sodium Void Reactivity in LMFBRs; a Physics Assessment," APR-TM-400, Argonne National Laboratory, September 1981.

QCS760.178A2-3 J. D. Garrison and B. W. Roos, Nucl. Sci. Eng., 12, p. 115, 1962.

QCS760.178A2-4 A. T. D. Butland, W. N. Simmons, and J. M. Stevenson, "An Assessment of Methods of Calculating Sodium-Voiding Reactivity in Plutonium-Fueled Fast Reactors," Fast Reactor Physics 1979, Proceedings of an International Symposium on Fast Reactor Physics, Vol. 1, p. 281, Aix-En-Provence, pp. 24-28, September 1979.

after attack by the pool. A direct calculation of the timing for availability of the radial blankets has not yet been performed. However, based on the high heat fluxes expected, and Ledinegg instability, access to the radial blanket assemblies would be likely and within the time frame of the annular pool phase.

Freezing Mechanisms and Limits to Fuel Removal

Once escape paths become available, access to sufficient volume to assure permanent subcriticality can only be limited temporarily by fuel freezing. Experimental results were discussed in Ref. QCS760.178B5-1 which indicated the possibility for fuel penetration into the UAB - fission gas plenum region for distances on the order of 30 to 40 cm. The details of the applicable freezing mechanisms are as yet unresolved. A discussion of mechanisms is found in Appendix D to this response. It is noted that fuel would penetrate much larger distances if the conduction model were used as a basis and somewhat shorter distances than experimental results indicate if the "bulk" freezing model were applied. For UAB penetration, experimental results are presently used as a best estimate for fuel penetration into the UAB in the absence of prior cladding blockages. A pessimistic estimate is provided by the bulk freezing model which would limit fuel penetration to about the extent of the UAB itself ($\simeq$ 30 cm).

For interassembly gaps, the conduction theory as discussed in Appendix D is applied as a best estimate (including accounting for sodium flow impedance) while bulk freezing is used as a pessimistic basis. The primary control channel remains unplugged when tested against either conduction or bulk freezing models. On the other hand, plugging cannot be ruled out for the secondary control rod annular gap leading to the inlet orifice.

When either calculations or experimental results are applied to fuel escape paths it is found that (a) the PCA escape path remains unplugged and fuel escape is limited only by hydraulic considerations, (b) fuel penetration into the remaining escape paths, UAB and interassembly gaps, is in some cases individually insufficient to assure subcriticality. However, when collectively coupled with the PCA removal, these paths provide for fuel escape from the core region in sufficient quantity to assure permanent subcriticality.

Driving Pressures and Hydraulic Limitations

Once molten fuel moves out of the assemblies, the fuel will flow radially and downward into the open gaps. The gap flow area is small initially as only high power assemblies ($\sim$ 20%) are involved, and then increases as more fuel assemblies are involved. When all the fuel assemblies are involved (i.e., the molten pool reaches the core boundary), the total gap flow area is estimated to be roughly 3000 cm^2 at BOC-1 and 2500 cm^2 at EOC-4, assuming that only the gaps between the blanket and control assemblies remain open. The fuel-steel mixture in the assembly is in a dispersive state due to steel boiling. The pressure inside the assembly is expected to be 3-5 bars which is the steel vapor pressure at 3100 - 3200°C. The pressure in the gaps would be approximately 1.5 bar. Therefore, an initial pressure differential between the assembly and the gaps would be above 1.5 bar.

The effect of sodium impedance to fuel flow in the interassembly gaps is discussed in Appendix D. Based on the conduction model, sodium flow impedance will reduce the gap penetration by no more than 40%. This reduced penetration is still sufficient to accommodate all of the fuel required to assure permanent subcriticality on a time scale that is short (1 to 2 sec) relative to the time scale of the MO/APP.

The fuel temperature was previously estimated to be 3100-3200°C when the fuel assembly hexcan walls melt through. If fuel removal through the interassembly gaps is not sufficient for subcriticality, a molten fuel pool will be formed around the control assemblies, and the power will respond to assure boilup. Therefore, it is reasonable to assume that the molten pool temperature will be about the same as the fuel temperature at melt-through of the hexcan walls, i.e., 3100-3200°C. This temperature corresponds to a steel saturation vapor pressure of 3-5 bar. Since the inlet plenum pressure is approximately 2 bar at this point in the assumed flow coastdown transient, the differential pressure for fuel removal to the inlet module through the control assemblies can be assumed to be approximately 1.5 bar including a static head of 0.5 bar.

The rate of fuel removal from the core (i.e., below the core/LAB interface) is initially rapid until the molten fuel fills a space above the orifice region in the PCA's and the low pressure vent tube outlet of the SCA's. This space will be filled rather quickly after the hexcan walls (and the guide tubes in the case of secondary control assemblies) melt through. The volume of these spaces was estimated to be approximately 79 liters, which corresponds to $\sim$ 11% of the total fuel inventory (6000 kg). After filling the space above the PCA orifice region, the molten fuel will flow through the orifice plates into the inlet module and ultimately into the reactor inlet plenum. In the secondary control assemblies, the molten fuel may flow through the guide tube lower vent (Fig. QCS760.178B5-3) into either or both of the inlet module and out to the core barrel space. However, both of these later SCA paths were assumed to be unavailable because an assessment of the potential for plugging has not yet been performed.

The rate of fuel removal through the PCA orifice region to the inlet module can be estimated by utilizing design information on sodium flow in the PCA (Ref. QCS760.178B5-4). As shown therein, most of the pressure drop occurs through the orifice plates, and a sodium mass flow rate of 5.6 kg/sec per assembly was calculated for a pressure drop of 5.4 bar. Accordingly, based on the pressure drop and density ratios between the sodium flow and fuel flow, the fuel removal rate through the orifice region is calculated to be 9.6 kg/sec per assembly. For the nine PCA's, the total fuel removal rate is 86 kg/sec which corresponds to 1.4% of the total fuel inventory per second.

There are two major effects to be considered in the above estimate: fuel crust formation and two-phase flow (reduced density). The fuel crust reduces the orifice hole diameters, and the "steady-state" reduced hole diameter can be calculated on the basis of energy balance between convection at the crust surface and conduction through the crust. The heat transfer coefficient is calculated to be roughly 2 w/cm^2-°C, and with the fuel flow at 350°C above its liquidus the hole diameter is reduced from 1.07 cm to 0.94 cm. Using a new loss coefficient, determined for the reduced hole diameter based on design information provided in Ref. QCS760.178B5-4, the fuel removal rate was

recalculated. The total fuel removal rate was reduced from the above estimate by 15% due to the presence of the fuel crust.

Reduction of the flow density reduces the mass flow rate for a given pressure drop. When the flow density is reduced by a factor of 2 (void fraction = 0.5), the mass flow rate is reduced by 30%, i.e., from 1.4%/sec to 1% sec.

In summary, about 11% of the total fuel inventory can be removed into the primary and secondary control assemblies on a short time scale after melt-through of the hexcan walls. In addition, the fuel can be removed through the PCA orifice region into the inlet module and ultimately the reactor inlet plenum, at a rate of about 1% of the total fuel inventory per second even with consideration of the effects of fuel crust and reduced mixture density.

Termination of Accident Sequence

The material presented this far along with supporting appendices has developed the basis for (1) fuel removal paths are available, (2) fuel removal is significant even when assessed with either conservative models or experimental results, and (3) significant recriticality events cannot lead to energetic disassembly during the melt-out/annular pool phase.

From this information it follows that the CRBRP hypothetical core disruption accident terminates benignly and that because of the long time scale of the melt-out/annular pool phase the condition of a large scale homogeneous confined pool is not established.

The implications of the preceding discussions can be summarized in Table QCS760.178B5-5. This table shows the multiple paths for fuel removal and the extent of fuel removal that can be accommodated for BOC-1 and EOC-4 core conditions. Early fuel removal is associated with fuel escape dominated by interassembly gap flow as discussed in Ref. QCS760.178B5-1. This would occur on a time scale that is short (1 to 2 sec) relative to the time interval of the annular pool phase. The table also shows that with some reasonably pessimistic estimates relative to early fuel removal, but which at the same time avoid precluding clearly available pathways, permanent subcriticality can be attained on an extended time scale that is still within the time interval of the annular pool phase. Table QCS760.178B5-5 will be discussed by columns.

Upper Axial Blanket

The distinction between BOC-1 and EOC-4 core conditions is imbedded in the role of plenum fission gas on cladding blockages. For the BOC-1 core, cladding blockages cannot be precluded but will not be complete throughout the core. However, over the time scale of the MO/APP phase a best estimate would indicate some fuel removal but in quantities insufficient to lead to permanent subcriticality. A pessimistic estimate would take no credit for this removal path during the MO/APP phase. An important consideration of the UAB is introduced because of the extended time required to melt-out the inner blankets. Simple considerations of ablation melting of the UAB would indicate sufficient time is available to erode even rather thick (5 cm) cladding blockages in a time scale shorter than 100 sec. Thus, even if other mechanisms of fuel

Table QCS760.178B5-5 POTENTIAL FOR LOSS OF FUEL INVENTORY PRIOR TO MELT-OUT OF INNER BLANKET ASSEMBLIES

	Location	% Driver Fuel Inventory			Power Level and Time Interval Between Melt-Out/Annular Pool Phase and Homogeneous Pool Phase**
		Upper Axial Blanket and Radial Blanket	Interassembly Gaps	Control Rod Assemblies	
BOC-1	Early* Fuel Removal	< 10% (1) Based on Limited Opening in Clad Bkg.	> 40% Rate of Removal is Fuel Melt Limited	≈ 10%	10 to 5 w/g Bkt. Pwr. Level Initial Temp. 1000°C (avg) $\Delta\theta$ ≈ 150 sec
	Later* Fuel Removal	≈ 20% (1) No fuel Penetration into UAB - RB only	15% Based on BFM (2) and BOC Gaps	> 40% (3)	Time Interval Reduced by 1/4 Due to Driver Fuel Penetration into Bkt. Assembly $\Delta\theta$ ≈ 35 sec
EOC-4	Early* Fuel Removal	> 25% Based on Exp. Data Limited Clad Bkg.	> 40% Rate of Removal is Fuel Melt Limited	0% (4)	25 to 10 w/g Bkt. Pwr. Level Initial Temp. 2000°C (avg) $\Delta\theta$ ≈ 46 sec
	Later* Fuel Removal	> 40% Based on BFM (2) in UAB (25%) Plus (20%) into RB	> 10% Based on BFM (2) and EOC Gaps	> 30% (5)	Time Interval Reduced by 1/2 Due to Driver Fuel Penetration into Bkt. Assembly $\Delta\theta$ ≈ 23 sec

*Relative to the annular pool phase time interval.

**Defined by loss of inner blanket fuel assemblies structural integrity.

NOTES FOR TABLE QCS760.178B5-5

(1) Percent removal refers to short time scale following early fuel disruption. UAB is expected to be opened by thermal attack before large homogeneous pool is formed.

(2) BFM - Bulk freezing model. ORB - Outer Radial Blanket.

(3) The basis for > 40% is (a) 10% inventory to fill control rod channel, (b) plus draining through control rods at ≈ 1% 1 sec for as long as fuel supply lasts.

(4) No credit is taken for control channel volumes in the best estimate. Best estimate emphasizes early fuel removal through interassembly gaps.

(5) The basis for > 30% is (a) above and (b) draining through control rod channels at ≈ 1% 1 sec for ∿ 20 secs.

removal were denied, the UAB would be open by the time that a large homogeneous pool is established.

For the EOC-4 core plenum, fission gas release during the initiating phase will prevent upper steel blockage as demonstrated in the TREAT R-8 test (see Response to QCS760.178B4). A best estimate consideration would indicate essentially unlimited fuel penetration into the UAB on an assembly basis. While a pessimistic estimate would indicate a more limited penetration perhaps to the end of the blanket section. This is supported by either application of a bulk freezing model or relying solely on thermite injection test results. Again, a key consideration is that the subsequent melt-out of the upper blanket region accounting for fission energy can also occur on a 30 second time scale if fuel melting is used as a basis. The time scale for opening the UAB is much shorter if hexcan melting is visualized as the criterion for separation of blanket region from the fission gas plenum region. Again the above core structure is opened on a time scale less than or equal to the time to melt-through the inner blanket.

Interassembly Gaps

The interassembly gaps are also significant pathways for fuel removal. Essentially the total driver fuel inventory can be accommodated by radial flow outward (and downward) if a conduction limited fuel freezing (penetration model) is employed. This will not or need not occur on a one-to-two second time scale. The rate of fuel removal is found to be essentially supply limited. That is, fuel can only be removed as fast as melting occurs. Sodium impedance was evaluated and found at best to reduce unimpeded penetration length by ≈ 40%. This reduction does not alter the fuel removal inventory. Pessimistic estimates are based on the bulk freezing model and gap sizes for the BOC-1 and EOC-4 core respectively. In the latter cases, the fuel removal may be less than required to achieve permanent subcriticality, but none-the-less when added with other removal paths leads to the same result.

Control Rod Assemblies

The control rod assemblies (CRA) play a part in accommodating fuel removal in two ways. First, following melt-through into the voided assembly internals, the process of filling up the CRA from the inlet orifice to the lower axial blanket-core interface removes a fuel inventory of ≈ 10%. Second, drainage through the lower orifice region of the primary control rod assembly is assumed independent of freezing model. The drainage rate through 9 primary control rod assemblies is conservatively estimated to be within 1 to 2% of the fuel inventory per second. Thus even with the most pessimistic case sufficient fuel inventory is removed prior to inner blanket melt-out to assure permanent subcriticality. It is noted that the inlet orifice region of the secondary control rod assemblies cannot be assured to be free from plugging.

In Table QCS760.178B5-5 only that inventory of fuel associated with the CRA volumes above the inlet orifice is credited. This is to put the role of the CRA on a consistent basis with the best estimate and pessimistic estimate of the time scale for melt-out of the IB assemblies as discussed in the next section.

Time Scale and Power Level

The overall time scale and power level are interrelated. The best estimate is based on the assumption that driver fuel does not penetrate into the inner blanket region because of rapid removal through the interassembly gaps. The pessimistic time estimate assumes that because of limited fuel removal through the gaps, driver fuel enters the inner blanket fuel region and reduces the melt-out time by a factor of two (EOC-4) and a factor of four (BOC-1).

The average power level in the driver fuel is based on consideration that it is most probably; (1) above decay heat levels (10% of nominal power) because of mild recriticality events, (2) less than 50% of nominal power which should be sufficient to preclude recriticality on an assembly scale because of fuel dispersal, and (3) less than 20% of nominal power after assembly melt-through reduces the surface to volume ratio in the MO/APP. Since assembly merging occurs rapidly after dispersal, a power level of ≈ 30% of nominal, which is sufficient to assure fuel dispersal, is taken as a basis for the time to melt the IB assemblies.

Additional Considerations

In the pessimistic consideration above, driver fuel penetration into the inner blanket region, if it should occur, would also be accompanied by an equivalent penetration into the outer radial blanket. This would further reduce or accommodate an inventory of ≈ 20%.

Sensitivity

Various sensitivities have been indicated in Table QCS760.178B5-5. An additional sensitivity that is not explicitly presented is that of the details of the power history during the MO/APP. It is felt that the details of the power history are not important so long as large ramp rate recriticalities can be precluded. An increase in power level would shorten the time scale to melt-out the inner blanket regions but would have the off-setting effect of increasing the driving pressure for fuel removal and decreasing the UAB melt-out time.

Sodium Re-Entry

With multiple fuel escape paths operating in a surrounding liquid sodium environment the question of condensation induced sodium re-entry is natural. By analogy, transient condensation of steam contacting subcooled liquid water can result in sudden depressurization of the steam region and "suction" of the subcooled water toward the steam source. Such rapid condensation has been postulated to explain the occurrence of water hammers during accident transient simulations for pressurized water reactors. The concern has been voiced that, in a process similar to that mentioned above for steam, steel-vapor condensation on upper pool liquid sodium following melt-through of upper core blockages can cause the liquid sodium to be drawn back into the core. This water hammer which is certainly possible with respect to single component systems, is inapplicable to the two-component steel vapor-liquid sodium system because of the volatility of the liquid sodium surface and, therefore, the

participation of sodium vapor during the steel condensation process. A pressure reduction in the steel vapor region due to condensation is immediately compensated for by an equivalent pressure increase due to sodium evaporation.

The thermodynamic arguments are presented in Appendix E. The results of these arguments indicate that for the steel vapor, subcooled sodium liquid system a dual phase conversion process results in a vapor volume increase. For every one cubic cm of steel vapor condensed, 1.3 cubic cm of sodium vapor is produced, which significantly changes the character of the process in comparison with a one-component system such as steam and water. Sodium re-entry caused by rapid steel vapor condensation is not considered applicable to the accident sequence.

Response Summary

- While recriticality events cannot be ruled out during the MO/APP phase, these events are inherently mild because of flow regime and geometry considerations. Neither can such events escalate into larger amplitude prompt burst events. As a result of such mild recriticality events, the fuel maintains itself in a highly dispersed state at some low level above decay heat.

- Viable fuel removal paths exist in the UAB (for some core conditions), through interassembly gaps, through control rod assemblies and in some cases by melting into the outer radial blankets.

- In view of the variable and parallel nature of these removal paths the removal of sufficient fuel to assure permanent subcriticality is not overly sensitive to freezing mechanisms, sodium constraint, and viability of individual pathways.

- Removal of $\sim$ 40% of the total driver fuel inventory is sufficient to assure permanent subcriticality.

- Because of the above considerations, removal of sufficient fuel to assure permanent subcriticality can occur prior to melt-out of the inner blanket and formation of a large scale homogeneous pool.

- Even if such events were to occur without losing sufficient inventory, melt-out of the UAB would remove any constraint to the pool and provide another means for termination of the accident sequence.

- During the time when fuel loss is occurring, sodium re-entry is precluded as a source of pressure compaction of the annular pool material.

References to Response QCS760.178B5, -C6, -C7

QCS760.178B5-1 S. K. Rhow, et al., "An Assessment of HCDA Energetics in the CRBRP Heterogeneous Reactor Core," CRBRP-GEFR-00523, General Electric Company, December 1981.

QCS760.178B5-2 G. A. Greene, et al., "Heat Removal Characteristics of Volume Heated Boiling Pools with Inclined Boundaries," BNL-NUREG-51157, Brookhaven National Laboratory, April 1980.

QCS760.178B5-3 E. E. Morris and T. Y. C. Wei, "An Assessment of the Unprotected LOF Accident in the CDS Phase II Heterogeneous Core Design," ANL/RAS 81-1, Argonne National Laboratory, December 1980.

QCS760.178B5-4 D. Y. Nee, "Preliminary Thermal-Hydraulic Performance of CRBRP Preliminary Control Assemblies," CRBRP-ARD--0151, June 1977.

APPENDIX A TO: Question CS760.178B5, -C6, C7

Melt-Out of Inner Blanket Assemblies

The time required to melt out the inner blanket fuel assemblies is estimated from the following expression derived from an adiabatic energy equation:

$$\Delta\theta = \frac{(2800 - T_i) + \lambda/C}{\frac{FQ}{RC}} \qquad (1)$$

where $\Delta\theta$ is the time to melt in seconds, T_i is the initial blanket fuel temperature taken as the radial average at centerline or maximum conditions (°C), λ is the heat of fusion of fuel (278 j/g), C is the heat capacity of fuel (0.5 j/g °C), F is the fraction of nominal power for driver fuel, Q is the nominal power of driver fuel (150 w/g), and R is the ratio of driver fuel to blanket fuel.

For consideration of the melt-out phase the power level on the average will likely be bounded on the high side by 0.5 times nominal power which may be representative of a level sufficient to prevent recriticality by fuel dispersal in subassembly geometry and by ≈ .1 times nominal power representing the short time decay heat level. Thus F = .3 is taken as an average over the MO/APP phase. Utilizing (1) above, the following table indicates the results for:

	EOC-4	BOC-1
F	.3	.3
Q/C	300°C/s	300°C/s
λ/C	556°C	556°C
T_i	2000°C	1000°C
R	3	10
$\Delta\theta$	46 sec	150 sec

Melt-through of the hexcan walls within the core region results in the flow of molten fuel into the gaps; it could also result in the flow of molten fuel into the internal blanket assemblies. Upon entering the blanket assemblies, the molten fuel will fill the voided space between blanket rods. Heat transfer from the molten fuel to the blanket rods will cause the temperature of the blanket material to begin to rise at a rate greater than the adiabatic rate. An estimate of the maximum temperature rise rate $dT/d\theta$ within the blanket rods surrounded by molten fuel can be obtained by assuming that the

heat generated within the molten fuel is transmitted instantaneously to the blanket rods. This results in the expression

$$\frac{dT}{d\theta} = \frac{1 + \frac{\alpha}{1 - \alpha} R}{\frac{CR}{QF}} \qquad (2)$$

where α is the volume fraction of molten fuel ($\alpha = 0.24$).

In deriving Eq. (2), the transport of the sensible and latent (phase change) energy of the fuel melt to the blanket pins has been neglected. This is permissible since the temperature relaxation time within the blanket rod is approximately 35 sec and there is about four times more blanket rod material than molten fuel by mass. For the EOC-4 core, the ratio $[\alpha/(1 - \alpha)]R$ is $\sim$ 1.0. Thus we conclude from Eq. (2) that fuel entering the internal blanket assemblies can decrease the time to involve the internal blankets by no more than a factor of two. For the BOC-1 core the ratio $[\alpha/(1 - \alpha)]R$ is ≈ 3. Correspondingly, the time to involve the internal blankets can decrease by no more than a factor of four.

APPENDIX B TO: Question CS760.178B5, -C6, -C7

Considerations of Recriticality Events in the MO/APP of the CRBR Heterogeneous Core

Recriticality events subsequent to the initiating phase can occur. The geometric and the heat sink aspects of the boundary walls of high surface to volume ratio can give rise to fuel density increase. It is noted that motion of cold fuel material can be shown not to initiate large ramp rates. Reactivity insertion from motion of cold fuel are limited to several cents/subassembly/sec. The following discussions focus on the hydrodynamic aspects limiting fluid dynamic sources of large ramp rate recriticality events.

Recriticalities may not be precluded, in particular, shortly after termination of the initiating phase. To address this concern, a recriticality scenario is developed for the BOC-1 core by making pessimistic assumptions: (a) dispersed fuel in the high-power fuel assemblies collapses following the initiating phase power burst, (Ref. B-1), and (b) at the same time fuel in the medium-power fuel assemblies experiences a drainage-type collapse. The reactivity insertion rate associated with fuel compaction, which is the main concern in this pessimistic scenario, is estimated below.

In the case of fuel collapse in the high-power assemblies, the dispersed fuel will settle down displacing the vapor. The collapse rate will be controlled by the rate of vapor separation to the region above the pool. Since the flow regime is expected to be liquid continuous toward the end of the collapse, the terminal rise velocity of vapor bubbles can be used as the rate of pool collapse as indicated in Ref. B-2. This terminal velocity in a fuel-dominant pool was calculated to be 23 cm/sec.

The high-power fuel was assumed to be uniformly dispersed prior to collapsing. The reactivity level of the core was first calculated based on these conditions to establish the reference initial reactivity level. Then, the reactivity due to collapse of the pool was calculated by lowering the pool height. It was assumed that the fuel in all the high-power assemblies (channels 9 and 11 in Ref. B-1) is collapsing simultaneously at the same rate. The results of this reactivity calculation produces a ramp rate of about 10$/sec.

Fuel in the medium-power assemblies (57) has disrupted and is assumed to be experiencing a drainage-type collapse at termination of the initiating phase analysis. This type of fuel collapse will result in a reactivity insertion at a rate of about 20¢/sec per assembly based on TREAT test data. Thus, the simultaneous fuel motion in the medium-power assemblies is expected to produce a ramp rate of about 10$/sec. Therefore, the total ramp rate due to pool collapse in the high-power assemblies and fuel drainage in the medium-power assemblies could be no greater than 20$/sec, which is below the range for which hydrodynamic disassembly of the core is expected*. Thus, it is concluded that fuel compaction would simply expedite the accident progression

*Less coherent behavior would correspondingly reduce the magnitude relative to these estimates.

by maintaining power between decay heat level an ≈ .5 times nominal leading to a permanent subcriticality without an energetic power burst. The response to mild recriticality events is now considered.

Early in time, in response to the power source, the molten fuel flows toward the axial ends of the subassembly in the form of two intact slugs. The liquid slugs are accelerated under the action of the expanding high pressure fuel and/or steel vapors at the center of the subassembly. The occurrence of fluid mechanical instabilities, however, will cause the low-density high pressure vapor region to penetrate and mix with the more dense accelerating slugs. At any location after the lower vapor-liquid fuel interface has passed, the heavier molten fuel is not completely expelled or replaced by the lighter vapor. A thick film of molten fuel will adhere to the subassembly wall while a tongue(s) or finger(s) of the vapor of reduced diameter advances through the center established by the portion of the fuel melt left behind. Moreover, atomization of the fuel film and the wave(s) or spike(s) produced at the lower (unstable) fuel interface will occur by direct action of the expanding vapor region. These processes result in the disintegration of most of the mass of the molten fuel and rapidly transform the postulated fuel slug into a two-phase annular-drop flow. The molten fuel and steel left behind in the form of entrained drops and liquid film in the axial midplane region results in the evaporation of the molten material in this region, the transport of the vapor along the length of the subassembly and the subsequent condensation of the vapor upon relatively cold fuel surface (drops and film) at the axial ends of the subassembly.

If the vapor flux is large enough to maintain the fluid-mechanical balance between interfacial drag and the mass of the fragmented fuel, the dispersed annular flow regime will endure and dominate the boiling process within the disrupted subassembly. On the other hand, suppose we assume that the vapor flux is continuously reduced until it falls below that required to maintain fuel-steel boiling. Clearly, then, the pool will contract and ultimately return to its collapsed configuration, passing successively through the annular drop, churn turbulent and bubbly flow regimes as the vapor flux is reduced. The pool collapse rate will be limited to the bubble rise velocity within the bubbly flow regime. This velocity is less than 30 cm/sec and is too low to produce anything but a mild recriticality. Thus the breakup of the accelerating fuel slugs within a single subassembly eliminates the possibility of severe fuel collapse rates and, therefore, eliminates the amplification of mild recriticalities into super prompt critical bursts.

The physical process that leads to the breakup of the accelerating fuel slugs is the well known Taylor instability (B-3). It has been shown by Taylor that a plane interface between two fluids of different densities in accelerated motion is unstable as long as the acceleration is directed from the lighter to the heavier fluid. The high pressure side of an accelerating fuel slug in a single subassembly is subject to breakup by means of this type of instability, since its motion is largely one dimensional. For simplicity, attention will be focused on a single accelerating fuel slug, as illustrated in Fig. B-1. The theoretical considerations that follow below are necessarily quite imprecise. It is understandable that phenomena so complex as finite-amplitude wave development cannot be analyzed accurately. These simple results constitute order-of-magnitude estimates. Moreover, the analysis does not take into account fuel vaporization or condensation at the liquid fuel

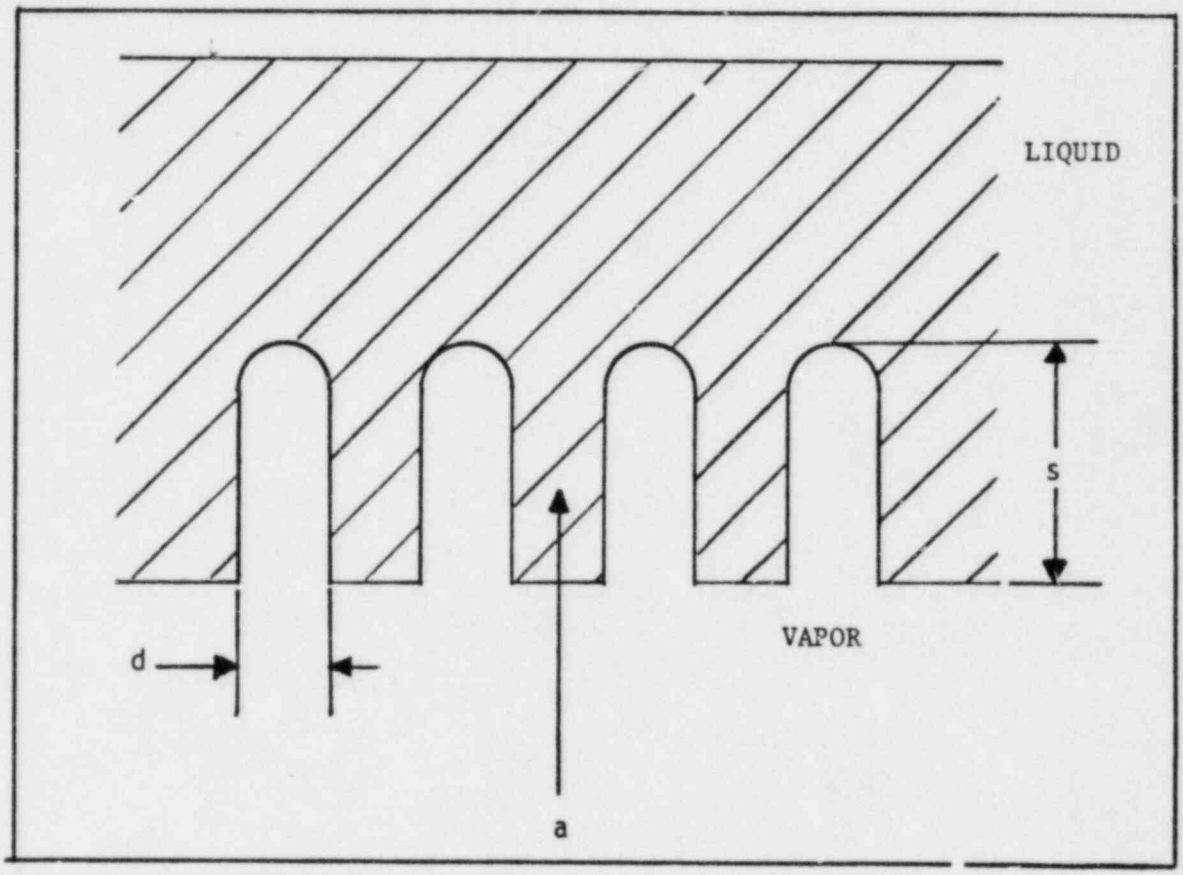

Fig. B-1 Schematic Illustration of Accelerating Fuel Slug.

interface or the deposition of molten material on the subassembly walls, which certainly will modify the results quantitatively (see below).

The Taylor instability has been observed under a wide variety of experimental conditions, and the initial phase of the instability has been found to agree well with linearized wave theory. The experimental results may be interpreted roughly as showing that the instability follows the first-order theory during the time

$$\tau = \sqrt{\lambda/a} \tag{1}$$

where λ is the wavelength of the disturbance and "a" is the acceleration of the liquid slug. Typically, under reactor accident conditions, $\tau \approx 10$ msec. It therefore appears that the initial development of the instability is of little interest. The succeeding stages of the instability consist of round-ended columns of gas or vapor penetrating steadily through the liquid with little change of profile (see Fig. B-1) until the opposite surface of the liquid slug is reached causing the slug to burst. In spite of the presence of these gas columns, the main body of the liquid slug is accelerated as though they did not exist. The gas columns penetrating into the accelerating slug have been found to move relative to the liquid at a constant velocity v given by

$$v \simeq \sqrt{ad} \tag{2}$$

where d is the diameter of the penetrating gas column. Thus the penetration distance s of the column into the slug (Fig. B-1) after time t is given approximately by

$$s \simeq \sqrt{ad \cdot t} \tag{3}$$

Clearly, the distance z travelled by the liquid fuel slug during this time is

$$z = \frac{1}{2} at^2 \tag{4}$$

Eliminating t between Eqs. (3) and (4) yields an expression for the column penetration distance in terms of z:

$$s \simeq \sqrt{2zd} \tag{5}$$

Equation (5) has a very simple interpretation as a fuel slug breakup criterion. It predicts that only the diameter of the gas columns and the instantaneous location of the accelerating fuel slug influence the breakup of the slug, which should occur when s equals the axial thickness of the fuel slug. To complete the application of Eq. (5) to an accelerating fuel slug in a reactor subassembly, one need only estimate the diameter of the fuel (or steel) vapor columns. Here we must rely on experimental observations. Photographs of the process indicate a progressive change early in the acceleration transient from a number of surface waves and troughs to a much smaller number of troughs until only one or two round-ended columns of gas remain and penetrate the liquid slug. Thus taking d to be of the order of the radius of the subassembly duct ($d \simeq 5$ cm) we find from Eq. (5) that columns of core vapor will penetrate approximately 22 cm into the fuel slug after the

slug has traversed one-half of the active core length ($z \sim 50$ cm), as compared with the slug depth which is typically between 10 and 20 cm.

It should be mentioned that Fig. B-1 falls far short of describing the later stages of development of the Taylor instability. The penetrating gas (vapor) columns compete with one another, the large ones growing at the expense of the small ones. A large quantity of liquid is left adhering to the sides of the channel (subassembly), with the result that the vapor penetrates through the fuel slug at a faster rate than that given by Eq. (2). The vapor-liquid regions on the sides of the spikes (or film) and vapor columns are in relative motion which produces additional surface instability of the Helmholtz type. In particular, the final stage of mixing between liquid fuel and vapor is too complex for detailed description. The important point to be made here, however, is that it is apparent from the preceding discussion that conditions conducive to the breakup of accelerating fuel slugs in subassembly geometry exist following a power burst.

The obvious question of concern is how large can a fuel pool be before its response to a power or pressure source is dominated by radial motion of the liquid fuel rather one-dimensional expansion as previously discussed. Our focus here is to attempt to identify the threshold pool size above which purely dynamic fuel motion is possible.

Let us consider a spherical cavity of instantaneous radius R containing fuel or steel vapor at high pressure suddenly formed as a result of a power burst along the axial centerline of a cylindrical pool of molten fuel of diameter D and instantaneous height H (see Fig. B-2). The initial height of the pool is designated by H_o. The constancy of molten fuel volume within the pool requires that

$$\frac{1}{4} D^2 H_o = \frac{1}{4} D^2 H - \frac{4}{3} R^3 \tag{6}$$

Differentiating this expression twice with respect to time gives the following relation between the instantaneous acceleration of the bubble interface and that of the surface of the pool:

$$\frac{1}{4} D^2 \frac{d^2H}{dt^2} = 4R \left[R \frac{d^2R}{dt^2} + 2 \left(\frac{dR}{dt} \right)^2 \right] \tag{7}$$

The initial phase of the bubble growth and pool expansion is controlled by the inertia of the liquid that completely surrounds the bubble. The bubble is blown up according to the Rayleigh equation for radial motion

$$R \frac{d^2R}{dt^2} + 2 \left(\frac{dR}{dt} \right)^2 = \frac{P - P_\infty}{\rho} \tag{8}$$

where P is the pressure within the fuel vapor bubble, P_∞ is the ambient pressure above the fuel pool and ρ is the density of the molten fuel. Equation (8) is an approximate form of the Rayleigh equation which gives reasonable solutions for inertia-controlled bubble growth. Strictly speaking, the

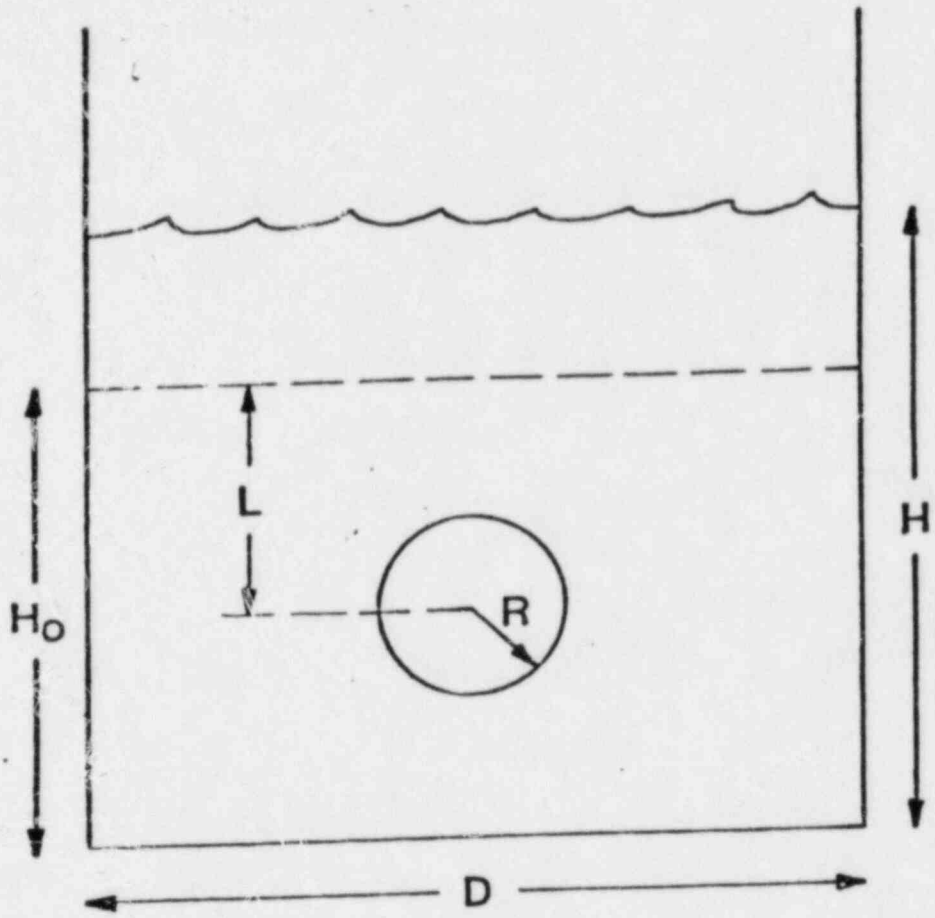

Fig. B-2 Pool Geometry with "Initial Bubble".

coefficient of the second term in Eq. (8) should be 3/2. Eliminating the radial acceleration terms between Eqs. (7) and (8) yields

$$\frac{D^2\rho}{16R}\frac{d^2H}{dt^2} \simeq P - P_\infty \tag{9}$$

Equation (9) simply expresses the law of motion governing the expansion of the fuel pool when the motion within the pool is three dimensional and little mixing occurs between the expanding vapor cavity and the surrounding molten fuel. While the early expansion is essentially radial, ultimately the growing fuel cavity will "feel" the presence of the vertical wall that contains the pool. The pressure will tend to become uniform across the width of the pool (within the vapor space) and the pool expansion may then be adequately treated as one dimensional. During this period the pool growth is well represented by

$$\rho L\frac{d^2H}{dt^2} \simeq P - P_\infty \tag{10}$$

where L is approximately the initial depth of the bubble center (assumed stationary in time) below the surface of the pool, or, equivalently, the thickness of the fuel slug that is accelerated upward during the one dimensional expansion phase.

For the one dimensional expansion, the appropriate liquid inertia is proportional to the mass of the liquid above the bubble center, or ρL. The effective liquid inertia for the early spherical expansion follows from Eq. (9) and is $D^2\rho/16R$. It is reasonable to suppose that the pool expansion is dominated by one dimensional fuel flow when the "one dimensional inertia" becomes somewhat greater than the "spherical inertia", i.e., when $\rho L \gtrsim D^2\rho/16R$, or

$$R \gtrsim \frac{D^2}{16L} \tag{11}$$

As a numerical example, suppose we consider fuel-pool motion following a power burst at L = 25 cm below the surface of, say, a 50 cm deep pool. The pool is assumed to be about two subassemblies in cross-sectional area, or D ≈ 20 cm. Owing to the discrete control subassembly and blanket assembly array within a heterogeneous core, this value of D corresponds to about the largest radially unimpeded region of molten fuel that can form during the MO/APP within the CRBRP. From criterion (11), we calculate that when the radius of the power burst bubble is of the order R ≈ 2 cm the pool expansion becomes one dimensional. It is of interest to note that during the spherical growth period we calculate using Eq. (6) that the pool surface rises only 0.1 cm. Thus, for all practical purposes, the pool response to a power burst is one dimensional and subject to the instabilities discussed previously for a single subassembly. The fuel-steel boiling process within a disrupted heterogeneous core should therefore be stable to mild recriticalities.

References for Appendix B to QCS760.178B5-C6, C7

B-1 S. K. Rhow, et al., "An Assessment of HCDA Energetics in the CRBRP Heterogeneous Reactor Core," CRBRP-GEFR-00523, General Electric Company, December 1981.

B-2 T. G. Theofanous, "Multiphase Transients with Coolant and Core Materials in LMFBR Core Disruptive Accident Energetics Evaluation," NUREG/CR-0224, Purdue University, July 1978.

B-3 G. I. Taylor, Proc. Roy. Soc., London, A201, p. 192, 1950.

APPENDIX C TO: Question CS760.178B5, -C6, -C7

Reactivity Calculations for Various Configurations of Disrupted BOC-1 Core

This appendix documents neutronics calculations which were performed to evaluate reactivity levels for the disrupted core configurations at BOC-1.

The primary objective throughout this neutronics analysis has been to retain as much rigor in the computational modeling as possible while retaining efficient computations. For significantly disrupted core configurations, as are encountered in the melt-out and large-scale pool phase analysis, the presence of large internal voids makes the use of diffusion theory suspect. In order to adequately handle the complex streaming associated with large internal voids S-4 transport theory with isotropic scattering was selected as the computational mode. The use of S-4 transport theory in RZ geometry will adequately handle the isolated blanket islands and control rods while giving the benefit of a rigorous treatment of the internal voids.

The basic cross-section data used for the neutronics analysis were generated from the ENDF/B-IV data files (Ref. C-1). The MC^2-SDX (Refs. C-2 and C-3) code package was used to process these data. A base library of 171-groups ($\Delta u = 0.1$) was generated using a weighting spectrum from a 2040-group slowing down calculation for an appropriate Pu/U fueled LMFBR core composition (Ref. C-4). Special care was taken in generating ^{238}U blanket cross-sections. A blanket fine-group library was obtained using the core leakage as an external source for the blanket slowing down problem. Using the combined fine-group base library, broad group libraries were generated with the SDX code. Resonance self-shielding effects were accounted for in voided and non-voided driver, internal blanket, and radial blanket assemblies. An eight group and a twenty group library were obtained for operating conditions (1500°K) and for an elevated temperature (3000°K). Table C-1 shows both group structures. The reference CRBRP design and BOC-1 masses are taken from the CRBRP PSAR and are given in Table C-2. Corresponding to the best-estimate core conditions at termination of initiating phase analysis, a full RZ model for the BOC-1 core was constructed as shown in Fig. C-1. This model represents the base case for disrupted core neutronics calculations.

Three disrupted core configurations were analyzed. In all cases, one-third of the cladding and wire wrap in all fuel assemblies is assumed to relocate into the UAB region. Another one-third of the cladding and wirewrap is relocated into the LAB region. The remaining residual steel including the hexcan walls is assumed to be homogenized with the molten fuel.

Conditions of the core are assumed to be as described in the main text, (Table QCS760.178B5-4) and the fuel removed from the core is assumed to be distributed as follows: 11% in the below-core region, 6% in the radial blanket region, and the remaining fuel removal in the radial shield region. In Case 3 where a core-wide pool is formed with control assemblies available for fuel removal, an additional 8% of the total fuel is assumed to be relocated into the control assemblies.

Table C-1

GROUP STRUCTURE FOR 8 AND 20 GROUP
CROSS SECTION LIBRARIES

Broad Group Energy, ev	20 Group Library	8 Group Library
1.0000×10^{7}	1	1
3.6788×10^{6}	2	
2.2313×10^{6}	3	
1.3534×10^{6}	4	2
8.2085×10^{5}	5	
4.9787×10^{5}	6	3
3.0197×10^{5}	7	
1.8316×10^{5}	8	4
1.1109×10^{5}	9	
6.7380×10^{4}	10	5
4.0868×10^{4}	11	
2.4788×10^{4}	12	6
1.5034×10^{4}	13	
9.1188×10^{3}	14	7
5.5309×10^{3}	15	
3.3546×10^{3}	16	8
2.0347×10^{3}	17	
1.2341×10^{3}	18	
4.5400×10^{2}	19	
6.1442×10^{1}	20	

Table C-2

HEAVY METAL* MASS INVENTORY (kg) FOR CRBRP BOC-1

Fission Produces	Driver	Inner Blankets**	Radial Blanket**	Axial Blankets
^{239}Pu	1468.0			
^{240}Pu	199.7			
^{241}Pu	34.0			
^{242}Pu	3.4			
^{235}U	7.6	16.7	26.9	8.6
^{238}U	3476.0	8253.0	13285.0	4216.0
Fission Products	-	-		
Total Heavy Metal	5188.7	8269.7	13311.9	4224.6

*Heavy metal excludes oxygen.

**Includes axial extensions.

Question CS760.178A3

What is the potential for autocatalysis due to plenum fission gas acting on the fuel column to force axial compaction as disruption occurs in the initiating phase of the LOF?

Response

An assessment of this question resulted in the conclusion that the potential for fission gas induced compaction in the CRBRP is negligible, due to the release of the gas into the coolant channel prior to fuel column disruption.

The heterogeneous core design minimizes concern for a range of accidents involving autocatalytic behavior because of the substantial reduction in the sodium void worth in the driver assemblies and the significant incoherence in thermal-hydraulic response at EOC-4 conditions. To provide a resolution to this question, a comprehensive examination of the important physical phenomena and their implication on the assessment of whole core behavior was performed. Included in this examination was a phenomenological review of the response of the plenum fission gas to both cladding failure (depressurization) as well as fuel column compaction during the accident scenario described in Ref. QCS760.178A3-1. In addition, it was recognized that the potential for the plenum gas compaction problem may have been exaggerated by the use of known conservative assumptions in the modeling of fuel dispersal after rod disruption (Ref. QCS760.178A3-1, Section 7.2.1). Thus, a review of relevant experimental information, a detailed examination of critical phenomenology, and a modeling effort to describe fuel motion consistent with the experiments were performed concurrently. With such an assessment providing the justification for fuel dispersal modeling, the whole core dynamic response was re-examined with the SAS3D code.

A preliminary assessment of the physical phenomena associated with potential plenum fission gas effects led to several conclusions. Among the most important of these are: (1) the fission gas plenum pressure is not likely to cause fuel motion to initiate earlier than would be expected based on fuel motion thermal criteria, (2) unless the plenum and upper axial blanket cladding can move far enough upward to clear the blanket fuel pellet stack, such motion will not reduce the plenum pressure sufficiently to preclude influence on fuel motion, (3) the gap between blanket cladding and blanket fuel pellets is expected to remain sufficiently open and free of fission products so that neither gas release through the gap to a cladding failure farther down on the fuel rod nor downward motion of the blanket pellets will be restricted, and (4) the timing of events in the CRBRP best estimate analysis (Ref. QCS760.178A3-1) is such that plenum fission gas influence on fuel motion in some of the later-failing channels (starting with channel 11) might be possible.

The approach taken in this report is to reassess the experimental bases to support a less conservative fuel motion modeling than used in the previous CRBRP analysis. In performing the reassessment, particular attention is paid to the TREAT L6 and L7 LOF experiments which are used to calibrate the SAS 3D/SLUMPY fuel motion model for use in whole-core accident analysis. The SAS3D experiment and whole-core analyses are supplemented with FRAS3 (Refs.

QCS760.178A3-2, -3, -4) calculations to establish the amount of fission gas that is likely to be present in the fuel and available to assist in fuel dispersal following the onset of fuel motion. It is concluded that an experimental-analytic bases can be defined to support more realistic lead fuel channel response to the LOF conditions. When the more realistic modeling is used, it is found that all channels have time to release enough plenum fission gas prior to fuel motion to remove this potential fuel compaction mechanism.

In the remainder of this report, the TREAT LOF tests which have been conducted during the past several years will be briefly characterized. Then the FRAS3 code which provides the basis for estimating the amount of fission gas available to participate in fuel motion will be reviewed. Next, the SAS3D analyses of the L6 and L7 TREAT tests and the CRBR LOF scenario will be described. Finally, some of the sensitivities and uncertainties found in both the test analyses and the whole-core calculations will be identified.

Experimental Basis

A listing of LOF experiments carried out in the TREAT reactor is made in Table QCS760.178A3-1 (Ref. QCS760.178A3-5). Fuel motion in these experiments was monitored using the fast neutron hodoscope (Ref. QCS760.178A3-6). Although all of these tests are pertinent to the understanding of LOF transients, tests L6 and L7 were selected as the database for calibrating SAS3D/SLUMPY because only tests L6 and L7 were performed using (1) irradiated fuel, (2) nearly meter-length fuel pins, and (3) a 1.2-meter hodoscope collimator viewing height.

From a review of the results of all the tests listed above, it is possible to make some general observations. For the tests that were conducted at nominal power, it was found that fuel which had been irradiated long enough to accumulate a significant gaseous fission-product inventory compacted at a slower rate and to a lesser extent than fresh fuel at the time of melting. When the power levels were at 6 times nominal or higher, the test results indicated dispersive tendencies. It is judged that fission gas was an important contributor to both the slower rate of compaction observed in irradiated fuel at nominal power and the dispersive tendencies observed in the higher power tests.

The L6 and L7 tests were designed to simulate accident conditions that were identified in SAS3D analyses of the CRBRP homogeneous design. The fuel rods used in the tests were irradiated in a thermal-neutron spectrum at a peak linear power of 36 kW/m to a peak burnup of about 3.0 atom percent. The L6 test was designed so that fuel would fail into a voided coolant channel near the time of peak power in a transient in which peak power would be about 10 times nominal. The L7 test had a similar design except that the peak power was to be about 20 times nominal. Both tests achieved their respective objectives.

A description of the tests is given in Ref. QCS760.178A3-7. For the present discussion, the most important instrument is the 1.2-meter fast neutron hodoscope. This device counts collimated fast neutrons produced by fissions in the test fuel to form an image of the fuel. As fuel moves about, the count rate of fast neutrons increases in regions where the fuel density

Table QCS760.178A3-1

TREAT EXPERIMENTS SIMULATING LOSS-OF-FLOW ACCIDENT CONDITIONS

Test Designation	Number of Elements	Fissile Fuel Length, mm	Preirradiation Neutron Spectrum	Hodoscope Collimator Viewing Height m	Peak Transient Power ÷ Nominal Power[a]
L2	7	340	None	0.5	1
L3	7	340	Fast	0.5	1
L4	7	340	Fast	0.5	1
L5	3	864	Thermal	0.5	6
L6	3	864	Thermal	1.2	10
L7	3	864	Thermal	1.2	20
R3	1	914	None	0.5	1
R4-R6	7	914	None	0.5	1
R7	7	914	None	0.5	15
R8	7	914	None	1.2	1
F1	1	340	Fast	0.5	1
F2	1	340	Fast	0.5	12

[a]Ignoring preheat power phase, if any.

increases and diminishes in regions where the density decreases thus enabling the hodoscope to form a dynamic image of the fuel relocation.

FRAS3 Calculations

FRAS3 is the current developmental version of the FRAS code which has been used at Argonne for more than eight years to model transient fission gas behavior in mixed oxide fuels. The FRAS3 code models transient fission gas release as a two-step process. In the first step, gas within the fuel grains is released to the grain boundary. In the second step, gas on the grain boundary is released to the grain edge porosity. Currently, gas that reaches the grain edges is assumed to be released. There is likely to be some time delay between the release of gas to the grain edges and its ultimate release from the fuel; however, it is difficult to quantify this delay since some of the relevant parameters such as the magnitude of the fuel porosity and the permeability are not well known and may actually change during the course of the transient. Neglect of the gas in the grain edge porosity is conservative as far as the whole-core calculations are concerned since a potential contributor to fuel dispersal is not taken into account.

To validate the modeling in the FRAS3 code, predictions of gas release based on FRAS3 calculations have been compared with measured gas releases in a series of FGR tests (Refs. QCS760.178A3-2, -3). In the comparisons, the calculated temperature at a radius of 0.9 times the fuel rod radius was assumed to represent the average temperature of the unrestructured fuel. The FRAS3 calculations actually represent a local release fraction while the measurements represent a release fraction based on the total release from the fuel. A summary of the comparisons is shown in Fig. QCS760.178A3-1, where the solid lines show the measured releases and the dashed lines show the envelope of the FRAS3 calculations for the various test conditions. As a result of these comparisons it was concluded that taking into account the differences that would be expected between a total and local release fraction, and "given the uncertainty in the reported FGR fuel temperatures, FRAS3 can correctly predict the magnitude of the total gas release" (Ref. QCS760.178A3-2).

FRAS3 predictions of the fraction of the initial fission gas concentrations retained near the time of fuel motion initiation for both the L6 and L7 tests and for channel 6 in the EOC-4 SAS3D reactor model are shown in Table QCS760.178A3-2. The initial concentrations are based on SAS3D calculations. The thermal histories used in the calculations for the L6 and L7 tests are based on SAS3D calculations of these tests, and the thermal history used for channel 6 is based on the previous EOC-4 LOF best estimate analysis. Use of these results in the SAS3D analyses will be described later in this report.

Analysis of the L6 and L7 TREAT Tests

The general approach to the SAS3D analyses of the L6 and L7 experiments is as follows: First, a steady-state calculation was devised to simulate the irradiation history of the fuel elements used in the tests. Following this, a 20-second transient was computed in which the reactor power level, coolant flow rate, and fuel temperatures were brought to the values that prevailed at the beginning of the tests. Finally, the test transient itself was simulated. This procedure was followed not only for each test, but also for the heat balance transients that were conducted prior to each test.

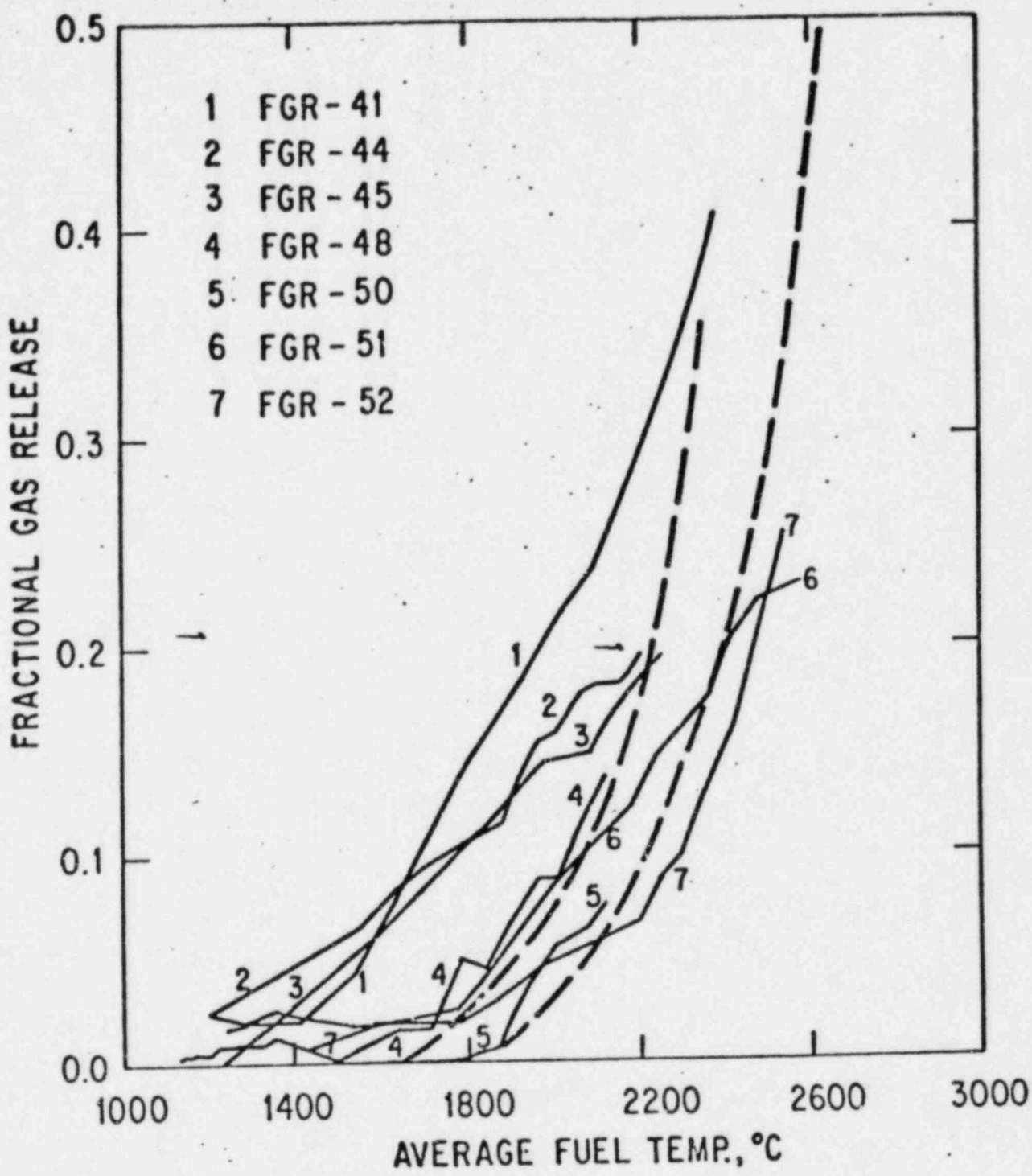

Fig. QCS760.178A3-1 Comparison of Measured (Solid Curves) and Calculated Gas Release Fractions. The Dashed Curves Represent the Envelope of FRAS3 Calculations for the Range of Initial Conditions Corresponding to the Measured Data.

Table QCS760.178A3-2

GAS RETENTION CALCULATED WITH THE FRAS3 CODE NEAR THE TIME OF FUEL DISRUPTION IN TREAT TESTS L6 AND L7 AND FOR CHANNEL 6 IN THE EOC-4 SAS3D CRBR MODEL

Case	Initial Concentration in Unrestructured Fuel, atoms/cc	Percent Retained in Grains	Percent Retained on Grain Boundaries
L6	1.00×10^{20}	24	9.5
L7	1.00×10^{20}	64	4.7
Ch. 6	1.34×10^{20}	54	4.7

Table QCS760.178A3-3

COMPARISON OF MEASURED AND CALCULATED BOILING TIMES FOR THE L6 AND L7 TREAT TESTS

Test	Measured	SAS3D
L6	12.6 s	12.1 s
L7	13.4 s	13.4 s

The single-channel representation of the fuel elements and their associated coolant channels is the same as used in the initial SAS3D analysis of the L7 test (Ref. QCS760.178A3-8). However, in the present work, the sodium loop is modeled using the PRIMAR-0 option of the SAS3D code. The pump coastdown is modeled by specifying the coolant inlet pressure as a function of time. The inertial effects of sodium in the test vehicle loop outside the section where the fuel elements were located are modeled by adding 59 centimeters to the effective coolant column inertial length at the channel inlet. Other input assumptions relating to fuel and cladding properties and heat transfer from fuel to cladding and from cladding to coolant are made as nearly like those that would be used in whole-core analyses as feasible. One measure of how well the heat transfer is modeled is provided by comparing calculated boiling times with the apparent boiling time as indicated by test instrumentation. Table QCS760.178A3-3 shows this comparison for the L6 and L7 tests. The calculations utilized a superheat of 10°C for initial bubble formation. The close agreement in the case of L7 is probably fortuitious while better agreement with the L6 result would be desirable. Nevertheless, the comparison is considered satisfactory.

Input for the SAS3D fuel motion model SLUMPY was prepared as follows. Fission gas parameters were evaluated on the basis of the FRAS3 calculations described previously. One of the SLUMPY parameters is the fraction of the initial gas concentration that is present when fuel motion begins. Since the FRAS3 calculations assumed the initial concentration that is computed internally by the SAS3D steady-state calculation, this fraction was set to 0.34 for the L6 test and 0.69 for the L7 test (see Table QCS760.178A3-2). A second parameter specifies the fraction of the gas present at the time of fuel motion initiation that is to be made immediately available. The immediately available gas was assumed to be given by the FRAS3-calculated gas concentrations on the grain boundaries. This fraction was set to 0.28 and 0.07 respectively for L6 and L7. That gas which is not immediately available was released from molten fuel with a time constant of 100 ms and from solid fuel with a time constant of 3 s; these are nominally employed SAS3D values.

Most of the other SLUMPY input parameters were set to default values or to values that had been used in previous homogeneous studies (Ref. QCS760.178A3-9). The number of grams of stainless steel per gram of fuel was set to a small value (0.001) because such a value was needed in the whole core calculations to prevent the flow area available to the SLUMPY compressible zone from becoming excessively large as disrupted fuel was pushed up the coolant channel. Steel vapor, however, was not considered as a potential source for fuel dispersal in either the test analyses or in the whole-core calculations.

To achieve what was regarded as a reasonable match between the SAS3D/SLUMPY calculations and the test data, attention was focused primarily on three parameters. The first of these was the fraction of the gravitational constant used in the equations of motion, the second was a parameter called QSODUM which establishes coupling between the SLUMPY calculation and the coolant dynamics calculation, and the third was the parameter VISFU which permits the viscosity in the compressible zone calculation to be increased when significant amounts of unmelted fuel are present.

Of primary interest in the present analysis is the comparison between the fuel motion as calculated by SAS3D/SLUMPY and that measured in the TREAT tests. A convenient figure of merit to use for this purpose is the reactivity feedback that would be obtained if the observed fuel motion were to occur in an operating LMFBR (Ref. QCS760.178A3-10). Designating this quantity as the relative fuel worth (REF), it is obtained by weighting the computed or measured fuel density changes with a normalized (in this case the homogeneous CRBRP) axial fuel worth distribution and spatially integrating. REF is normalized so that its value is initially zero and is -1.0 if all the fuel is removed. The criterion for choosing values for the SAS3D/SLUMPY parameters was that the slope of the REF obtained from the calculations should be reasonably close to the slope of the experimental REF.

The parameter values which fit L6 and L7 best are 0.2 for the fraction of the gravitational constant, 0.02 for QSODUM, and 10,000 for VISFU. A 50% fuel melt fraction was used as the criterion for initiating the fuel motion calculation. Calculated and experimental REF's obtained using these parameters are plotted as a function of the TREAT reactor energy in Figs. QCS760.178A3-2 and -3. The experimental data were grouped into time bins such that the reactor energy production within each bin was constant. As a result, each of the experimental points has the same statistical significance. The calculated and experimental REF's are plotted in Figs. QCS760.178A3-4 and -5 as a function of time after 14.1 s. The choice of 14.1 s as the origin in these plots was made because this is about the time when thermal hydraulic instrumentation indicated that fuel disruption might have occurred in the L7 test. The 50% melt fraction criterion was reached in the SAS3D calculations at 14.335 s and 14.161 s respectively for the L6 and L7 tests. The agreement between calculation and experiment shown in the figures is regarded as satisfactory and is believed to justify the use of the chosen SLUMPY parameters (other than the fission gas fraction) for the modeling of irradiated fuel motion in whole core calculations. Some discussion of sensitivities observed in the test calculations are given later in this report.

Whole-Core Calculations for CRBR EOC-4 LOF

The SAS3D whole-core calculation for the heterogeneous EOC-4 core which is most relevant to the issue addressed herein is summarized below. Input data for this case was essentially the same as was used in the best estimate analysis (Ref. QCS760.178A3-1, Section 7.2.1) except for the following changes. First, all driver fuel channels were set to initiate fuel motion when the fuel melt fraction reaches 50%. Second, integer input variables were set to permit sodium film motion calculations to continue rather than terminate after two seconds of boiling, to also allow slip between fuel particles and fission gas in the lead channel, and to ignore stainless steel vapor pressures in the event of mixing of steel and fuel during the SLUMPY calculation. Third, except for the two variables which specify the amount of fission gas that is present when the fuel motion calculation begins, input variables for SLUMPY were set to the values which were found to provide the best fit for the L6 and L7 tests.

In channel 6, the fraction of the steady-state fission gas concentration assumed to be present when the fuel motion calculation started was set to 0.59, and the fraction of gas present that was made immediately available was set to 0.08. These values are based on the FRAS3 calculations described

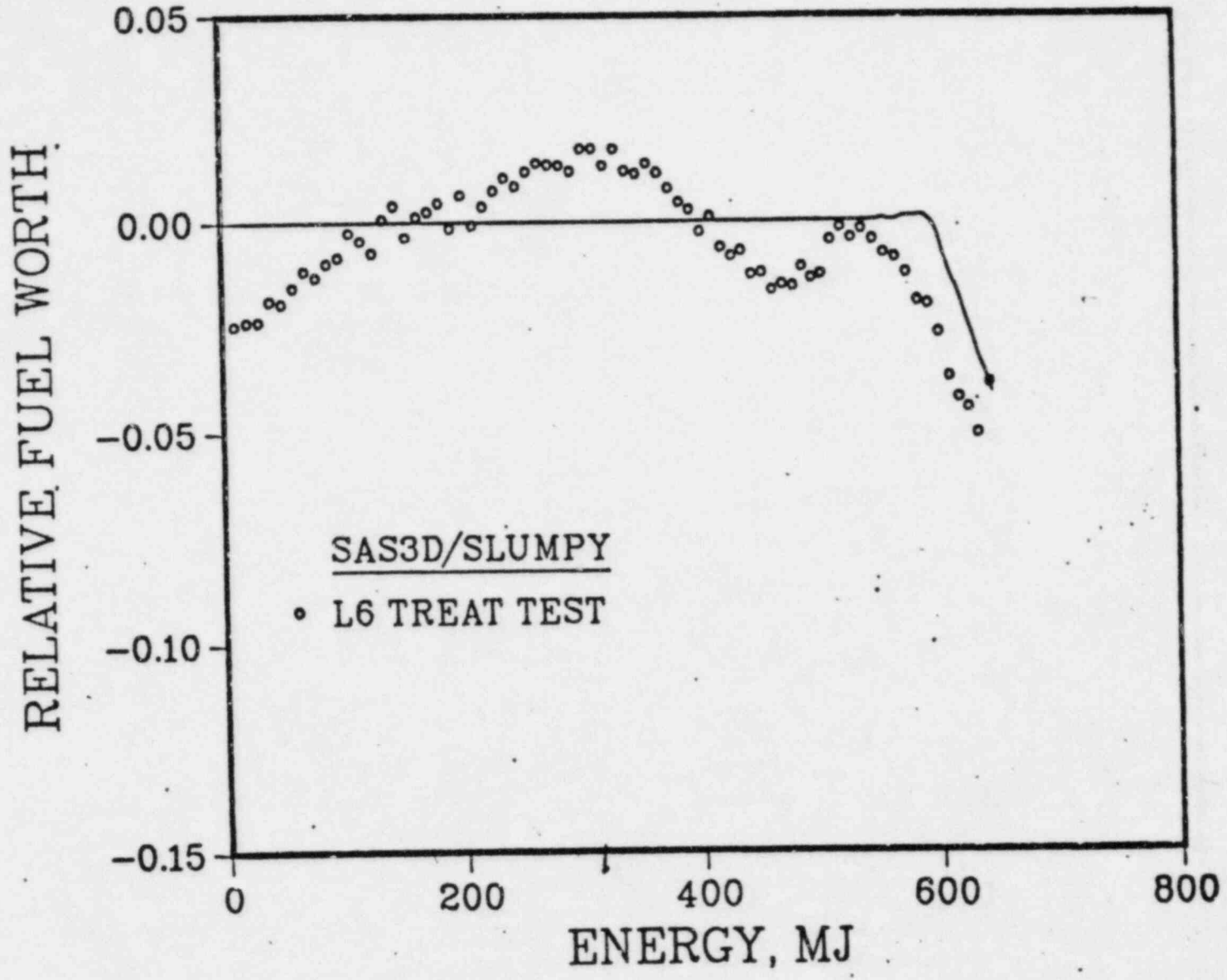

QCS760.178A3-9

Fig. QCS760.178A3-2 Comparison of Measured and Calculated Relative Fuel Worths as a Function of Reactor Energy for the L6 TREAT Test.

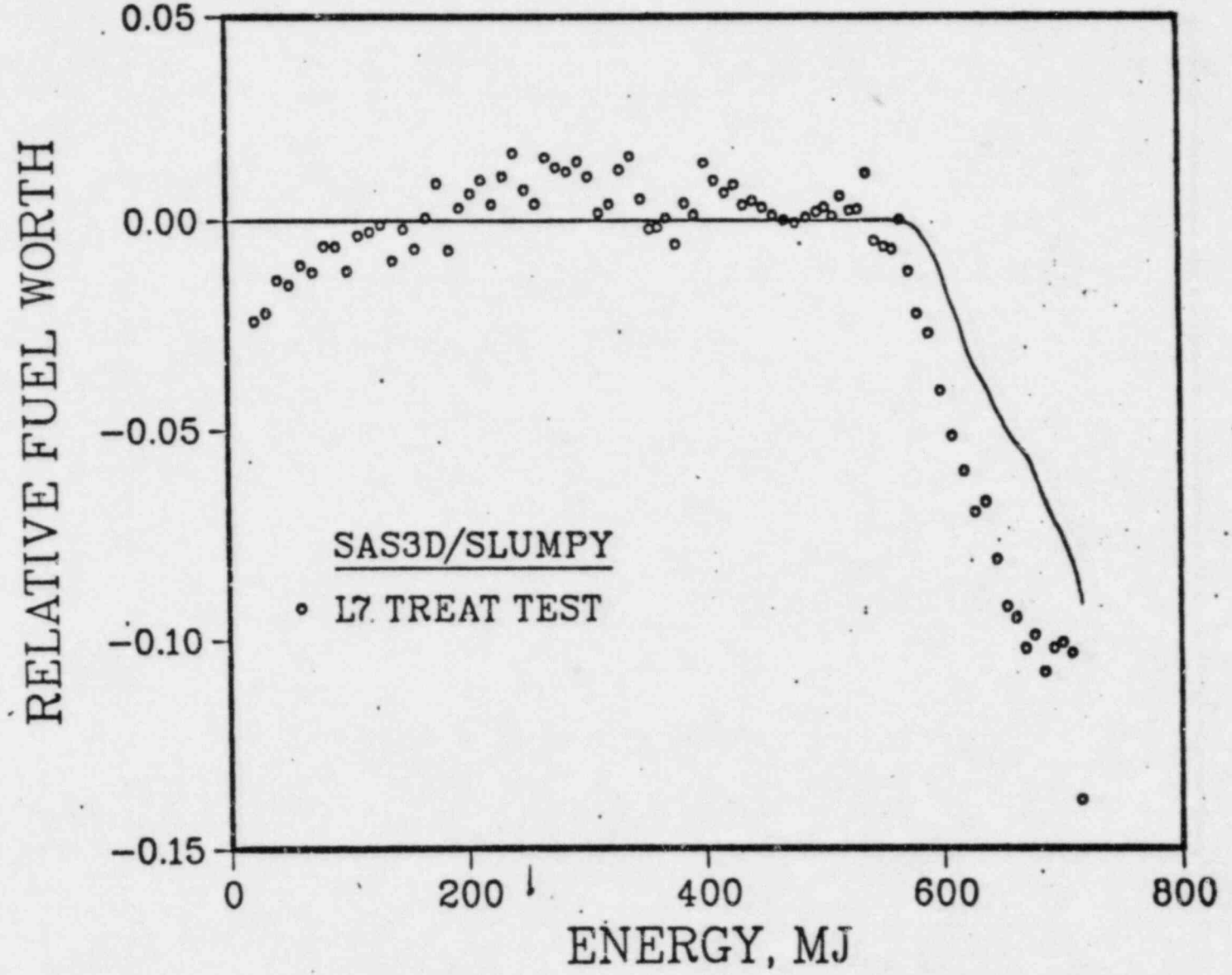

QCS760.178A3-10

Fig. QCS760.178A3-3 Comparison of Measured and Calculated Relative Fuel Worths as a Function of Reactor Energy for the L7 TREAT Test.

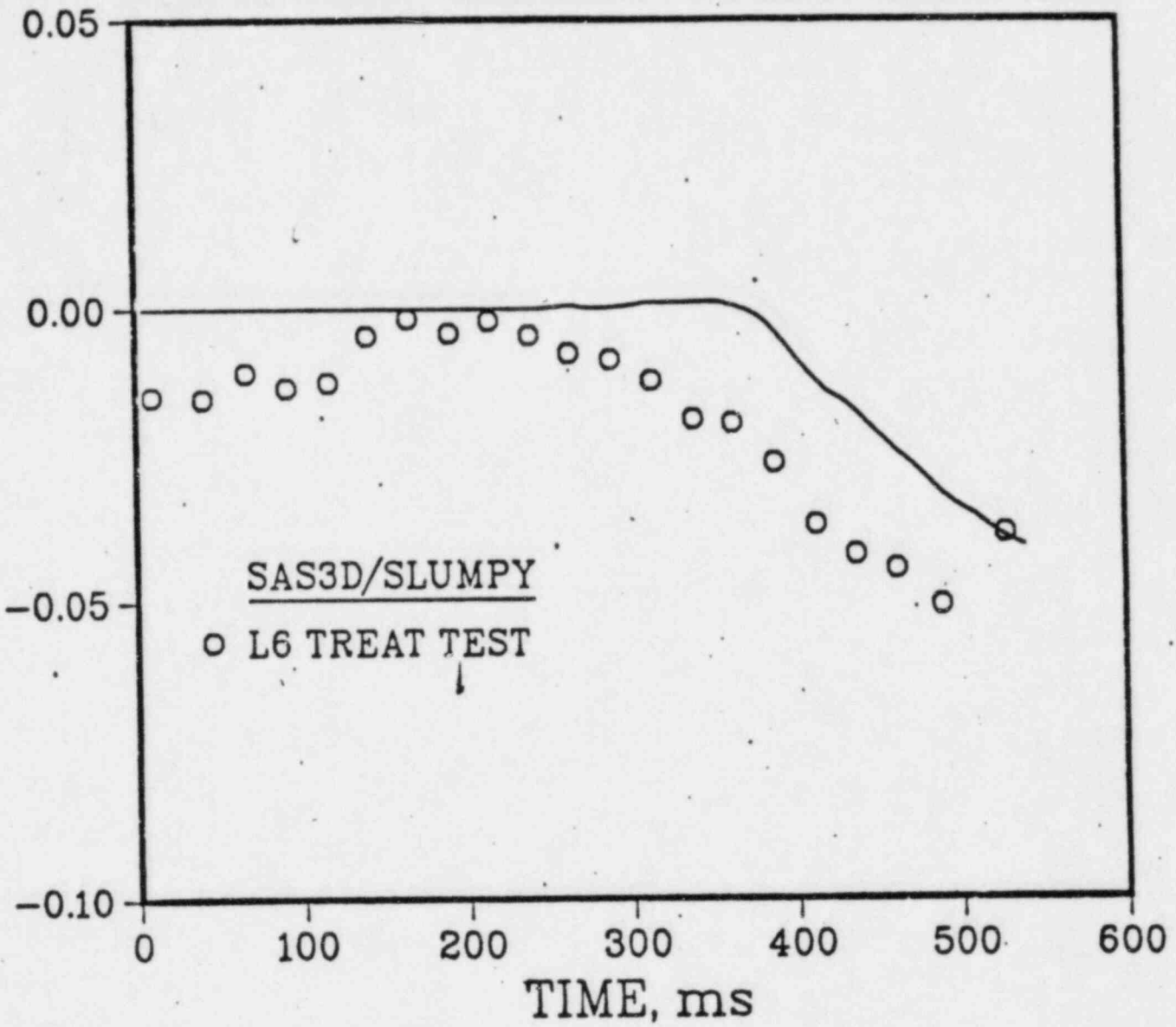

Fig. QCS760.178A3-4 Comparison of Measured and Calculated Relative Fuel Worths as a Function of Time After 14.1 s for the L6 TREAT Test.

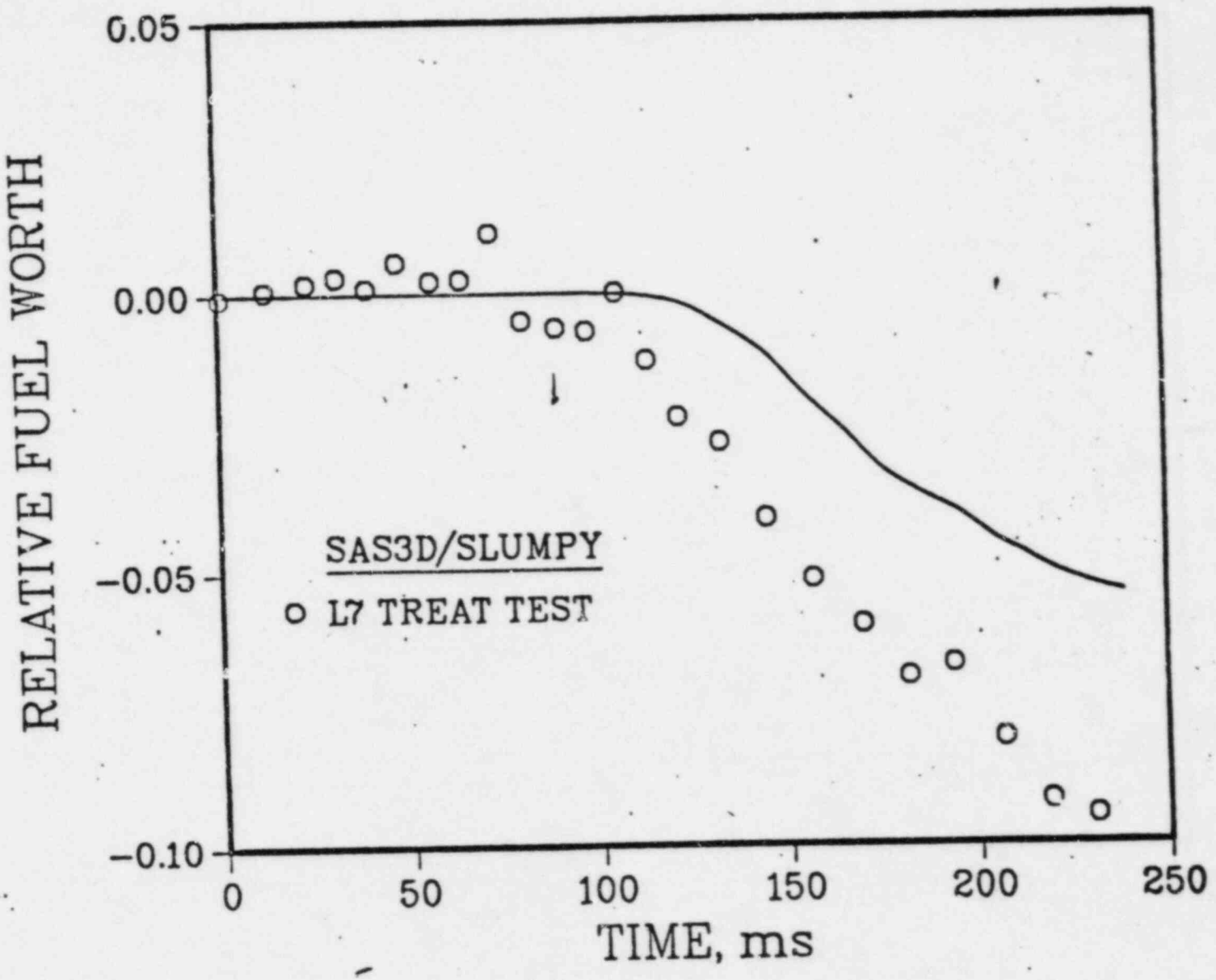

QCS760.178A3-12

Fig. QCS760.178A3-5 Comparison of Measured and Calculated Relative Fuel Worths as a Function of Time After 14.1 s for the L7 TREAT Test.

earlier. FRAS3 calculations were not performed for the other driver fuel channels, so these same fractions were used for these channels as well. Since the remaining channels have higher burnup than channel 6, it is not clear that use of these fractions is conservative, but these channels are of secondary importance for this case.

An event sequence is shown in Table QCS760.178A3-4. The portion of the transient prior to fuel motion in channel 6 is very similar to that in the earlier CRBRP calculation although the fact that the film motion calculation was allowed to continue in all boiling channels did cause some minor changes in the power level and in the coolant voiding reactivity. Following the initiation of fuel motion in channel 6, the scenario changes. Fuel motion reactivity feedback remains positive in channel 6 for about 146 ms following fuel disruption and the power level continues to rise throughout most of this period reaching a peak of about 4.7 times nominal. Then the fuel motion reactivity becomes more negative and finally drives the reactor subcritical about 406 ms after first fuel motion.

While it is felt that SLUMPY can be calibrated to adequately model fuel motion during the initial disruption, the fact that fuel freezing and plugging is not modeled makes it questionable to continue using the model for much more than a few hundred milliseconds after initial fuel motion. The SAS3D calculation might be terminated at this point. However, to better understand the whole core conditions and, in the belief that negative fuel motion reactivity would continue somewhat beyond the time when SLUMPY encountered time step difficulties, the calculation in channel 6 was stopped and the SAS3D calculation continued. The time when this occurred along with the power level and various reactivity feedbacks is indicated in Table QCS760.178A3-4. Beyond the time indicated, no fuel motion occurred in channel 6, although the fuel was allowed to continue to absorb heat and to transfer heat to its surroundings.

Following termination of the fuel motion calculation in channel 6, the reactor remained subcritical for about 323 ms, and then reached criticality on the strength of coolant voiding and cladding motion. The reactivity remained above critical for about 163 ms during which time the peak reactivity was about 16 cents and the peak power was about 1.8 times nominal. The reactor became subcritical again because of a decline in both the clad motion reactivity and the coolant reactivity. This time the reactor remained subcritical for about 144 ms and then became recritical because of an increase in both the coolant and clad motion reactivities. The reactivity continued to climb until it reached about 26 cents at which time fuel motion was initiated in channel 2. Following fuel disruption in channel 2 the reactivity increased still further partly because of positive fuel motion feedback. Both the power and the reactivity passed through local maxima about the time when fuel motion was initiated in channel 4. About 380 ms after fuel motion started in channel 2, the reactor became subcritical again because of negative fuel motion feedback from channel 2. Reactivity feedbacks from channels 4 and 7 were positive at the end of the calculation and totaled about 28 cents.

To assess the plenum gas release effects on upward steel relocation and the potential for compaction of fuel by the gas remaining in the fission gas plena, it was first estimated that release of this gas could not start until the cladding on the top node of fuel reached a temperature of 1400°C; approximately the melt point. The time between the achievement of this criterion and

Table QCS760.178A3-4

EVENT SEQUENCE FOR EOC-4 LOF SCENARIO

Time	Event	CHN	P/PO	RHO	RHOD	RHOE	RHOV	RHOF	RHOC
12.7655	Coolant Boiling	6	0.821	-0.094	-0.140	-0.050	0.096	0.0	0.0
14.6697	Coolant Boiling	2	0.819	-0.068	-0.156	-0.057	0.145	0.0	0.0
15.0561	Coolant Boiling	4	0.817	-0.069	-0.161	-0.061	0.152	0.0	0.0
15.7772	Coolant Boiling	7	0.851	-0.019	-0.170	-0.068	0.219	0.0	0.0
17.1048	Coolant Boiling	10	1.226	0.234	-0.235	-0.125	0.594	0.0	0.0
17.1998	Coolant Boiling	11	1.269	0.253	-0.242	-0.132	0.627	0.0	0.0
17.5298	Coolant Boiling	9	1.321	0.252	-0.270	-0.159	0.681	0.0	0.0
17.7792	Coolant Boiling	13	1.241	0.190	-0.287	-0.175	0.653	0.0	0.0
17.9242	Clad Motion	6	1.320	0.233	-0.297	-0.186	0.715	0.0	0.0
18.2117	Coolant Boiling	12	2.225	0.514	-0.333	-0.223	0.999	0.0	0.071
18.6442	Coolant Boiling	15	2.570	0.531	-0.397	-0.279	1.130	0.0	0.076
18.8732	Coolant Boiling	14	3.002	0.561	-0.440	-0.315	1.241	0.0	0.075
19.1867	Clad Motion	2	2.889	0.498	-0.495	-0.366	1.282	0.0	0.076
19.3417	Clad Motion	4	3.770	0.594	-0.527	-0.390	1.238	0.0	0.273
19.3617	Fuel Motion	6	3.784	0.590	-0.532	-0.393	1.233	0.0	0.283
19.4129	Coolant Boiling	5	3.695	0.570	-0.544	-0.400	1.200	0.005	0.308
19.4930	Peak Reactivity	0	4.654	0.644	-0.563	-0.411	1.207	0.003	0.408
19.5017	Peak Power	0	4.670	0.643	-0.566	-0.413	1.201	0.002	0.419
19.6092	Clad Motion	7	3.453	0.492	-0.587	-0.426	1.186	-0.110	0.428
19.6163	Coolant Boiling	3	3.437	0.488	-0.588	-0.427	1.186	-0.123	0.441
19.7705	Coolant Boiling	1	1.744	-0.022	-0.594	-0.434	1.145	-0.701	0.560
19.7730	Coolant Boiling	8	1.722	-0.036	-0.594	-0.434	1.145	-0.712	0.559
20.0267	Fuel Motion Off	6	1.049	-0.600	-0.577	-0.433	1.440	-1.523	0.493
20.1267	Clad Motion	10	0.984	-0.651	-0.579	-0.432	1.365	-1.523	0.518
20.1555	Clad Motion	11	1.004	-0.601	-0.578	-0.432	1.389	-1.523	0.543
20.5080	Clad Motion	9	1.514	0.007	-0.588	-0.433	1.565	-1.523	0.987
20.7005	Clad Motion	13	1.506	0.019	-0.597	-.0433	1.586	-1.523	0.986
20.9430	Fuel Motion	2	1.989	0.259	-0.610	-0.431	1.731	-1.523	1.092
21.1105	Fuel Motion	4	2.863	0.470	-0.629	-0.428	1.773	-1.402	1.157
21.1342	Clad Motion	12	2.665	0.425	-0.631	-0.428	1.760	-1.399	1.123
21.5380	Fuel Motion	7	0.681	-1.324	-0.638	-0.425	1.848	-3.711	1.602
21.8117	Clad Motion	15	0.363	-3.377	-0.634	-0.426	1.864	-5.636	1.456
21.8830	Termination	0	0.334	-3.742	-0.633	-0.426	1.837	-5.904	1.385

Nomenclature is as follows:

CHN - SAS channel #.

P/PO - Core power relative to nominal.

RHO - Net reactivity in $.

RHO(X) - Reactivity in $ due to Doppler (D), axial expansion (E), sodium void (V), fuel motion (F), cladding motion (C).

the start of clad motion or fuel motion is listed in Table QCS760.178A3-5. Also listed in the table is the approximate gas pressure when the release would start. In those channels where either clad motion or fuel motion or both had not initiated in a channel, the time listed is the time to the end of the calculation. An analysis of the conditions at the time the release should start indicates that the time constant for the release should be about 250 ms. A test calculation for channel 6 using the SAS3D gas release model agreed rather well with this time constant estimate; however, a similar test calculation for channel 9, which had a much higher pressure than in channel 6 indicated that for the higher pressure channels the time constant is somewhat less than 250 ms.

From Table QCS760.178A3-5 it is seen that only two time constants exist for plenum gas release prior to cladding motion for most of the channels. The plenum pressure will be about 4 atm with a continued release (note that this is higher than the sodium inlet plenum pressure) occurring while molten steel is available to move. The gas release would have stopped the sodium vapor flow and an upper cladding blockage would not be anticipated. Instead, a thick lower blockage would form by steel drainage.

Table QCS760.178A3-6 lists the fuel thermal condition in those channels where fuel motion did not occur at the time when the calculation was terminated. The results listed in Tables QCS760.178A3-5 and -6 provide the basis for the conclusion stated at the beginning of this report that the potential for fuel compaction driven by the gas pressures in the fission gas plena is very low. The results in Table QCS760.178A3-5 show that for those channels where fuel motion occurred during the calculation, there is ample time for the pressures in the plena to be relieved prior to fuel motion. Given that the reactor is appreciably subcritical at the end of the calculation, and given the condition of the fuel in those channels that have not yet experienced fuel motion, it seems likely that pressure will be relieved in the plena of those channels long before any fuel motion might start.

Sensitivities and Uncertainties

With respect to the experiment analysis, one of the major uncertainties is determining precisely when a given SAS3D-calculated thermal condition (e.g. a 50% fuel melt fraction) actually occurred in the experiment. It was because of this that no attempt was made to try to get the calculated REF to fall directly on the experimental REF for the time interval during which fuel dispersal seemed to be clearly indicated. The systematic trends and scatter in the experimental data also suggested that such an attempt should not be made. In the experiment calculations, the timing of specific thermal events was found to be sensitive, among other things, to the value of the heat transfer coefficient between fuel and cladding, and to the power coupling factor between the TREAT reactor and the fuel in the test vehicle. This latter factor is estimated to have a total uncertainty of ± 10%.

Among the SLUMPY parameters focused on the analyses of the L6 and L7 experiments, it was found that calculations for both tests showed moderate sensitivity to the value chosen for QSODUM. While there did appear to be a preference for a small, non-zero value, the value zero could have been chosen without too much harm to the comparison between calculated and experimental REF's. Calculations for the L6 test were rather strongly sensitive to the

Table QCS760.178A3-5

APPROXIMATE TIMES TO CLADDING AND FUEL MOTION RELATIVE TO CLAD FAILURE AND PLENUM-FISSION-GAS PRESSURES AT FAILURE (1400°C) OF THE TOP FUEL NODE IN DRIVER ASSEMBLIES AS DETERMINED FROM THE SAS3D CALCULATION

Channel	Time to Clad Motion, s	Time to Fuel Motion, s	Pressure at Failure atm
2	0.60	2.36	42
4	0.61	2.38	42
6	1.14	2.58	22
7	0.58	2.51	44
9	0.59	1.96*	39
10	0.55	2.31*	41
11	0.66	2.39*	42
12	0.79	1.54*	34
13	0.70	1.89*	36
14	0.66*	0.66*	26
15	0.79	0.86*	27

*These are times referred to the end of the calculation since the event in question did not occur.

Table QCS760.178A3-6

FUEL CONDITIONS IN THOSE CHANNELS THAT HAVE NOT INITIATED

FUEL MOTION BY THE TERMINATION OF THE CALCULATION

Channel	Peak Fuel Melt Fraction or Temperature
9	0.26
10	0.32
11	0.30
12	0.10
13	0.15
14	2656°C
15	0.003

value chosen for the fraction of the gravitational constant, while the calculations for both tests were rather strongly sensitive to the value chosen for the parameter VISFU.

The key to the conclusions reached on the basis of the whole-core analysis is the fuel modeling that was used for channel 6. While the analysis of the L6 and L7 TREAT tests appear to provide strong justification for the modeling used, the most important point seems to be that the fuel in channel 6 was allowed to disperse. A preliminary calculation in the investigation used a value of unity for the fraction of the gravitational constant, values of zero for QSODUM and VISFU, and approximately the same amount of fission gas immediately available. Because of the larger fraction of the gravitational constant, the reactor power reached about 7 times nominal power before fuel motion reactivity feedback from channel 6 began to decrease. SLUMPY was allowed to continue computing fuel motion throughout this case and as a result, late in the transient, partly aided by a rather large decrease in the magnitude of the negative reactivity feedback from channel 6, the reactor became recritical with the reactivity reaching nearly 96 cents. This produced a power burst in which the reactor power reached 42 times nominal. In spite of the differences between this result and the present case, the general conclusions regarding the potential for compaction of fuel by plenum fission gas were very much the same as described in this report.

Termination of the fuel motion calculation in channel 6 introduces some degree of uncertainty into the later portion of the transient. If the fuel motion had been stopped earlier, the negative fuel motion reactivity would have been smaller in magnitude and the reactor would have been less subcritical. The transient would then be changed from about 20.02 s onward. However, the amount of negative fuel motion reactivity computed up to the time of fuel motion cutoff in channel 6 does not appear to be excessive. It is primarily due to the movement of fuel away from the midplane of the reactor core; the total amount of fuel located in the axial blanket at the time of fuel motion cutoff was less than 5 grams per fuel pin. If all this fuel were moved back into the first two nodes in the active core the net reactivity increase would be less than 10 cents and the reactor would still be more than 50 cents subcritical. The time margins between clad failure and fuel motion shown in Table QCS760.178A3-5 appear to be large enough so that this reactivity change would have a negligible effect on conclusions reached herein.

Conclusion

The analyses of the whole core response to loss-of-flow (LOF) without scram event have been conducted using methods and a data base which are consistent with the most relevant experimental information. By detailed examination of TREAT LOF experiments L6 and L7 with the SAS3D code and of fission gas release experiments with the FRAS3 code, a technically defensible set of modeling parameters for fuel disruption and dispersal have been identified. When such modeling is utilized in the whole core analysis of the EOC-4 LOF scenario, it has been found that early and significant fuel dispersal takes place and the possibility of autocatalytic behavior leading to energetic hydrodynamic disassembly is highly unlikely. In particular, the mechanism for fuel column compaction by plenum fission gas is generally eliminated by the significant time delay between the initiation of plenum depressurization and fuel rod disruption. This results from the relatively

mild power excursion experienced when experimentally consistent fuel dispersal parameters are used. The sensitivity of the whole core response to fuel motion modeling is relatively weak and, although specific power histories may differ, the general conclusion that plenum fission gas compaction is not a significant concern can be made as long as experimentally consistent fuel motion assumptions are made.

References

QCS760.178A3-1 S. K. Rhow, et.al., "An Assessment of HCDA Energetics in the CRBRP Heterogeneous Reactor Core," CRBRP-GEFR-00523 (December 1981).

QCS760.178A3-2 T. E. Kraft, "An Evaluation of Recent Transient Fuel Behavior Models Based on Selected Experimental Results," ANL/RAS 80-29 (November 1980).

QCS760.178A3-3 J. M. Kramer, e .al., "An Analysis of Recent Fuel Disruption Experiments," Intl. Top. Mtg. on LMFBR Safety, Lyon, France (July 1982).

QCS760.178A3-4 E. E. Gruber and E. H. Randklev, "Comparison of Fission Gas Effects in a Transient Overpower Test (HUT 5-7A) to FRAS3 Code Predictions," Intl. Top. Mtg. on Fast Reactor Safety Technology, Seattle, Washington (August 1979).

QCS760.178A3-5 R. Simms, et.al., "TREAT Experimental Data Base Regarding Fuel Dispersals in LMFBR Loss-of-Flow Accidents," Proc. of Top. Mtg. on the Reactor Safety Aspects of Fuel Behavior, Sun Valley, Idaho (August 1981).

QCS760.178A3-6 A. DeVolpi, et.al., "Fast-Neutron Hodoscope at TREAT: Data Processing, Analysis, and Results," Nucl. Tech., Vol. 30, 398 (1976).

QCS760.178A3-7 R. Simms, et.al., "Loss-of-Flow TREAT Tests L6 and L7 with Irradiated LMFBR-Type Fuel, "Nucl. Tech., Vol. 52, 331 (March 1981).

QCS760.178A3-8 C. H. Bowers, et.al., "Analysis of TREAT Tests L7 and L8 with SAS3D, LEVITATE, and PLUTO-2," Specialists' Workshop on Predictive Analysis of Material Dynamics in LMFBR Safety Experiments, LA-7938-C, Los Alamos Scientific Laboratory (March 13-15, 1979).

QCS760.178A3-9 W. R. Bohl, et.al., "An Analysis of the Unprotected Loss-of-Flow Accident in the Clinch River Breeder Reactor with an End-of-Cycle Core," ANL/RAS 77-15 (May 1977).

QCS760.178A3-10 R. Simms, "An Evaluation of Fuel Motion in Recent TREAT Experiments with Liquid-Metal Fast Breeder Reactor Fuel," Nucl. Tech., Vol. 50, 257 (October 1980).

Question CS760.178B4

To what extent can steel blockages form throughout the core to prevent fuel removal through normal axial blanket flow channels during the early phase of the LOF? What is the location and character of the steel blockages in these channels?

Response

A significant time interval exists for molten cladding relocation during a loss-of-flow without scram event in the CRBRP. This is true for the entire core burnup cycle (i.e., BOC through EOC) and is principally the result of the very low effective sodium void worth of the heterogeneous design. However, very little upward steel relocation or blockage is expected for the irradiated core condition due to the blowdown of the high pressure plenum fission gas. The gas release opposes the sodium vapor streaming which is the primary mechanism for upward relocation of molten cladding (see response to QCS760.178A-3 for the CRBRP transient analysis). This gas release effect has been experimentally confirmed (Ref. QCS760.178B4-1) and results in only a thick lower steel blockage for irradiated core conditions.

The remaining discussion is therefore primarily focused on the BOC core condition where upper steel blockages are expected to form as shown in Chapter 7 of Ref. QCS760.178B4-2. In response to the first part of the above question, two additional SAS3D calculations were performed for the BOC-1 core to maximize the potential effects on the melt-out phase entrance conditions of the axial location of the blockage as well as uncertainties in core reactivity feedback parameters. The comparative reference for these new calculations is Case 1C, Section 7.1.1 of Ref. QCS760.178B4-1 which presents the best estimate; slow drainage of disrupted fuel comparable to PLUTO-2 calculations.

In order to examine the axial location effect in the first analysis (labeled Case 4) the steel blockage was forced to form upon entering the upper axial blanket, providing the maximum restriction to fuel removal. The core transient response history and extent of steel blockages were found to be quite similar for the reference and modified axial blockage location. Figures QCS760.178B4-1 and -2 depict the core conditions at the onset of fuel motion in each analysis; very little independent steel relocation occurs after this event. Based upon the mechanism of near-fresh fuel melting and drainage, a power burst occurs (comparable to Case 1C) which disperses fuel and leaves the core in a subcritical but higher reactivity state. The peak fuel thermal conditions in the fuel channels which did not disrupt are reasonably similar as shown in Table QCS760.178B4-1. Hence, the CRBRP core dynamic behavior was found to be only weakly affected by the steel blockage axial location. The same extent of steel blockages throughout the core was found to exist upon melt-out phase initiation. In addition to locating the steel blockage at the entrance to the UAB, uncertainties in reactivity parameters were also represented in a manner to slow down the transient response, and thereby allow

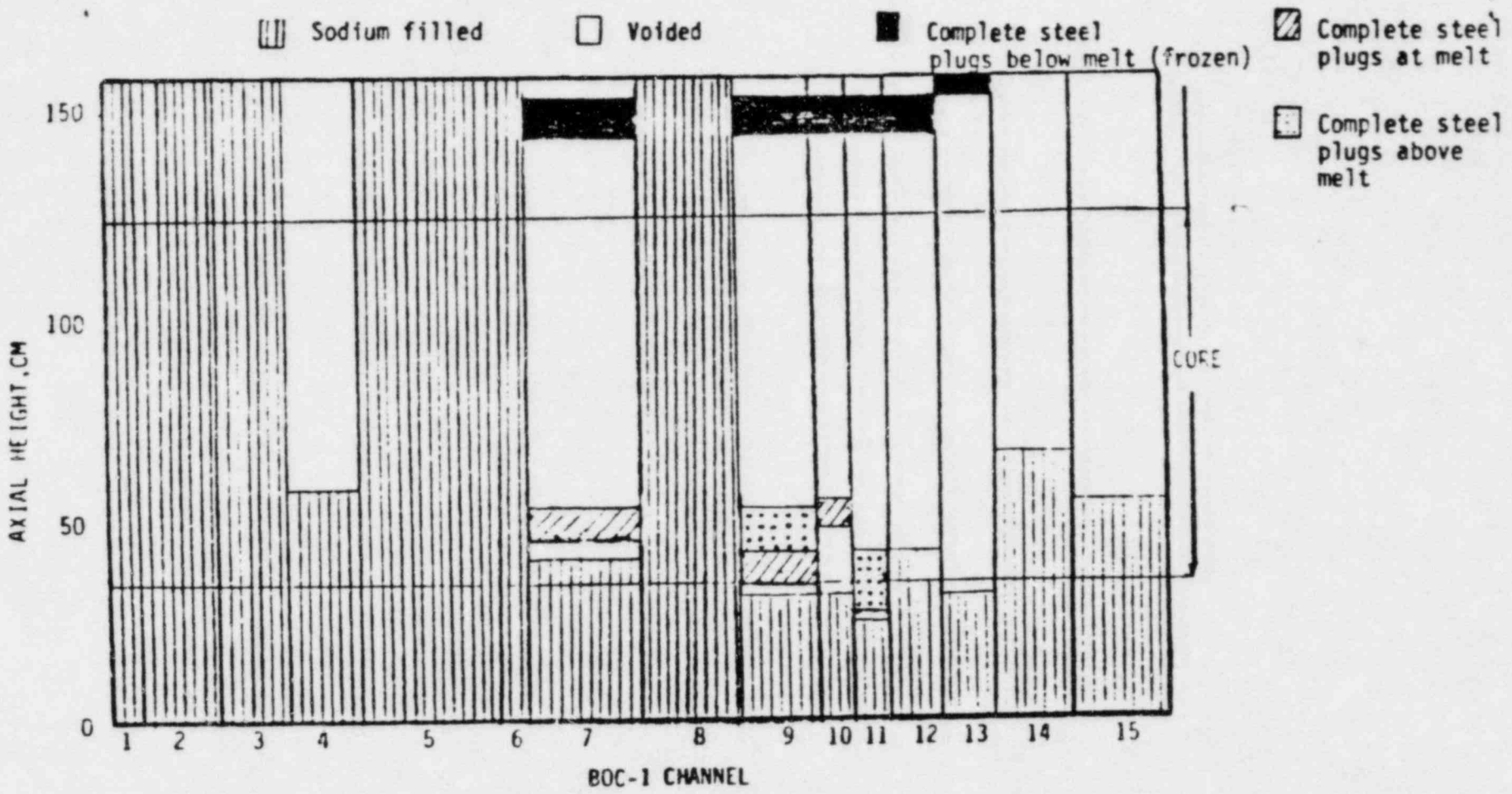

QCS760.178B4-2

Fig. QCS760.178B4-1 State of Core at Initiation of First Fuel Disruption (Ch. 11) for BOC-1 LOF Case 1C (Doppler = -20¢, Axial = -38¢, Sodium Void = -36¢, Cladding = 155¢, Net = 63¢, P = 2.33 Nominal).

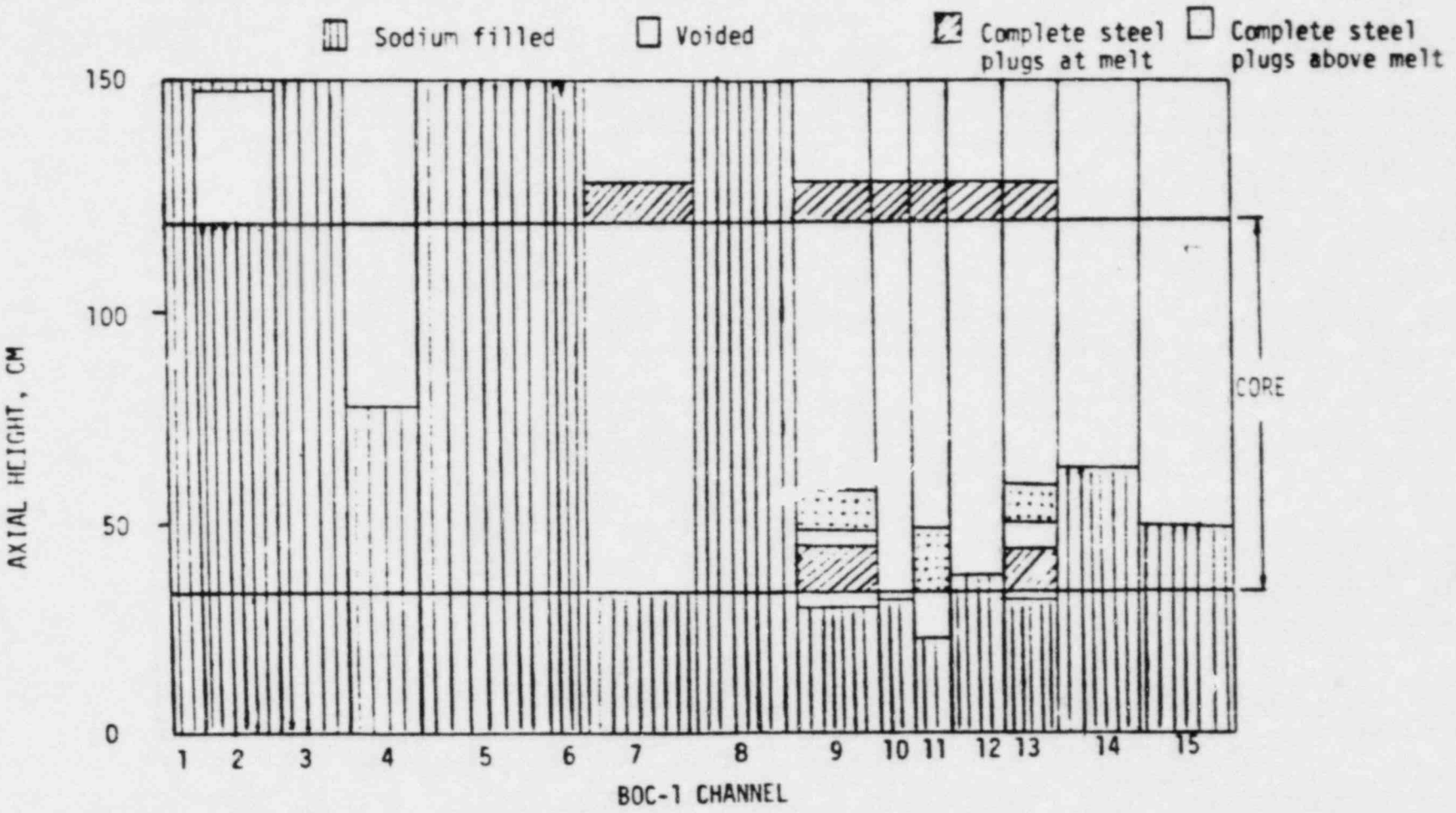

QCS760.178B4-3

Fig. QCS760.178B4-2 State of Core at Initiation of First Fuel Disruption (Ch. 11) for BOC-1 LOF Case 4 (Doppler = -21¢, Axial = -38¢, Sodium Void = -47¢, Cladding = 109¢, Net = 2¢, P = 0.93 Nominal).

Table QCS760.178B4-1

FUEL MELT FRACTION (OR MAXIMUM TEMPERATURE)

AT END OF SAS ANALYSIS FOR BOC-1 LOF

SAS Channel Number	Number of Fuel Assemblies	Fuel Melt Fraction or Maximum Temperature (°C) Case 1C	Case 4	Case 5
2	12	0.04	0.08	2679
4	18	0.24	0.28	0.01
14	18	0.07	0.11	2632
15	24	0.30	0.31	2679
Time from Start of LOF (S)		20.4	19.9	23.1
Normalized Energy (FPS) from Initiation of LOF		20.5	20.5	20.5
Energy Produced During Power Burst (FPS)		3.5	3.5	3.5

additional time for blockage formation. The specific, additional changes made to construct Case 5 (beyond Case 4) were:

1. Local negative sodium voids more negative by 60%*,
2. Local positive sodium voids more negative by 60%*,
3. Doppler constant more negative by 20%,
4. Steel worth uniformly reduced by 20%.

Nominal fuel reactivity worths were used for Case 5 since it was a-priori unclear how to bias them; initial fuel drainage has the effect of adding positive reactivity, while subsequent fuel dispersal results in negative reactivity. The expected slowdown in core response was obtained with initial cladding melting and fuel motion occurring approximately 1 and 2.6 seconds later than in the reference case. The slower developing transient and stronger Doppler feedback act to reduce the peak power attained in the fuel drainage induced power burst to 61 P_o, or about half of the reference case peak value. However, the longer duration of the power burst results in an energy addition comparable to those of the other two calculations. The condition of the core is actually more benign in this case than in the other two as depicted in Fig. QCS760.178B4-3 and Table QCS760.178B4-1. At the onset of fuel disruption, reduced upper steel blockages (Channel 10 blockage is absent) and reduced sodium voiding exist in the core. Concurrently, at the end of the power burst the low power channels contain substantially reduced energy due to the slower, lower power transient and enhanced cooling by diverted sodium flow from the lead channels.

It is concluded that the incorporation of reactivity uncertainties to slow the LOF leads to a more benign transient during the initial part of the LOF. Although the degree of steel blockages is similar to the reference case, there is actually less propensity for upper steel blockages to form in the lower power fuel assemblies of the BOC-1 core during the slower, lower power transient.

Hence, based upon the concept of near fresh fuel drainage upon substantial melting, the maximum extent of steel blockage formation in the UAB is well represented by the best estimate calculations of Ref. QCS760.178B4-1.

In response to the second part of this question, a detailed reassessment of the location and character of the steel blockages was performed. This new examination made use of additional experimental and analytic information which was not included in the understanding represented by Ref. QCS760.178B4-2, see Section 8.2.1. That earlier assessment can be summarized as the following:

a. In the absence of opposing plenum gas release, gross upward steel relocation will occur due to sodium vapor streaming after cladding melting extends fully across the fuel assembly.

---

*These reactivity uncertainties were originally stated as approximately two sigma values. Additional, recent information provided in response to QCS760.178A-2 on sodium void worth indicates these values to be substantially more conservative.

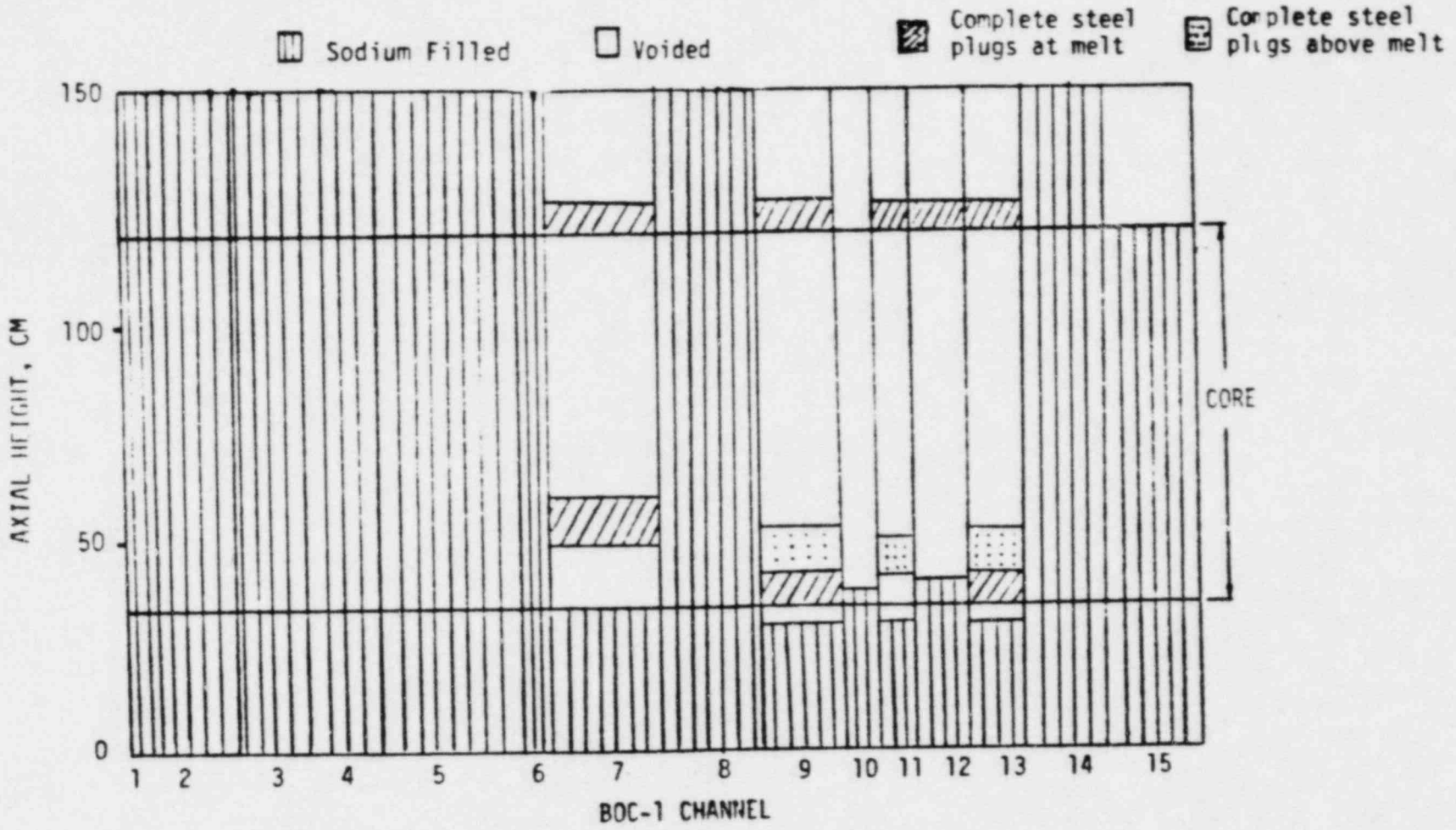

QCS760.178B4-6

Fig. QCS760.178B4-3 State of Core at Initiation of First Fuel Disruption (Ch. 11) for BOC-1 LOF Case 5 (Doppler = -10¢, Axial = -10¢, Sodium Void = -70¢, Cladding = 90¢, Net = -0.3¢, P = 0.70 Nominal).

b. The steel blockages which start to form upon entry to the UAB, are thin (millimeters) and vented at the time of fuel disruption.

c. These blockages will not severely restrict the flow of the hot, pressurized fuel (which results from the predicted core power burst) into the UAB.

d. Based upon the judgement that pressurized fuel could penetrate the initial steel restriction, the axial location of the steel blockage in the UAB was determined by the SAS calculation. Since SAS3D does not have a fuel freezing calculation, these steel blockages could then be used to restrict, but yet allow the latter fuel penetration into the UAB.

e. Relative to energetics potential, it is conservative to ignore the effect of plenum fission gases in restricting the formation of an upper steel blockage.

The review focused on the above five points and in particular, an explanation for the differences between the upper blockage formations observed in the TREAT R and SLSF P series experiments and their interpretation for CRBRP. The experiments reviewed were L3, L4, R4 through R8, P3 and P3A. Test R-8 was specifically used to confirm the effect of plenum fission gas release on upper steel blockage formation. The most appropriate analyses in support of experiment interpretation and extrapolation were determined to be those discussed in Ref. QCS760.178B4-3.

The conclusions of the current assessment are in general agreement with the earlier study, but are modified in the areas of blockage thickness and fuel penetration of pre-existing blockages. Further, the differences in the experimentally observed blockage configurations are understandable when examined in light of the different thermal and flow incoherencies which exist between them. Relative to the above listed five points, the current understanding for CRBRP can be summarized as follows:

a. In the absence of opposing plenum fission gas release, gross upward steel relocation will occur due to sodium vapor streaming once cladding melting extends fully across the fuel assembly.

b. The steel blockages start to form upon entry to the UAB and become rather thick, especially at the edges, and vented in the CRBRP size fuel assembly. The experimental data (R5, R6, P3A, P3) indicate that the blockage is vented prior to and possibly following fuel disruption. The existence of vents is a natural consequence of the direct relationship between the sodium vapor flow required to relocate steel upward and the flow resistance increase which occurs as the blockage nears completion. The thickness of the blockage is governed by the radial, thermal and flow incoherencies and explained in the following interpretation of the experiments and the CRBRP. The CRBRP fuel assembly has a larger cross-sectional area and contains 217 fuel rods, as compared with the R-series test sections which contain seven fuel rods, and the P3A and P3 test sections which contain 37 fuel rods. This will lead to greater transverse thermal incoherency within a CRBRP fuel assembly. This is

especially true since the LOF tests were designed to produce radial uniformity in the power-to-flow ratio, while a CRBRP fuel assembly is expected to experience larger radial power gradients as well as flow nonuniformities (more coolant area in the outer row of fuel rods). In a LOF, the thermal incoherency leads to varying times of cladding melting initiation among the fuel rods.

The radial incoherency in cladding melting and subsequent motion results in significant differences in the hydraulic resistance across a fuel assembly. This allows sodium vapor to be diverted from a higher resistance flow subchannel where flooding is occurring to a low resistance flow subchannel elsewhere within the assembly. The net effects are: (1) to sustain sodium vapor flow at a relatively high rate for a longer period of time and initiate molten steel sloshing without gross relocation, (2) to enhance molten steel upward motion in the colder outer subchannels of an assembly, thus increasing the upper steel plug thickness at the edges and producing a thinner central region, and (3) to locate the steel at different elevations, thus leading to irregularly shaped vented plugs. The results from the 37-rod P3A test generally support these conclusions, as compared with the results from the 7-rod R-series tests.

The effects of thermal incoherency on molten cladding relocation were studied. Calculations have been performed for tests R4, R5, and P3A, as well as FFTF and CRBRP assemblies. The results were generally in good agreement with the corresponding tests, and supported the trend toward thicker upper blockages for the larger assemblies, (Ref. QCS760.178B4-3).

c. Based upon preliminary structural calculations, blockage regions which are near melting ($\sim$ within 50°C) will not severely restrict the flow of the hot, pressurized fuel into the UAB. Initial interpretation of SLSF test data indicates that the upper blockage in the larger scale, constant power P3 experiment may have been moveable at the time of fuel disruption which would allow pressurized fuel penetration into the UAB.

d. The experiment which could most likely provide information on this condition was TREAT R7 which represented a power burst to 15 times nominal following steel melting. However, the fuel thermal conditions could not be readily ascertained and it is likely that significant pressurization did not occur. In the CRBRP, the extent of fuel penetration into the UAB will depend upon the relative timing of steel and fuel relocations throughout the core. There is no change in the original judgement that a complete fuel blockage in the UAB, cannot be precluded

e. For the EOC-4 configuration it appears likely that the plenum fission gas would be released to the sodium flow channel (time constant of 0.25 sec) during the time of gross melting of the cladding. The cladding failure temperature and gas release time constants were estimated to be 1400°C ($\simeq$ melting) and 0.25 seconds,

respectively. TREAT Test R8 shows that under the conditions of simultaneous gas release and steel melting an upper blockage would not be formed (Ref. QCS760.178B4-1). Hence, for the conditions expected in the EOC-4 core (see QCS760.178A3, Table 5) upward steel relocation would not be expected in much of the core.

In summary, there is ample time for steel relocation prior to fuel motion in the CRBRP, primarily due to its low effective sodium void worth. However, since plenum fission gas release from irradiated rods starts almost coincident with steel melting, gross upward steel relocation is not anticipated for irradiated fuel conditions. Upward cladding blockages are however, anticipated for BOC core conditions. In this case they are characterized as forming a short distance into the UAB. The blockage is expected to be relatively thick (cm's) near the bundle edges but irregular and vented to gas flow. The onset of fueled region pressurization could disrupt regions of the steel blockage which are within 50°C of the melting point allowing fuel penetration into the UAB.

The dynamic response of the BOC-1 core and the extent of upper blockage formation throughout the core was found to only be weakly sensitive to large variations in axial blockage location (including the core/UAB boundary) and reactivity feedback parameters. Hence, the initial conditions chosen for analysis of the melt-out phase are appropriate (see response to QCS760.178B5).

References

QCS760.178B4-1 B. W. Spencer, et al., "Interim Report on TREAT Test R8, A Seven-Pin Loss-of-Flow Test with Pressurized Pins," Argonne National Laboratory, ANL/RAS 78-39, September 1978.

QCS760.178B4-2 S. K. Rhow, et al., "An Assessment of HCDA Energetics in the CRBRP Heterogeneous Reactor Core," CRBRP-GEFR-00523, General Electric Company, December 1981.

QCS760.178B4-3 M. Ishii, et al., "Multi-Channel Model for Relocation of Molten Cladding in Unprotected Loss-of-Flow Accidents in LMFBR's," Nuc. Sci. & Engr., Vol. 69, p. 297, February 1979.

Question CS760.178B5, -C6, -C7

-B5. What is the basis for maint ining continuous subcriticality in the high heat loss environment of early melt-out phase? What are the fuel losses (quantified), taking into account uncertainties in removal path geometries, driving pressures and freezing mechanisms?

-C6. What degree of subcriticality is required to prevent pool recriticality from thermal and fluid dynamics upset conditions? What is your position on the potential for small recriticalities to amplify? What is the justification for your position?

-C7. In assessing benign termination from the boiled-up pool, justify the fuel removal mechanisms and rates. In particular, assess the potential for upper pool sodium entry via rapid condensation of steel vapor pressure.

Response

The key points in the above questions are: (a) basis for continuous subcriticality. (b) fuel removal uncertainties relative to path, driving pressure and freezing mechanism, (c) fuel removal required to prevent recriticality, (d) potential for amplification of recriticality events, (e) termination of boiled-up pool phase including consideration of sodium reentry. Since these points are all related to the case for achieving a condition of permanent subcriticality following the initiating phase without large energetic reactivity insertions, they are addressed in an integrated manner in this response.

In previous analysis Ref. QCS760.178B5-1 it was shown that early fuel removal through interassembly gaps prevented the large scale pool phase (LSPP). In this reference the LSPP was considered as any contiguous molten mass which is of sufficient size such that its phenomenological behavior will dominate the accident progression relative to energetics potential.

In this response the terminology LSPP refers to the configuration after the melt-out of the internal blanket assemblies. The distinction is made between this more homogeneous configuration and that associated with the merging of molten driver fuel while the inner blanket is intact. The latter is referred to in this response as the melt-out/annular pool phase (MO/APP). This refinement is important in the context of the heterogeneous core design since the phenomenological behavior in the MO/APP introduces additional considerations with significance regarding energetics potential that would not be otherwise discussed in the context of a more homogeneous LSPP.

One of the immediate benefits resulting from the above distinction is to remove the implications that there is an extreme sensitivity to the timing of fuel removal (of the order of 1 to 2 sec) prior to the formation of the LSPP. It can be shown that there are at least several tens of seconds available for fuel removal in the interval from the onset of fuel disruption in driver fuel assemblies until the inner radial blanket fuel assemblies will experience melt-out.

So long as the inner blanket fuel remains intact, there is an effective barrier to coherent dynamic fuel motions which have the potential for

escalating into large ramp rate reactivity insertions. The time required to destroy this barrier is found to be long relative to either (a) the time for fuel removal through several available escape paths such as interassembly gaps and control channels or (b) the time for removal of obstructions to fuel escape in the upper axial blanket (UAB) region.

In this response, consideration has been given to the implications of the extended time scale of the melt-out/annular pool phase (MO/APP) relative to the homogeneous LSPP. Both the potential for recriticality events as well as alternate fuel escape paths have been considered including the potential for sodium re-entry. As a result it is concluded that:

1. Once molten fuel becomes available on a assembly basis, mild recriticality events may be possible but they are limited in amplitude and do not amplify.

2. Multiple paths for fuel removal are available on a short time scale, relative to the melt-out of internal blanket assemblies. Correspondingly, fuel removal is not overly sensitive to fuel penetration model assumptions and fuel escape impedances.

3. There is always time for sufficient fuel removal, i.e., about 40% of the driver fuel, to achieve permanent subcriticality prior to loss of the annular inner blanket barrier.

4. The accident sequence will terminate benignly without the development of a homogeneous large scale confined pool phase as defined in (Ref. QCS760.178B5-1).

5. Sodium re-entry can be ruled out on the basis of excessive sodium vaporization when liquid sodium comes into contact with molten fuel and steel materials.

The details of the response are contained in the following sections. First, the beginning of the melt-out phase is characterized with respect to likely conditions in the driver and blanket fuel assemblies. Then a discussion of the possibility of recriticality events is presented supporting conclusion (1). In the next section fuel removal paths are identified followed by a discussion of the time scale on which these paths are made available. Fuel penetration mechanisms are discussed as well as sensitivity to external constraints, supporting conclusions (2),(3), and (4). Finally a discussion relating to the potential for sodium re-entry is provided to support conclusion (5).

Beginning of Melt-Out Phase

The melt-out phase of the accident sequence begins when fuel within individual assemblies in the driver core region starts the process of melting through hexcan wall barriers. For both the BOC-1 and EOC-4 core, this action begins after ≈ 20 seconds of initiating phase events (sodium boiling, cladding, and early fuel motion). At this time most of the driver fuel assemblies have experienced fuel disruption (∿ 1-2 s time scale). Internal blanket (IB) assemblies are not voided in the BOC-1 core and have an average fuel temperature ≈ 1000°C at the core midplane. For the EOC-4 core, IB assemblies may be

partially voided at an average blanket fuel temperature closer to 2000°C at the core midplane. The ratio of blanket fuel to driver fuel specific power level is approximately 1 to 10 for the BOC-1 core and approximately 1 to 3 for the EOC-4 core.

Early in the melt-out phase the driver fuel power level may be about 75 w/g (50% of nominal) tending perhaps to as low as 15 w/g as the merging of assemblies into a continuous annular fuel region becomes more complete. These power levels represent bounds below which, recriticality events cannot be precluded. At higher levels, vapor generation would boilup the pool and largely preclude such events. Recriticality events which do occur would be expected to be very mild and infrequent.

Based on the initiating phase analysis performed so far, cladding blockages are likely to be formed at the bottom of the core. Upper cladding blockages may also be formed, but vented in most of the BOC-1 core. In the EOC-4 core, upper cladding blockages are not expected in view of the effect of plenum fission gas release on cladding movement, as addressed in Response to CS760.178B-4. Therefore, it is concluded that fuel removal into the upper axial blanket region is possible depending on core conditions.

The gaps between hexcan walls which are not adjacent to boiling fuel regions are expected to remain open, not only in the region outside the core, but also in the core region. In the BOC-1 core, the gap sizes are expected to be similar to the fabrication dimensions (0.47 cm) because of negligible swelling of the hexcan steel. In the EOC-4 core driver fuel region, the hexcan steel swelling reduces the gap sizes on the average to about two thirds of the fabrication dimension. Therefore, the interassembly gaps are expected to provide a viable fuel removal path not only in the BOC-1 core but also in the EOC-4 core.

Based on the relative conditions of the driver fuel and the blanket assemblies it is estimated that the time interval between the onset of fuel driver disruption and breakdown of the IB barrier to form a homogeneous pool would be ≈ 150 seconds for the BOC-1 core condition and ∿ 50 seconds for the EOC-4 core condition based on adiabatic heating. If driver fuel does not flow rapidly from the core region it may also enter and penetrate the IB assemblies causing the IB to melt-out at greater than the adiabatic rate. As shown in Appendix A to this response this effect would reduce the above indicated time intervals by no more than a factor of four for BOC-1 and two for EOC-4 conditions, respectively.

Recriticality Events

Recriticality events following the initiating phase have been considered. Such events cannot be generically ruled out in the high heat loss environment at the assembly scale as power decreases to decay heat levels. Fuel compaction is limited by vapor separation and cannot introduce reactivity ramp rates exceeding 20¢/s/assembly which during the early time period would be mitigated by core-wide incoherencies.

Vapor condensation due to influx of cladding steel will be limited since colder steel will be covered by a thermally stable fuel crust. No mechanisms

have been identified which can fragment and rapidly distribute cold steel within the pool.

However, some gradual reduction in vapor flux cannot be precluded with the resultant compaction of fissile material. The response is self-dispersive since an increase in power will very rapidly increase vapor production in the near saturated pool, leading to a reduced fissile density. Reoccurrence and amplification would be possible if the physical event behaved and responded as continuous liquid slug elements bounded by expanding and compressing vapor spaces. However, this is not found to be likely because of vapor-liquid break-up processes resulting from the growth of Taylor type instabilities. These mechanisms and their application to the MO/APP are discussed in Appendix B to this response. It is concluded that the fuel-steel boiling process within a disrupted heterogeneous core should be stable to mild recriticalities at least as long as the annular geometry dominates the fluid dynamic behavior.

Fuel Removal Paths

Fuel removal paths important to the termination of the accident sequence include: (a) the upper axial blankets, (b) interassembly gaps, (c) control rod channels, and (d) radial blanket assembly void space.

Upper Axial Blankets - The upper axial blanket regions of the driver fuel assemblies provide a fuel escape path on two levels of consideration. On an early time scale, cladding blockage are likely to prevent upward fuel escape for BOC conditions. However, for EOC conditions, downward cladding relocation driven by plenum fission gas escape, will leave an upward escape path for subsequent disrupted fuel. Accounting for coolant channel volume fraction the driver fuel removed upward would be $\sim$ 1% per cm of penetration into the UAB (on a assembly basis).

On a larger time scale (several tens of seconds) cladding blockages in the upper axial blanket can be removed as an obstruction to fuel escape by virtue of ablative melting or in EOC conditions by melt-out of the hexcan boundary in the UAB region. The latter can reasonably occur on a time scale of less than 10 sec depending on the fuel penetration.

Interassembly Gaps - Figure QCS760.178B5-1 shows the side view of the gaps in the region below the core, and the radial blanket/shield regions. The dimensions shown in this figure are fabrication dimensions at room temperature. Although the gap sizes could be larger in actual cases due to thermal expansion, the fabrication dimensions are used in the present estimation of the gap volume. Furthermore, it is assumed that the gaps in and below the shield block region (.17 cm) will not be available due to fuel plugging as it flows into this constricted region.

Thus, the volume of the gaps available for fuel removal from the core region is estimated, and the results are given in Table QCS760.178B5-1. This table shows that the total gap volume below and outside the core region is much larger than the total liquid volume of the core materials: fuel, cladding, and assembly hexcan walls.

The interassembly gap width in the core region has been calculated using the SAS3D results for the initiating phase at a point in the transient around

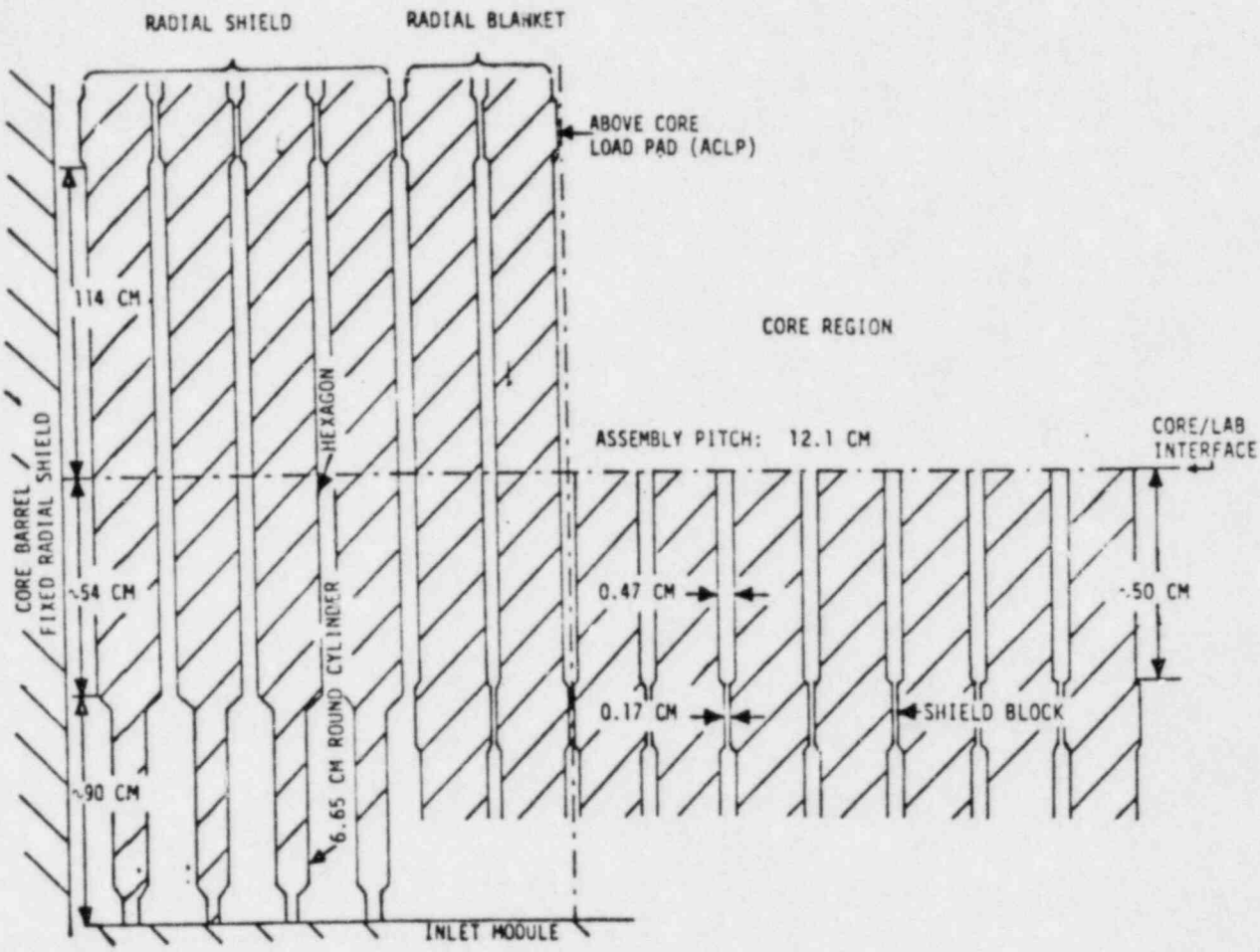

Fig. QCS760.178B5-1 Sketch Showing the Interstitial Gaps Outside and Below the Core Region.

Table Q760.178B5-1

TOTAL VOLUMES OF CORE MATERIALS AND GAPS BETWEEN ASSEMBLIES

Location	Volume (Liters)
Region Below Core	
Between Core/LAB Interface and Shield Block	110
Radial Blanket Region	
Between Core/LAB Interface and Shield Block	60
Between Core/LAB Interface and ACLP*	110
Radial Shield Region	
Between Core/LAB Interface and Inlet Module	1800
Between Core/LAB Interface and ACLP	250
Region Between Radial Shield Assemblies and Core Barrel	
Below Core/LAB Interface	1300
Between Core/LAB Interface and ACLP	1200
TOTAL	4830**
Total Fuel Assembly Volumes in Core Region (BOC-1)	
Fuel in Liquid State	700
Cladding in Liquid State (including wire wraps)	310
Hexcan in Liquid State	210

*Above-core load pad at 13 cm into UAB.

**This represents 690% of total core fuel volume..

the initiation of fuel disruption in the lead assemblies. The hexcan walls in the below-core and radial shield regions have experienced little swelling at both BOC-1 and EOC-4. Therefore, the gap widths in these regions are expected to be approximately 0.48 cm which is a fabrication dimension (0.47 cm) plus thermal expansion. The gap width in the radial blanket regions is taken to be an average between the gap widths in the core and radial shield regions. The gap sizes are summarized in Table QCS760.178B5-2.

Control Rod Channels - The fuel removal flow paths in the nine primary and six secondary control assemblies in the reactor core are schematically shown in Figs. QCS760.178B5-2 and -3. The primary control assembly (PCA) has a moveable inner hexcan (attached to the control rods) which partially protrudes into the active core zone. The annular gap which is formed with the outer hexcan has a hydraulic diameter and flow area of approximately 0.75 cm and 5 cm^2, respectively. The main path for fuel flow is downward into the large open area (empty hexcan) below the moveable control, then through a 3.7 cm diameter hole in the shield region to the orifice zone (8.4 cm diameter). The orifice zone consists of seven one cm thick plates, each of which has six equally spaced and parallel 1.07 cm diameter holes. The plates are separated by open spaces (8.4 cm diameter) 1.27 cm high. After passing through the orifice zone the fuel flows into the inlet nozzle (D_H = 6.35 cm, A = 12.47 cm^2), then into the large inlet module and ultimately into the reactor inlet plenum.

The secondary control assemblies (SCA) have a different configuration (Fig. QCS760.178B5-3) with the initial path again through an annular region (D_H = 0.67 cm, A = 38.5 cm^2) past an orifice zone (D_H = 0.84 cm, A = 7,4 cm^2) into the inlet module. After melting through the guide tube an alternate path is available through a large open area (D_H = 10 cm) and outlet (D_H = 3 cm) into the SCA low pressure plenum (in the inlet module) and then outward to the core barrel region. However, no credit for fuel flow beyond the vent will be taken since an assessment of freezing and plugging potential has not been completed.

Table QCS760.178B5-3 provides the available volumes for fuel removal based on the above geometries.

Radial Blanket Assembly Void Spaces - In parallel with melt-through of the inner blanket and control assembly barriers, it is also reasonable to examine the volume available in the outer radial blanket assemblies due to the long time frame available. From geometric considerations the volume readily (sodium flow area) available in the first row of the outer radial blanket represents about 20% of the driver fuel volume.

Fuel Removal Necessary to Assure Permanent Subcriticality - Table QCS 760.178B5-4 shows reactivity levels for various disrupted core configurations at BOC-1 (see Appendix C for details of the neutronics modeling). Case 1 represents core conditions after approximately 43% of the total fuel inventory is removed from the core, the remaining fuel in the core annular regions is homogenized and fully compacted, while the internal blanket and control assemblies remain intact. The system is subcritical for this configuration. Case 2 is identical to Case 1 except that the fuel removal is reduced to 33% of the total inventory. The system is substantially above critical for this configuration. In Case 3, about 41% of the total fuel inventory is again

Table QCS760.178B5-2

WIDTHS OF INTERASSEMBLY GAPS IN CORE REGION
AND EX-CORE REGIONS

Locations	Gap Width, cm	
	BOC-1	EOC-4
Core Regions		
Between Non-Boiling Assemblies	0.41-0.51	0.22-0.48
Between Non-Boiling Fuel and IB Assemblies	0.42-0.49	0.24-0.49
Between IB Assemblies	0.43-0.48	0.26-0.50
Ex-Core Regions		
Below Core	0.48	0.48
Radial Blanket	0.45-0.48	0.35-0.48
Radial Shield	0.48	0.48

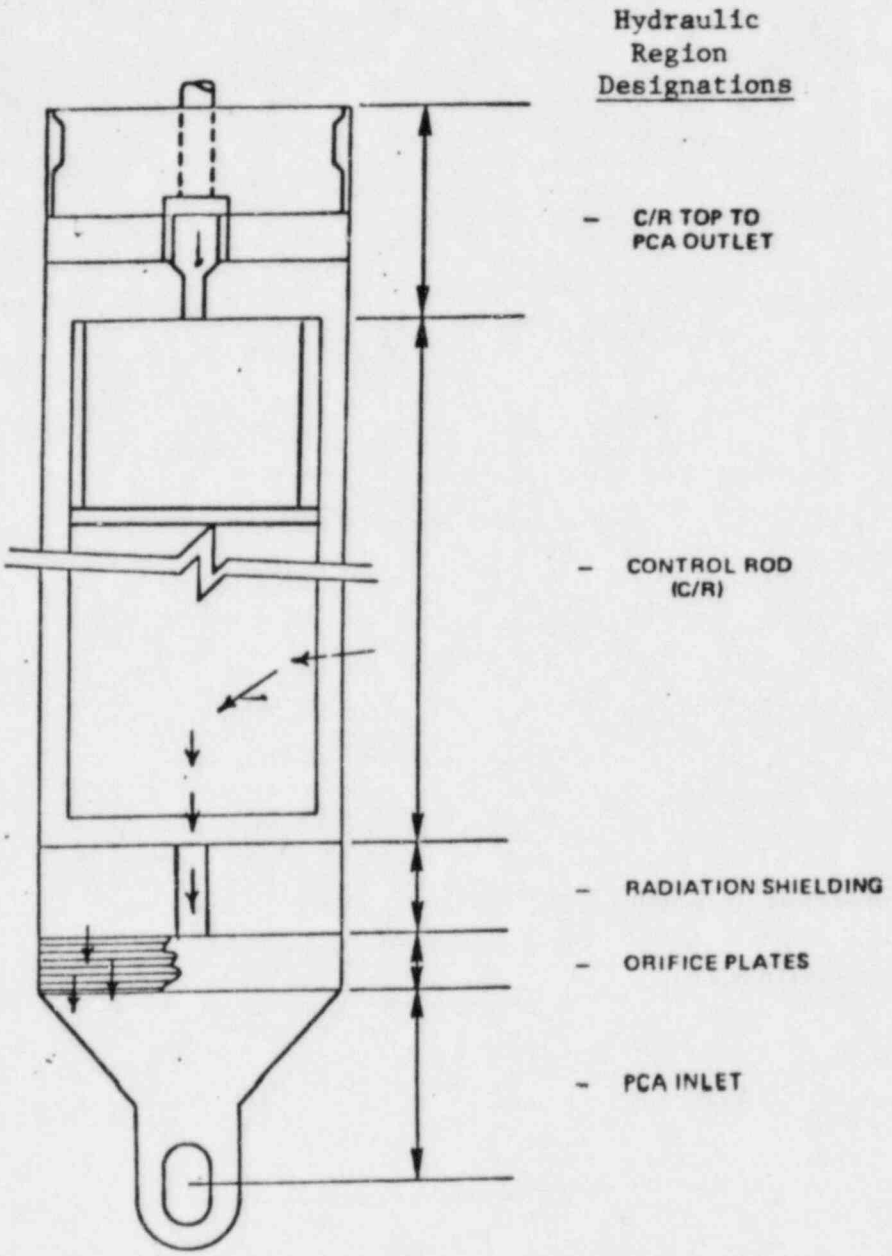

Fig. QCS760.178B5-2 Schematic of Primary Control Assembly.
⟶ Indicates Fuel Flow Path.

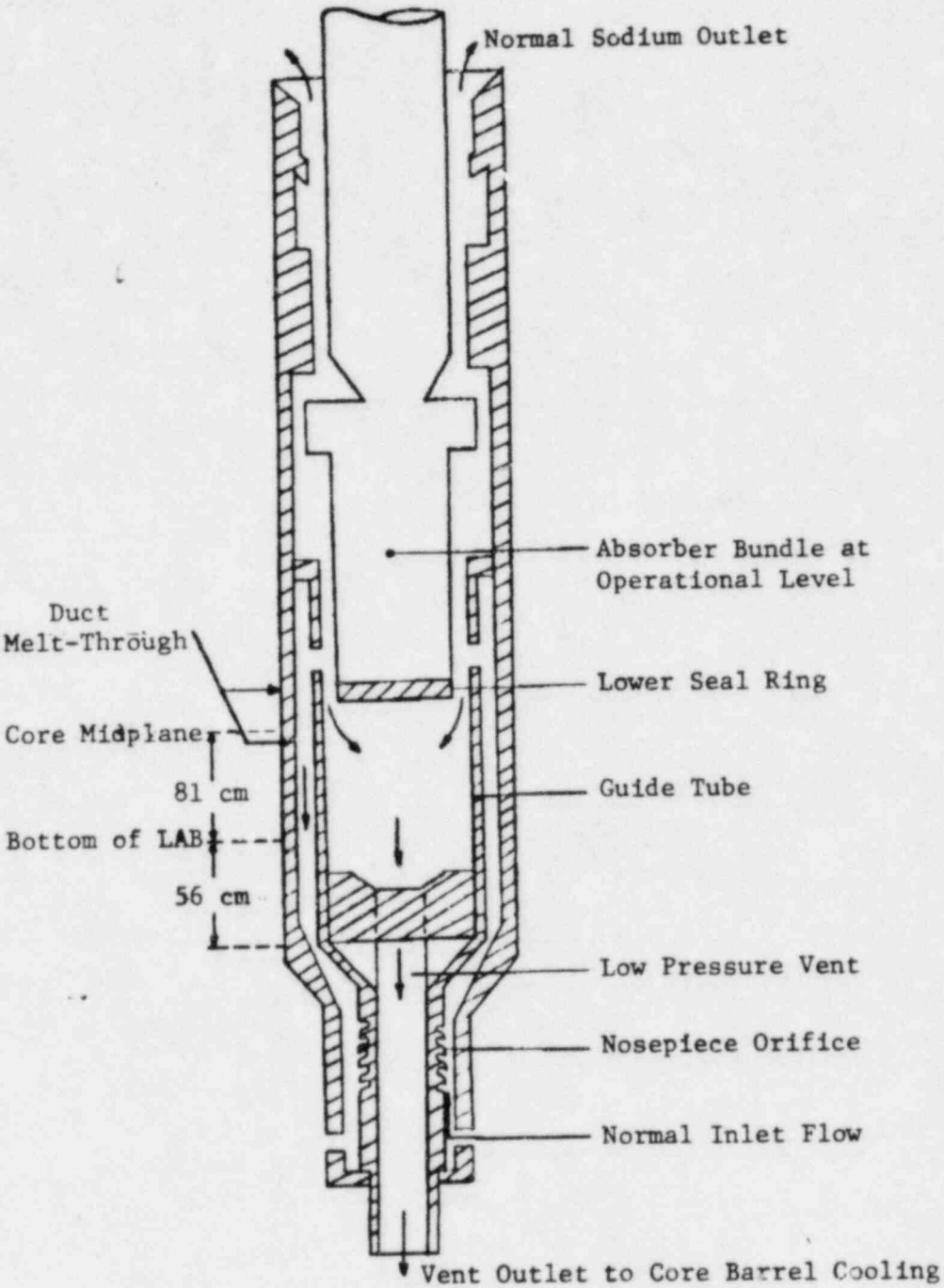

Fig. QCS760.178B5-3 Schematic of SCA Flow Paths for Fuel Removal (not to scale).

Table QCS760.178B5-3

VOLUMES AVAILABLE TO ACCOMMODATE FUEL IN PRIMARY AND SECONDARY CONTROL ASSEMBLIES

	Primary	Secondary	Approximate Core Fuel Fraction[1]
Number of Assemblies	9	6	-
Volumes Below Core/LAB Interface to Flow Restriction (liters)[2]	50	29	0.11
Lower Inlet Modules (liters)	292	-	0.42
Total Volume Available (liters[3])	342	35	0.53

NOTES:

1. Based on 6000 kg of fuel at 8.6 kg/l liquid density.
2. Flow restriction assumed to be orifice plates in PCA and low pressure vent outlet in SCA; see Figs. Q760.178B5-2, -3 for details.
3. Fuel loss through PCA lower inlet module to reactor inlet plenum not indicated here.

Table QCS760.178B5-4

REACTIVITY LEVELS FOR VARIOUS DISRUPTED CORE CONFIGURATIONS AT BOC-1

Case	Description of Core Configuration	Reactivity ($)
1	43% of total fuel inventory removed from the core. The remaining fuel in the annular regions is homogenized in the core and fully compacted with IB and CR assemblies intact.	-1.4
2	Same as Case 1 except that only 33% of total fuel inventory is removed.	+10.2
3	41% of total inventory removed from core. The remaining fuel, the IB and CR (except B_4C) assemblies are homogenized and fully compact.	-10.5

removed from the core. The remaining fuel, internal blanket and control assemblies (without B_4C) are assumed to be homogenized and fully compacted. This homogeneous pool configuration is substantially subcritical. From these neutronics results, it was concluded that the system will achieve permanent subcriticality as long as about 40% of the total fuel inventory is removed from the core. Based upon preliminary calculations, this also appears to represent a good estimate for EOC conditions.

Time Scale to Make Fuel Removal Paths Available Relative to the Annular Pool Phase

Fuel escape paths become available on a short time scale. At EOC conditions the UAB is open at the onset of fuel disruption. Other escape paths become available on a time scale of several seconds following fuel disruption due to melt-through of hexcan boundaries.

The hexcan wall melt-through time was calculated using a finite-difference method. This calculation initiates from the time a molten fuel pool has developed. Initial hexcan wall temperatures for this calculation were determined based on SAS3D calculations. A typical hexcan wall temperature profile just prior to boiling of the assembly molten pool is plotted in Fig. QCS760.178B5-4.

Heat transfer coefficients at the hexcan wall (with stable fuel crusts) were determined from the correlation of internally heated boiling pool test data of Ref. QCS760.178B5-2. Based on this correlation, the heat transfer coefficient for a boiling pool of fuel-steel mixture was calculated to be approximately 2 $w/cm^2-°K$. The heat transfer coefficient at the bottom of the pool may be lower than this value because the pool is expected to be more quiescent in this region. The heat transfer coefficient for a quiescent pool is as low as 0.2 $w/cm^2-°K$ according to Refs. QCS760.178B5-1 and QCS760.178B5-3. This means that the can wall heat transfer coefficient in the bottom region of the pool can be in the range from 0.2 to 2 $w/cm^2-°K$. The boiling pool temperature is expected to be 3100°C - 3200°C which is the steel boiling point at an assembly pressure of 3-5 bars.

Based on the above thermal characteristics the hexcan wall melt-through times were calculated using the typical hexcan wall temperature profile (Fig. QCS760.178B5-4) as the initial temperature profile. The results are plotted in Fig. QCS760.178B5-5, which indicates that the major portion of the hexcan wall will melt through within 2 seconds after the boiling pool is formed inside the hexcan.

The flow path through the control assemblies will become available approximately four seconds after being contacted by the boiling (3200°C) fuel-steel pool. This value is based upon a thermal analysis comparable to that just discussed for melting of the fuel assembly hexcan, except that the appropriate internal sodium flow ($\sim$ 20% of nominal), geometry and temperatures ($\sim$ 400°C) are considered. The estimated melt-through time is approximately proportional to both the driving temperature difference and heat transfer coefficient. Variations in these parameters, which control heat losses from the pool are offsetting in that the pool temperature will increase for reductions in the heat transfer coefficient. Hence, for the expected parameter variations, the control assemblies become available within several seconds

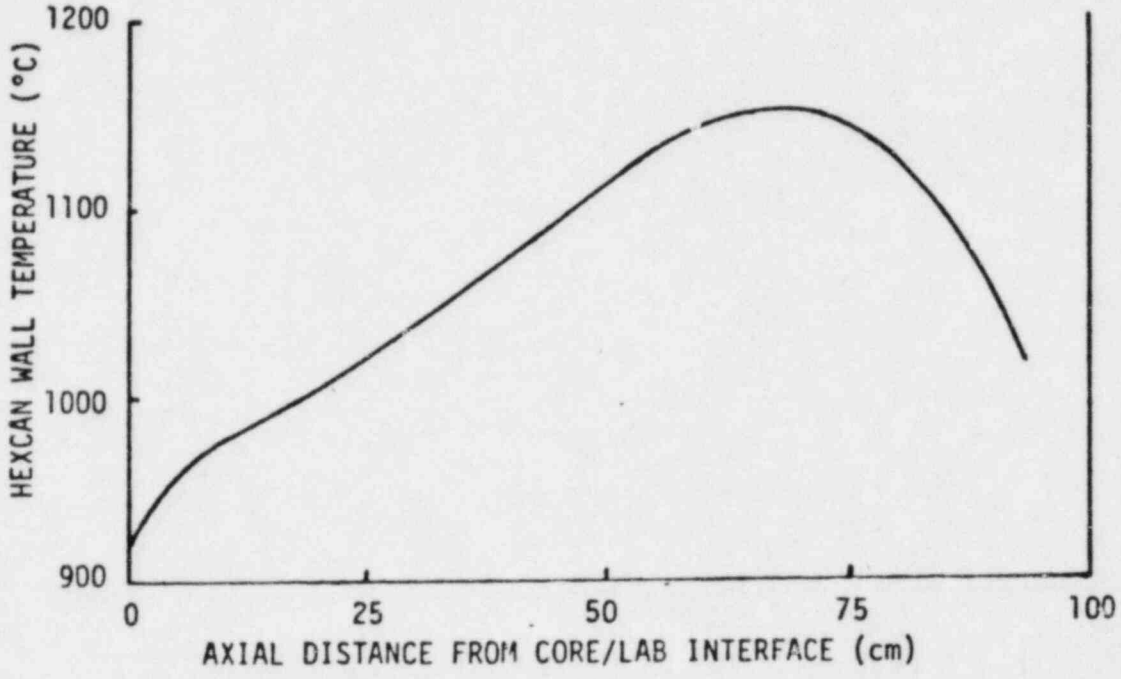

Fig. QCS760.178B5-4 Typical Hexcan Wall Temperature Distribution at Initiation of Pool Boilup.

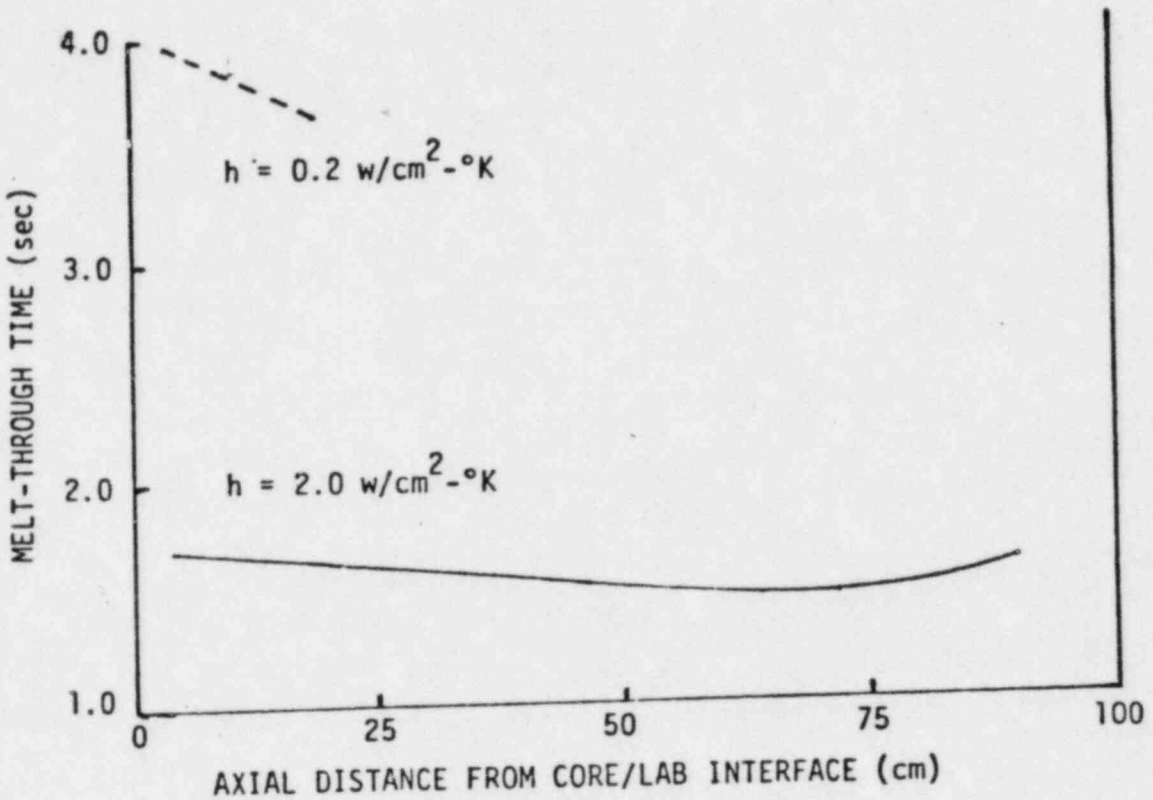

Fig. QCS760.178B5-5 Hexcan Wall Melt-Through Time Since Initiation of Pool Boilup. (Upper Dashed Curve Characteristic of 25 cm Quiescent Region. Lower Solid Curve Characteristic of Fully Boiled Up System).

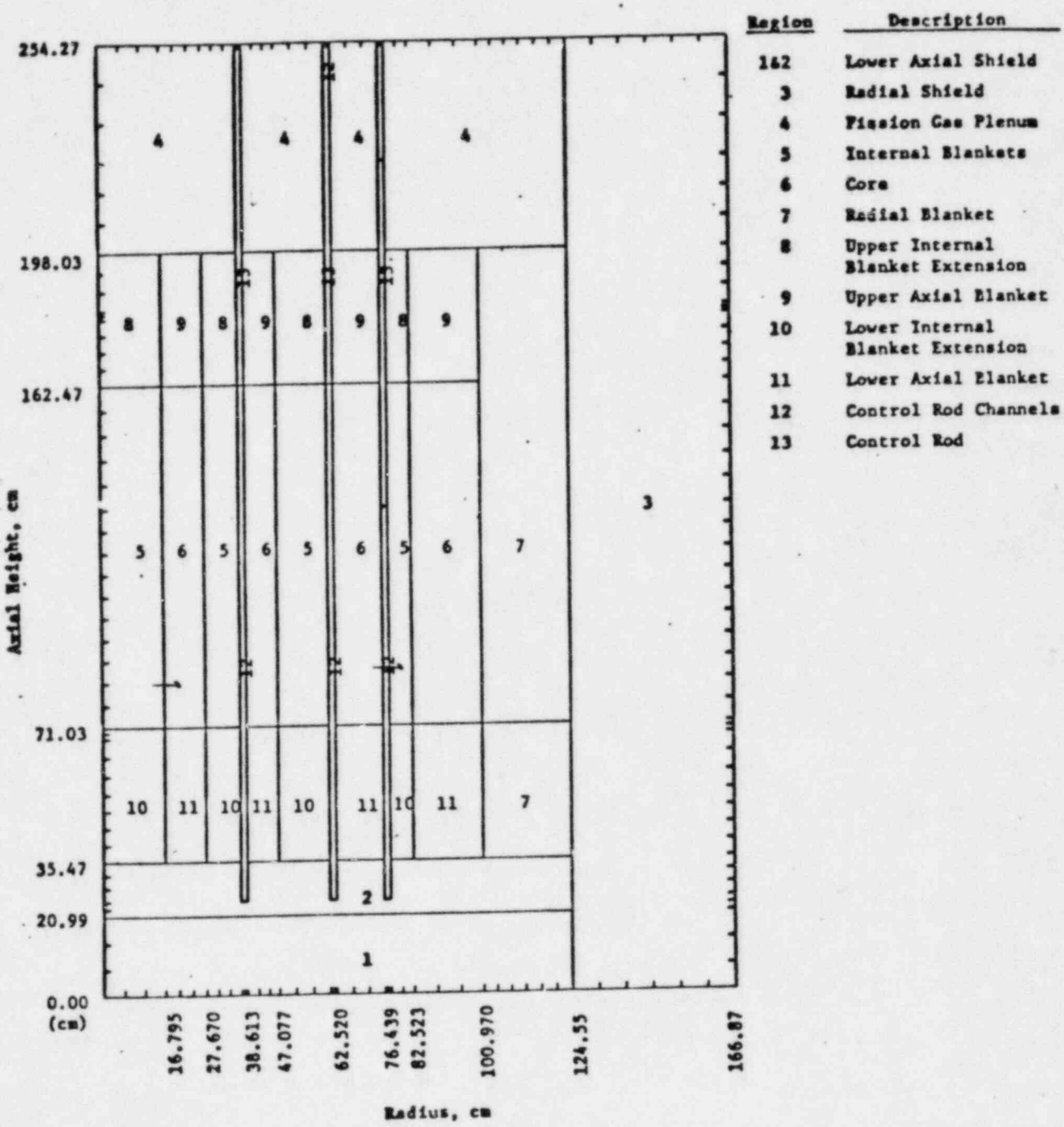

Fig. C-1 CRBRP BOC-1 Melt-Out Phase Base Case.

The results of Cases 1, 2, and 3 appear in Table QCS760.178B5-4 in the main response.

References for Appendix C to QCS760.178B5, -C6, -C7

C-1 ENDF/B Summary Documentation, BNL-NCS-17541 (ENDF 201), 2nd Edition (ENDF/B-IV), compiled by D. Garber, available from National Nuclear Data Center, Brookhaven National Laboratory, Upon, New York, October 1975.

C-2 H. Henryson, II, et al., "Mc^2-2: A Code to Calculate Fast Neutron Spectra and Multigroup Cross Sections," Argonne National Laboratory, ANL-8144, June 1976.

C-3 B. J. Toppel, et al., "ETEO-2/MC-2/SDX Multigroup Cross Sections, March 14-16, 1978 Radiation Shielding Information Center, Oak Ridge, Tennessee.

C-4 C. E. Till, et al., "Fast Breeder Reactor Studies," Argonne National Laboratory, ANL-80-40, July 1980.

APPENDIX D TO: Question CS760.178B5, -C6, -C7

Freezing Mechanisms

In Ref. D-1, a conduction-limited freezing model was determined to be most appropriate in analyzing fuel flow behavior in gaps or small tubes. Since there has been a concern over applicability of the freezing model in the presence of steel melt layers under fuel crusts and in the case of two-phase mixtures flowing in the gap, this concern is addressed in this Appendix. Again, it is concluded that the conduction-limited freezing model is applicable even when steel melting occurs under the fuel crust, and the gap flow is a two-phase mixture.

Penetration and Freezing of Flow in Melting Channels

When fuel penetration commences between the hottest assembly can walls exceeding $\sim$ 800°C, the molten fuel-steel hexcan interface temperature will fall between the fusion temperatures for these materials upon contact, resulting in solidification in the molten fuel and melting of the underlying hexcan (gap) wall. Even for sufficiently low initial hexcan temperatures such that melting of the steel hexcan does not begin upon contact with the fuel, steel melting may begin after convective heating from the molten fuel stream raises the fuel crust-solid steel interface temperature to the steel melting temperature. This is likely to occur at locations where the fuel temperature is $\sim$ 100°C or more above its melting temperature, that is in regions of the core where the fuel first enters the gaps (entrance region).

The concern with the existence of steel melt layers is that they may cause the protective fuel crust to become unstable leading to rapid fuel freezing by bulk solidification (Ref. D-2) or steel freeze plugs as a result of rapid mixing between fuel and steel (Ref. D-3), as have been postulated for thermite fuel penetration into rod bundle geometry*. It is important to note that the observed behavior of a growing freeze layer on a melting (or fluid) surface does not support the aforementioned mechanisms for rapid freezing in simple flow geometries. The formation of stable, growing freeze layers on the surface of turbulent flows by radiative and convective heat loss to the surrounding atmosphere is quite common. This situation is most prominent in rivers and lava flows. Here stable crust covers are formed under conditions in which the "underlying" fluid is air. In fact, a stream of molten UO_2 flowing over the lip of a tungsten crucible into a helium atmosphere was observed to form a tube of solid UO_2 through which the remaining UO_2 was forced to flow (Ref. D-4). Thus, flowing fuel will ignore the presence of the surrounding steel melt and grow its own channel wall (similar to the lava pipes familiar to the geologist (Ref. D-5). This conclusion also is confirmed by an experimental study in which hot Freon 112A (melting point 40°C) was injected into a thick-walled ice pipe maintained as its melting temperature throughout (Ref. D-6). While the major emphasis in this study was on the melting attack of the ice pipe wall by very hot turbulent flowing Freon,

*To date, no experiment has been performed that gives direct evidence of bulk solidification.

follow-up studies (Ref. D-7) at low Freon injection temperatures show the continuous conduction-limited buildup of a stable Freon layer on the melted ice wall until the pipe is closed to the Freon flow by the solidified layer.

Regarding the problem of mixing between flowing fuel and melted steel in regions where the gap wall may be subject to severe ablation by the fuel flow, it is pertinent to note that ice pipe ablation experiments show no appreciable mixing between the hot pipe flow (Freon) and the melted ice (Refs. D-5, D-7). In some experiments performed at very high Freon flow velocities (Ref. D-6), in the range 7.0 - 17.0 m/s, some of the melted ice in the form of water droplets was entrained by the bulk Freon flow. However, the volume fraction of entrained water was low and the process did not lead to a flow blockage by bulk solidification and/or freezing of the water component. In the ice pipe experiments reported in Ref. D-8, the water film produced along the melting ice pipe wall was found not to be entrained, despite Freon flow Reynolds numbers and velocities as high as 53,000 and 3.0 m/s, respectively. Thus, contrary to the steel-fuel mixing postulated for thermite fuel injected axially into rod bundle configurations, it would appear that very little mixing would take place between fuel and melted steel within the simple gap geometry.

Recently, measurements of the penetration of UO_2 into a thick-walled steel tube have been reported (Refs. D-9, D-10). We present below in some detail a discussion of this so-called TRAN series of in-pile experiments since it represents one of the few series of experiments carried out with pure UO_2 melts (including the conditions of steel wall melting upon contact with fuel) and since there seems to be some confusion in the literature regarding the interpretation of the experiments (Refs. D-9, D-10).

In the TRAN series of in-pile experiments, pure UO_2 is melted using neutronic heating in the Annular Core Research Reactor at Sandia. The UO_2 melt is then accelerated upward into a 130-cm long, steel freezing tube with a 0.32-cm diameter channel by the application of high pressure helium gas to the base of the fuel. Four such experiments have been performed to date, with the injection pressure held approximately constant at 1.0 MPa, the initial steel temperature varied from 400 to 900°C, and the initial fuel temperature varied from 2900 to 3500°C (Ref. D-11). Post-test analysis of cross sections of the tube indicated that melting of the steel wall occurred in the test where the initial steel temperature was 900°C. In all the experiments, the observed final fuel distribution consists of a frozen fuel layer that covers the inside surface of the tube and fuel debris located above the end of the fuel layer (Ref. D-11). The length of the fuel layer varies between 48 and 87 cm, depending on the amount of fuel injected into the tube during any given test (see below). In one experiment, a complete fuel blockage $\sim$ 2 cm long was observed between the fuel debris region and the end of the frozen layer.

A plausible explanation for the existence of the frozen fuel layer, as opposed to a long fuel plug that fills the tube cross section is that when the fuel melt is forced upward into the cold tube the ensuing fuel penetration and freezing process is influenced by the rapid formation of an annular fuel film-helium gas flow. That annular flow is likely due to the limited quantity of fuel material that enters the tube. A possible explanation for the presence of loose fuel debris and, in one test, a short blockage beyond the frozen fuel layer is that in annular flow the gas (helium) core usually

contains a significant number of entrained droplets (fuel) or suspended liquid slugs which can be carried upward by the gas flow to the "clean" tube wall above the fuel layer. While the observed fuel penetration distance is postulated to be due to the limited quantity of fuel material employed, the frozen fuel-layer configuration is demonstrated below to be compatible with the simple conduction-limited freezing mechanism.

In the TRAN tests, about 40 g of UO_2 was rapidly melted; however, only about 20 g of UO_2 entered the freezing tube (Ref. D-11). Vortex motion in the fuel sample may have been responsible for the reduced amount of fuel forced upward into the tube. Whatever the mechanism responsible for the limited quantity of fuel injected into the tube, one could reason as follows: the melt first enters the tube as an all liquid advancing flow, with the only gas-melt interface present being that at the flow front. After the $\sim$ 20 g of fuel melt inventory enters the tube, the flow pattern instantaneously changes into a slug flow in which a single fuel slug (or column) now occupies $\sim$ 25 cm of the tube, followed by the high pressure helium gas. The lower helium gas-fuel interface that must now appear at the tube inlet is highly unstable such that a long finger or bubble of the less dense helium gas penetrates the UO_2 melt slug. That is, at any location after the helium gas-fuel (lower) interface has passed, the heavier molten UO_2 is not completely expelled or replaced by the lighter helium gas. A film of molten UO_2 will adhere to the tube wall while a tongue or finger of the helium gas of reduced diameter advances through the tube core established by the portion of the fuel melt left behind. The helium gas finger should penetrate steadily through the fuel slug with little change in profile until the upper fuel-gas interface or flow front is approached causing the fuel slug, now greatly diminished in size, to burst. The bursting of the slug could result in the "throwing" of some of the melt material above the region occupied by the fuel film, which would explain the presence of loose fuel debris and small blockages beyond the end of the frozen fuel layer. Alternatively, portions of the fuel film may be entrained by the helium gas flow and redeposited on the tube wall downstream of the fuel layer.

There is much direct evidence for the transient slug annular flow transition described in the foregoing. In boiling experiments reported in Ref. D-12, a rapid depressurization technique was used to initiate vapor growth in superheated liquid Freon-113 within a tube. The vapor bubble so formed was observed to act like a piston, pushing the liquid slug out of the tube as it expands, but leaving behind a residual liquid Freon film on the tube wall. In a series of experiments reported in Ref. D-13, air was used to accelerate water or water to accelerate mercury through a tube. Interface displacement measurements clearly indicated that a film of the heavier fluid was left behind after the interface had passed. The explanation for the more dense fluid being left behind is rather straightforward: given an initial tendency for a residual liquid film of the more dense fluid to be left behind in such slug flow processes, this tendency is enhanced by the effect of the pressure gradient acting over the fluids of unequal density (Ref. D-13). The less dense driving fluid is accelerated more rapidly than the more dense displaced fluid. This explanation is the familiar Taylor (Ref. D-14) description of the instability of a bump (or wave) of small amplitude at an interface between a heavy fluid and a light fluid when accelerated in the direction of the heavy fluid. The simple Taylor theory suggests that molten UO_2 fuel and helium gas

in the TRAN tests cannot be separated by a stable interface. The experiments described above (Refs. D-11,D-12) indicate that transient fuel penetration in the Sandia freezing tests is best characterized by a fuel-film annular flow pattern.

With regard to the problem of fuel film survival after the gas source is depleted, we note here that there is more than sufficient time to freeze the film in place by conduction before any significant film drainage can take place. In the TRAN series of experiments the thickness of the frozen fuel layer was observed to be between 0.015 and 0.03 cm. Depending on the film thickness and the initial fuel temperature, which was in the range 2900 - 3500°C, we estimate using conduction-freezing theory (Ref. D-15) that the time required to freeze the film is between $\sim$ 10 ms and $\sim$ 100 ms. Assuming laminar fuel-film flow we calculate a loss of less than 10% of the fuel material due to film drainage before freezing.

In summary, it appears highly likely that the final fuel distribution in the Sandia TRAN freezing tests can be attributed to the limited quantity of fuel employed. The "driving" helium gas displaced and penetrated the fuel melt, causing the rapid formation of an annular fuel film helium gas flow pattern. Furthermore, we expect that the fuel film is frozen in place by conduction-limited solidification; that is, the TRAN tests provided strong evidence for conduction-limited fuel crust growth into an annular two-phase fuel flow in the presence of both solid and melted steel backings. Had an unlimited quantity of fuel been available for injection into the freeze tube, we predict from Ref. D-16 a fuel penetration length of at least 250 cm.

Penetration and Freezing of Two-Phase (Fuel-Gas) Mixtures

The flowing core debris during the melt-out phase of the accident sequence is a two-phase gas (or vapor)-fuel melt mixture. Also, the core debris that enters into the gaps between assemblies may contain some amount of molten steel and solid fuel particulate. The presence of molten steel and solid fuel in large quantities will accelerate the freezing rate and increase the frictional resistance that retards the fuel flow, respectively, both of which will tend to reduce the fuel penetration distance into the gaps. Fortunately, only small quantities of these materials are expected to be carried from the disrupted assemblies into the gaps by the escaping fuel.

The source of solid fuel particulate is the unmelted portions of the fuel pellets. The unmelted fuel represents at most about 20% of the total fuel within a disrupted assembly. A large fraction of this solid material ($\simeq$ 15% volume fraction of total fuel) is located at the bottom of the assembly, away from any potential fuel escape opening in the hexcan wall, and is likely to remain at the bottom owing to its large density compared with that of molten fuel. The remaining unmelted fuel, which is located at the top of the assembly, would be carried with the fuel flow into the gaps. However, since this solid material represents less than approximately 5% volume fraction of fuel and is continuously being eroded by melting, the solid fuel debris that enters the pool from above will not retard the fuel flow in any significant way.

As with solid fuel particulate, very little molten steel is anticipated to be mixed with the molten fuel within a disrupted assembly. The time interval between the complete melting of cladding and that of fuel is such that most of the cladding is moved out of the core region under the influence of both sodium vapor streaming and gravity. Thus, the melting fuel begins to lose its geometry when only a small portion of molten cladding ($\sim$ 10%) is still present in the heated fuel region. Molten steel will also form at the boundaries of the disrupted assemblies. However, unlike the residual cladding films which are "trapped" within the melting rod bundle matrix, the melt films that clings to the hexcan wall are likely to be stable and not entrained by the disrupted fuel. The evidence in support of this conclusion is provided by the observations (mentioned in the foregoing) of stable melt-film behavior in highly turbulent channel flows with an without crust formation (Refs. D-6, D-8).

The molten fuel will move out of the core as a two-phase gas-fuel melt flow. Thus, prediction of the fuel penetration length will depend on our ability to predict (a) the pressure gradient associated with the penetrating flow of the two-phase mixture and (b) the rate of fuel crust buildup in the two-phase mixture. Methods for handling item (a) above are well established and have been reported in numerous papers on two-phase flow. A careful examination of the literature has shown that relatively few papers have dealt with item (b). However, on physical grounds, one would expect the solidification rate of a two-phase mixture to be equal to or less than that of its pure liquid component. In fact, since the rate of deposition of liquid material in a turbulent two-phase flow always exceeds the rate of phase conversion at the channel wall, one would expect the solidification rates to be the same in both cases. Interestingly enough, some experimental work has been reported by Greene, et al., Refs. D-17 through D-20 that appears contrary to this line of reasoning.

In a series of abstracts and government reports, Greene, et al., (Refs. D-17 through D-20) reported the results of an experimental investigation of the transient solidification of a gas-liquid mixture, while flowing downward through a vertical tube with a fixed freeze length. The liquids used in this study were Wood's metal (melting point 74.6°C) and paraffin wax (melting point 54°C) and nitrogen gas served as the lighter phase. Experiments were performed over a range of gas injection rates (or void fraction) and at two-phase mixture temperatures equal to and above the solidification temperature. The experiments with liquids at their freezing temperatures are of most interest. Since convection heat exchange at the solid gas-liquid mixture interface is absent in this case, these experiments should permit a clear definition of the effects of the gas phase. The experimental results indicated that as the gas flow rate (or void fraction) increased, the time to completely freeze the test section (plugging time) as well as the mass displaced through the test section decreased. While the observed decreased mass flow rate with increased mass flux could, in a qualitative sense, be attributed to the two-phase friction multiplier, the corresponding decrease in plugging time is difficult to rationalize. In the earlier publications by Greene, et al., (Refs. D-17 through D-19), the authors postulated the entrapment of nitrogen gas bubbles within the solid phase that grows inward from the wall and concluded from their experimental results that the rate of solidification may be several times faster for the two-phase case than for the single-phase case. However,

the solidification of a two-phase structure (solid plus gas) was refuted in a later report (Ref. D-20), as this process was not indicated by post-test observations of the frozen material.

Soon after, Petrie, et al., (Ref. D-21) reported results of an experiment designed to measure directly the growth of an ice layer in a water-nitrogen gas mixture. A planar test section on which ice crusts were grown was vertically suspended in a pool of water contained within a lucite bubble column of square cross section. Nitrogen gas bubbles were formed at a perforated plate located at the bottom of the column. A lateral-traversing thermocouple probe was used to measure the instantaneous ice crust thickness as a function of time. Different water pool temperatures were studied, corresponding to saturated (0°C) and superheated (> 0°C) conditions. The experiments covered a range of void fractions from 0 to 90%. The following conclusions may be made from these experiments. For void fractions up to 90%, the presence of a discontinuous gas phase in a saturated flowing liquid does not affect the freezing of the liquid. The crust surface remains smooth and the void in the two-phase mixture is not trapped in the crust in agreement with the results reports in Ref. D-20. The effect of liquid superheat on the freezing of a flowing two-phase mixture is to enhance the convective heat transfer from the liquid to the crust. The crust surface remains smooth in this case with no evidence of entrapment of the void. In both cases, the crust growth behavior can be modeled by ignoring the presence of gas (except for the effect of the gas flux on the convective heat flux). Obviously, these more direct observations regarding the rate of solidification are not in conformity with the gas-induced decrease in solidification time proposed in Refs. D-17 through D-20.

Effect of Liquid Superheat

The fuel temperature is 3100 - 3200°C in the assemblies, and decreases along the flow direction, ultimately to the liquidus point. The heat transfer coefficient, h_f, can be calculated using the forced convection part of Chen's correlation.

$$h_f = 0.023 \frac{k_f}{D_h} \left(\frac{\rho_f (1 - \alpha) u D_h}{\mu_f} \right)^{0.8} Pr^{0.4} \qquad (1)$$

The molten fuel flow velocity is high initially and then decreases with increased penetration distance. Based on typical gap flow conditions with α_2 = 0.5, the heat transfer coefficient is calculated to be approximately 5 w/cm$_2$ -°K on the average. Based on the average heat transfer coefficient, 5 w/cm$_2$ -°K, the thickness of fuel crust on the steel wall initially at 800°C is calculated for various fuel temperatures as shown in Fig. D-1.

It can be seen that the fuel crust thickness is reduced substantially when the fuel temperature is above the liquidus. At above-liquidus fuel temperatures, the crust thickness growth is rapid initially, and then levels off, or even gets reversed before the gaps are plugged (original gap = .47 cm). Namely, the gaps would not be plugged at all if the fuel temperature is as high as shown in Fig. D-1.

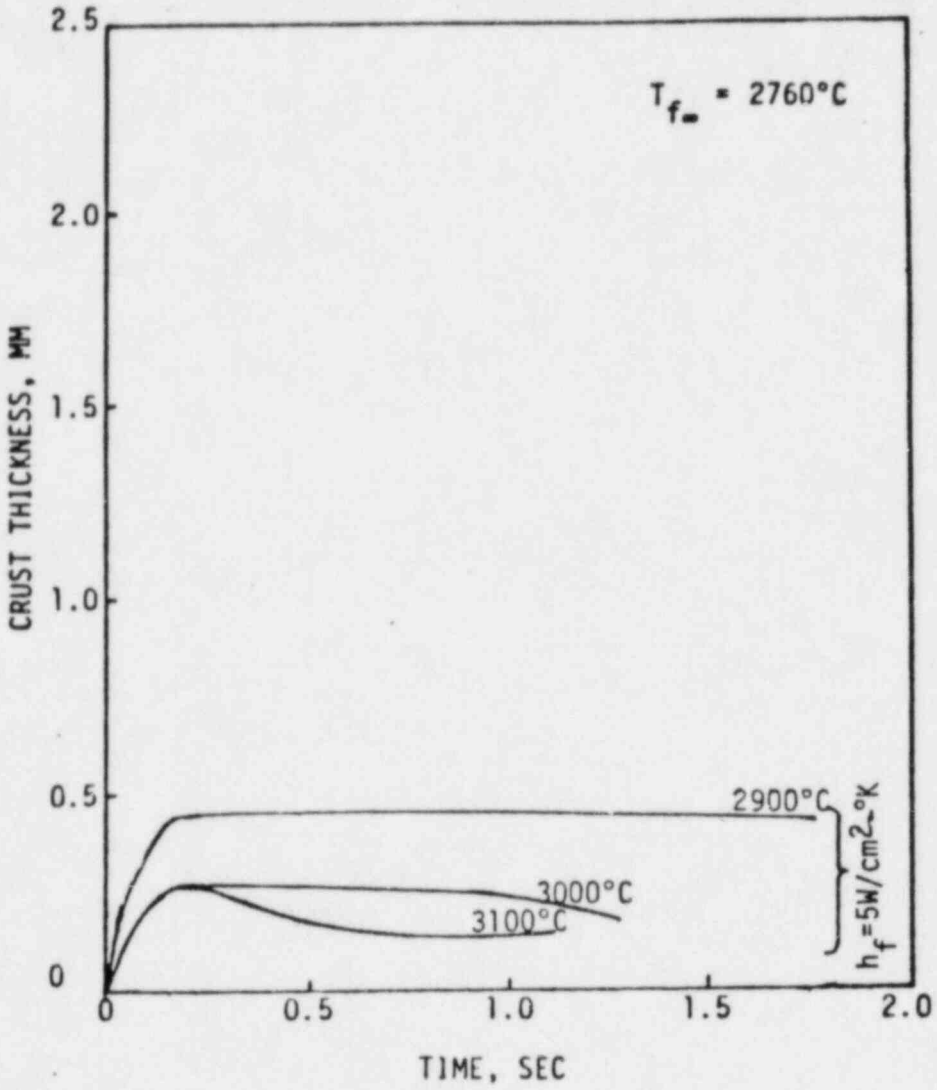

Fig. D-1 Growth of Fuel Crust Thickness on 800°C Steel Wall at Various Fuel Temperatures.

QCS760.178B5-D7

The fuel is initially at 3100 - 3200°C when flowing into the gaps and cools down to 2800°C after traveling about 30-40 cm. This indicates that the crust thickness in the 30-40 cm distance would level off at approximately 0.3 mm (see Fig. D-1); the gaps (4. - 5. mm) would remain open in this region. However, the fuel crust will continue to grow beyond this distance where the fuel is at its liquidus. Therefore, an approximate solution for this type of gap flow can be obtained by using a closed-form solution developed in Ref. D-23 for the case where the fuel is at its liquidus temperature. This closed-form solution is applied to the flow beyond the 30-40 cm distance with the pressure drop adjusted for flow inertia and friction loss in the 30-40 cm distance.

Accordingly, the distance of fuel penetration into the gaps before plugging is calculated by

$$\frac{X_p}{D_h} = 0.085 \left(\frac{\nu_f}{\lambda^2 \alpha_s} \right)^{7/11} \left(\frac{\Delta P \; D_h^2}{\rho \; \nu_f^2} \right)^{4/11} \qquad (2)$$

X_p = fuel penetration distance,

D_h = gap initial hydraulic diameter,

ρ = molten fuel density times $(1 - \alpha)$,

C_o = total wetted perimeter for outward gap flow,

ν_f = kinematic viscosity of molten fuel,

λ = growth constant (Ref. D-22),

α_s = thermal diffusivity of frozen fuel,

ΔP = driving pressure differential.

Using D_h = 0.8 cm (EOC-4 value), ρ = 4.3 g/cm^3, ν_f = 0.005 cm^2/sec, λ = 0.93, α_s = 0.0064 cm^2/sec, and ΔP = 1 bar. The fuel penetration distance is calculated to be $\sim$ 250 cm (the additional 30-40 cm penetration associated with above-liquidus fuel temperatures is neglected) which is much larger than the gap flow distance between the core boundary and the core barrel ($\sim$ 80 cm). Therefore, all the gaps outside the core could be filled with molten fuel without plugging the gap. Since the volume of the gaps in the ex-core region is much larger than the total volume of fuel, all the molten fuel could be removed from the core through the interassembly gaps while the gaps still remain open. Thus, it is concluded that fuel removal through the inter-assembly gaps is limited by the rate of fuel melting in the core, rather than by plugging of the gaps.

Bulk Freezing

In the discussion in the foregoing, prediction of fuel penetration into the gaps between assemblies is based on the conduction model, which involves the growth of a stable frozen layer at the channel wall. The results of some

experiments on UO_2 (thermite) fuel flow and freezing in subassembly structure, however, are not consistent with conduction-controlled freezing behavior. The conduction model predicts as much as an order of magnitude longer penetration distance than that observed in many of the thermite freezing tests. It has been concluded from these tests that UO_2 flowing over steel may behave in a manner that prevents the formation of a stable frozen UO_2 layer at the channel wall and, therefore, UO_2 penetration (or freezing) is controlled by turbulent heat transport from the fuel front to the channel wall ("bulk freezing model" D-2). While no direct experimental evidence exists to support this view of freezing, it has gained some popularity in the field of fast reactor safety as it provides a lower (theoretical) bound to the penetration distance of fuel in the channel geometries of interest. Accordingly, the bulk freezing model is utilized here to quantify or bound the effects of uncertainties in freezing mechanisms on fuel escape from the active core region.

According to the bulk freezing concept, the region just behind the leading edge of the penetrating fuel flow, where freezing is expected to occur first, appears as a "slush" and freezing is complete when the latent heat of fusion is "removed" from the slush by further (turbulent) heat loss to the channel wall. Assuming that turbulent heat loss within the complex "tumbling" flow pattern that must exist in the vicinity of the fuel front is well represented by Reynold's analogy, the penetration X_p of fuel limited by bulk solidification is readily shown to be given by D-24.

$$X_p = \frac{1}{2}\frac{D_h}{f}\frac{h_{f\ell}/c + (T_o - T_{mp})}{T_o - T_w} \tag{3}$$

where f is the dimensionless coefficient of friction ($f \approx 0.005$), D_h is the hydraulic diameter of the channel, $h_{f\ell}$ and c are the latent heat of fusion and the heat capacity of the flowing fuel respectively, T_o and T_{mp} are the fuel temperature at the channel entrance and the fuel melting temperature respectively, and T_w is the temperature of the channel wall. Within the context of bulk freezing theory, it is assumed that T_w is equal to the melting temperature of the steel channel wall ($T_w = 1400°C$).

Referring to the process of fuel ejection into the gaps between assemblies, we get from (3) $X_p = 32$ cm. This result is equivalent to the removal of 15% of the BOC core fuel inventory and 10% of the fuel from the EOC core. The reduced amount of fuel removed from the EOC core simply reflects the smaller gap spacing for this case.

Effect of Sodium on Flow of UO_2 in Gaps

The gaps between assemblies are interconnected and are filled with liquid sodium during normal operation. A small leakage flow from the inlet module is maintained through the lower assembly support plate structure. The sodium in the interassembly gaps flows to the upper plenum with the most restricted flow paths at the above core load pad (ACLP) locations*. The pressure in the gaps is approximately 1.5 bar which is the upper plenum pressure plus hydrostatic

*The frictional resistance to sodium flow in the interassembly gaps is negligible compared with the resistance to sodium flow at the ACLP.

head. The total area of the most restricted flow paths between the interstitial gaps and the upper plenum is roughly $A_{ACLP} \approx 600$ cm^2 with most of the area provided in the radial blanket/shield region.

In the initiating phase analysis, liquid sodium in the gaps is treated as a heat sink by increasing the thermal mass of the hexcan walls. At termination of the initiating phase analysis, the temperature of the fuel assembly hexcan walls with augmented thermal mass is calculated to be 900 to 1200°C in the core region. Therefore, the interassembly gaps are considered to be voided in the core region at initiation of the present melt-out phase analysis. However, the gaps below and outside the core region are not likely to be voided when molten fuel starts to flow in the gaps after melt-through of the fuel assembly. In Ref. D-1, it was concluded that the presence of liquid sodium in the gaps would not introduce significant, sustained fuel-coolant interaction pressurization to retard fuel removal from the core. This conclusion was based on first-principle arguments and supported by applicable experiments. It is shown here that the liquid sodium flow (impedance) to the upper plenum has little effect on fuel penetration into the gaps.

As the fuel flows from the active core region into the gaps, the liquid sodium displaced by the fuel produce a pressure drop at the ACLP locations of magnitude

$$\Delta P_{ACLP} = \frac{C_1}{2} \rho_{Na} u^2_{ACLP} \tag{4}$$

where C_1 is the effective drag or loss coefficient ($C_1 \approx 5.0$), ρ_{Na} is the density of liquid sodium, and u_{ACLP} is the sodium flow velocity through the ACLP. Assuming fuel crusts of instantaneous uniform thickness are left behind on the walls of the interassembly gaps penetrated by the fuel (conduction model), the pressure drop over the instantaneous fuel length X can be shown to be given by

$$\Delta P_{gap} = \frac{f}{2} \rho_{UO_2} u^2_{gap} \left(\frac{R_o}{R}\right)^3 \frac{X}{R_o} \tag{5}$$

where f is the friction factor for turbulent channel flow ($f \approx 0.005$), ρ_{UO_2} is the density of molten fuel, R_o is the gap half width (radius), R is the instantaneous "radial" location of the fuel crust-melt interface (measured from the channel centerline), and u_{gap} is the instantaneous fuel flow velocity in the gap.

Since the sodium volumetric displacement rate must equal the volumetric fuel escape rate from the core, we can write the equality

$$u_{gap} A_{core} = u_{ACLP} A_{ACLP} \tag{6}$$

where A_{core} is the gas cross-sectional area through which the fuel passes as it leaves the active core region. Eliminating u_{ACLP} in Eq. (4) in favor of u_{gap} via Eq. (6), adding the result to Eq. (5), and solving for $u_{gap} = dX/dt$ we get

$$\frac{dX}{dt} = \frac{[2\,\Delta P/(f\rho_{UO_2})]^{1/2}}{\left[\left(\frac{R_o}{R}\right)^3 \frac{X}{R_o} + \frac{C_1}{f}\frac{\rho_{Na}}{\rho_{UO_2}}\left(\frac{A_{core}}{A_{ACLP}}\right)^2\right]^{1/2}} \tag{7}$$

Since the fuel crust thickness, $R_o - R$, is related to time t through the familiar conduction-theory result

$$R_o - R = 2\lambda(\alpha_{UO_2} t)^{1/2} \tag{8}$$

where α_{UO_2} is the thermal diffusivity of the fuel and λ is the fuel crust growth constant ($\lambda \approx 0.9$), Eq. (7) can be transformed to

$$\frac{dX}{dR} = -\frac{B(1 - R/R_o)\,(R/R_o)^{3/2}}{\left[\frac{X}{R_o} + \frac{C}{f}\cdot\frac{\rho_{Na}}{\rho_{UO_2}}\cdot\left(\frac{A_{core}}{A_{ACLP}}\right)^2\left(\frac{R}{R_o}\right)^3\right]^{1/2}} \tag{9}$$

where B is defined as

$$B \equiv \frac{R_o}{2\lambda^2\alpha_s}\cdot\sqrt{\frac{2\Delta P}{f\rho_{UO_2}}} \tag{10}$$

The final fuel penetration length X_p is obtained by numerically integrating Eq. (9) in the negative R-direction from $R = R_o$ (open gap) when $X = 0$ to $R = 0$ (closed gap) when $X = X_p$.

In order to explore the effect of the sodium impedance on fuel penetration into the gaps, X_p has been plotted against the area for fuel escape, A_{core}, in Fig. D-2. The results shown are based on total fuel driving pressure $\Delta P = 1$ bar and a channel half-width $R_o = 0.2$ cm. The dashed curve in the figure corresponds to the fuel penetration length in the absence of liquid sodium. We note from the figure that even for A_{core} as large as 4000 cm^2, which is just about the maximum possible cross-sectional area for fuel escape from the core via the gaps between assemblies, the penetration length is reduced by only 40% by the sodium flow through the ACLP. The reason the fuel penetration length is rather insensitive to the sodium impedance is that in the conduction mode of freezing the penetration length is a weak function of the pressure drop ($X_p \sim \Delta P^{1/3}$). Interestingly enough, since the penetration length based on the bulk freezing model is practically independent of pressure drop (or flow velocity), we can anticipate an even smaller effect of sodium impedance on fuel penetration in this case.

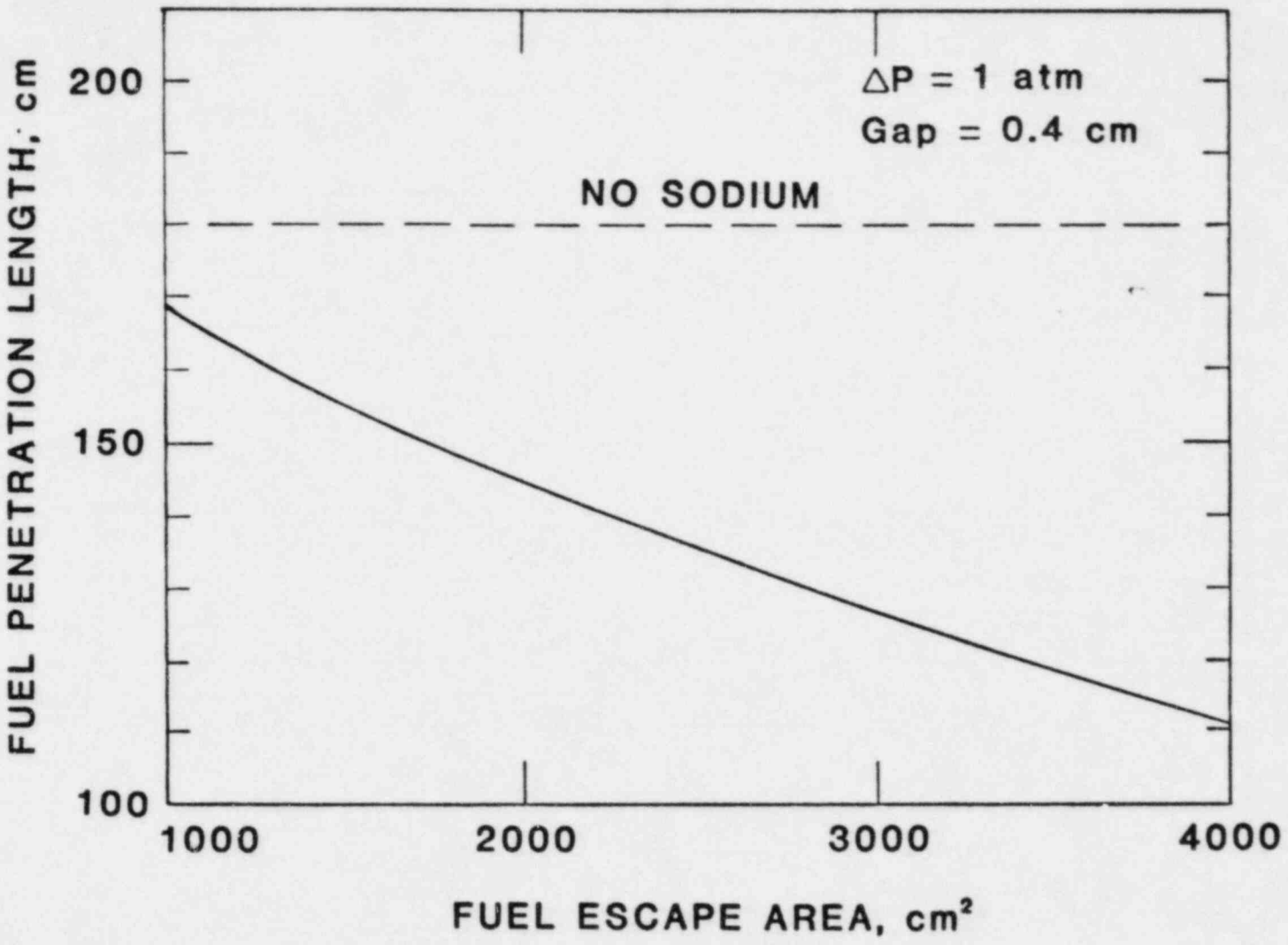

Fig. D-2 Fuel Penetration with Sodium Impedance Considered.

QCS760.178B5-D12

References

D-1 S. K. Rhow, et al., "An Assessment of HCDA Energetics in the CRBRP Heterogeneous Reactor Core," CRBRP-GEFR-00523, General Electric Company, December 1981.

D-2 R. W. Ostensen and J. F. Jackson, "Extended Fuel Motion Study," in Reactor Development Program Progress Report ANL-RDP-18, Argonne National Laboratory, pp. 7.4-7.7, July 1973.

D-3 M. Epstein, R. E. Henry, M. A. Grolmes, H. K. Fauske, G. T. Goldfuss, D. J. Quinn, and R. L. Roth, "Analytical and Experimental Studies of Transient Fuel Freezing," Proc. Int. Mtg. on Fast Reactor Safety and Related Physics, Vol. IV, USERDA Conf. No. 761001, October 5-8, Chicago, Illinois, pp. 1788-1798, 1976.

D-4 D. R. Armstrong, "Preliminary Results from 1st UO_2 Dropping Experiment," Private Communication, January 1970; (see also Fig. 3 in M. Epstein, M. A. Grolmes, R. E. Henry, and H. K. Fauske, "Transient Freezing of a Flowing Ceramic Fuel in a Steel Channel," Nucl. Sci. Eng., 61, pp. 310-323, 1976.

D-5 G. A. MacDonald, Volcanoes, Chapter 5, Prentice-Hall, Inc., Englewood Cliffs, New Jersey, 1972.

D-6 A. Yim, M. Epstein, S. G. Bankoff, G. A. Lambert, and G. M. Hauser, "Freezing-Melting Heat Transfer in a Tube Flow," Int. J. Heat Mass Transfer, 21 pp. 1185-1198, 1978.

D-7 D. W. Condiff and G. A. Lambert, Private Communication, 1978.

D-8 D. O. Lee, S. W. Eisenhawer, M. L. Corradini, and R. W. Ostensen, "Forced Convection Melting Heat Transfer in a Tube for a Two-Component System," AIChE Symposium Series, Vol. 75, pp. 55-68, 1979.

D-9 D. A. McArthur, R. W. Ostensen, and N. Hayden, "In-Core Transition-Phase Fuel-Freezing Experiment TRAN-1," Trans. Am. Nucl. Soc., Vol. 38, pp. 393-394, 1981.

D-10 D. A. McArthur, S. F. Duliere, and D. J. Sasmor, "Post-Test Analysis of TRAN-1 and TRAN-2 Final Fuel Distributions," Trans. Am. Nucl. Soc., Vol. 39, pp. 676-678, 1981.

D-11 D. A. McArthur, Private Communication.

D-12 W. D. Ford, H. K. Fauske, and S. G. Bankoff, "The Slug Expulsion of Freon-113 by Rapid Depressurization of a Vertical Tube," Intl. J. Heat Mass Transfer, Vol. 14, pp. 133-139, 1971.

D-13 M. A. Grolmes and G. A. Lambert, "Liquid Film Considerations for LMFBR Accident Analysis," Trans. Am. Nucl. Soc., Vol. 35, pp. 353-354, 1980.

D-14 G. I. Taylor, "The Instability of Liquid Surfaces when Accelerated in a Direction Perpendicular to Their Planes-I," Proc. Royal Soc. of London, Vol. A201, pp. 192-196, 1950.

D-15 M. Epstein, "Heat Conduction in the UO_2-Cladding Composite Body with Simultaneous Solidification and Melting," Nucl. Sci. Engng., Vol. 51, pp. 84-87, 1973.

D-16 M. Epstein, A. Yim, and F. B. Cheung, "Freezing Controlled Penetration of a Saturated Liquid into a Cold Tube," Trans. ASME J. Heat Transfer, Vol. 99, pp. 233-238, 1977.

D-17 G. A. Greene, D. C. Jones, Jr., and M. S. Kazimi, "Effects of Non-Condensable Void Fraction on Freezing of Flowing Fluids," Trans. Am. Nucl. Soc., Vol. 27, pp. 546-547, 1977.

D-18 G. A. Greene, D. C. Jones, Jr., M. S. Kazimi, T. Ginsberg, and J. J. Barry, "Anaysis and Measurement of Solidification Dynamics of Flowing Two-Phase Non-Condensable Mixtures," Trans. Am. Nucl. Soc., Vol. 28, pp. 465-466, 1978.

D-19 G. A. Greene, D. C. Jones, Jr., M. S. Kazimi, J. J. Barry, and G. A. Zimmer, "Two-Phase Transient Solidification Dynamics of Flowing Fluids with Non-Condensable Vapors," BNL-NUREG-24486R, 1978.

D-20 G. A. Greene and J. J. Barry, "Freezing of Multiphase Mixtures Flowing Downward in Circular Tubes," BNL-NUREG-28302, 1980.

D-21 D. J. Petrie, J. H. Linehan, M. Epstein, G. A. Lambert, and L. J. Stachyra, "Solidification in Two-Phase Flow," J. Heat Transfer, Vol. 102, pp. 784-786, 1980.

D-22 H. S. Carslaw and J. C. Jaeger, "Conduction of Heat in Solids, 2nd Edition, Clarendon Press, Oxford, 1959.

D-23 M. Epstein, et al., "Transient Solidification in Flow into a Rod Bundle," J. Heat Transfer, 102, No. 2, May 1980.

D-24 M. Epstein, M. A. Grolmes, R. E. Henry, and H. K. Fauske, "Transient Freezing of a Flowing Ceramic Fuel in a Steel Channel," Nucl. Sci. Engng., 61, pp. 310-323, 1976.

APPENDIX E TO: Question CS760.178B5, -C6, -C7

Sodium Re-Entry in the Presence of Steel Vapor Condensation

This Appendix considers the processes of vapor condensation in the presence of a second component subcooled volatile liquid in the context of a steel vapor sodium system. The distinctions between this system and a one-component system are drawn out and discussed relative to sodium re-entry in the CRBR safety evaluation.

The volatility of saturated or subcooled liquid sodium subjected to an oncoming stream of pure steel vapor is readily demonstrated by considering the thermal response of the surface of the liquid sodium. Immediately following liquid-vapor contact, the heating of the liquid sodium surface takes place via the kinetic rate of impact and deposition of steel vapor molecules upon the liquid, which form a condensed layer of steel separating the liquid sodium surface from the steel vapor phase. As the condensed steel layer grows, its temperature increases. Heat conduction through the condensed steel and the cold sodium begins to limit the condensation process as the surface temperature of the condensed liquid-steel layer approaches its vapor (boiling) temperature $T_{bp,ss}$. This kinetically controlled "preheating period" is estimated to be $b\bar{t} \approx 0.01$ μsec duration and leaves a steel condensate layer of ~ 0.1 μ thick on the liquid sodium surface. During the preheating period, the liquid sodium-condensed steel interface temperature rises from its initial temperature, T_o, and approaches a constant maximum value, T_i, when the condensation process becomes conduction limited. If T_i lies below the boiling temperature of liquid sodium, $T_{bp,Na}$, the steel condensation process will continue on the cold liquid sodium surface after the transition from kinetically controlled to conduction controlled condensation is made. This condition would result in the rapid depressurization of the steel vapor region and sodium re-entry into the core. Alternatively, if $T_i > T_{bp,Na}$, the liquid sodium just behind the thickening steel condensate layer will reach its boiling point during the preheating period, become slightly superheated and burst the steel layer. At this point in time sodium vaporization will begin and "fill" the void left by the condensing steel (see below).

In order to determine T_i, we consider the problem in which the region $x > 0$ initially contains liquid sodium at temperature T_o. The region $x < 0$ initially contains steel vapor at its boiling temperature $T_{bp,ss}$. Condensation of the steel vapor starts at the plane $x = 0$ and moves to the left into the steel vapor region. An approximate solution for the interface temperature T_i can be obtained by neglecting the transient term in solving the conduction equation in the steel condensate layer, so that the temperature distribution T_{ss} in this region is approximately that corresponding to steady state, that is

$$T_{ss} = T_i + x(T_i - T_{bp,ss})/\delta(t) \qquad (1)$$

where $x = -\delta(t)$ is the surface of separation of the vapor and liquid steel phases.

We impose the energy balance which equates the instantaneous latent heat of steel condensation to the conductive heat loss to the steel condensate layer:

$$\rho_{ss} L_{ss} \frac{d\delta}{dt} = - k_{ss}\left(\frac{\partial T_{ss}}{\partial x}\right)_{x=-\delta} \tag{2}$$

where ρ_{ss}, L_{ss} and k_{ss} are the liquid density, latent heat of condensation, and liquid thermal conductivity of steel, respectively. Heat flux continuity at x = 0 requires that

$$k_{ss}\left(\frac{\partial T_{ss}}{\partial x}\right)_{x=0} = k_{Na}\left(\frac{\delta T_{Na}}{\partial x}\right)_{x=0} = - \frac{k_{Na}(T_i - T_o)}{\sqrt{\pi \alpha_{Na} t}} \tag{3}$$

where α is thermal diffusivity, t is time and the subscript Na refers to the properties of the liquid sodium. The right-hand term in Eq. (3) follows from the fact that the liquid sodium region may be considered to extend to infinity in the positive x-direction; it is the flux of heat at the surface of a semi-infinite medium. Substituting Eq. (1) into Eqs. (2) and (3), the following system of equations is obtained.

$$\rho_{ss} L_{ss} \frac{d\delta}{dt} = - \frac{k_{ss}(T_i - T_{bp,ss})}{\delta} \tag{4}$$

$$\frac{k_{ss}(T_i - T_{bp,ss})}{\delta} = - \frac{k_{Na}(T_i - T_o)}{\sqrt{\pi \alpha_{Na} t}} \tag{5}$$

Integrating Eq. (4) and substituting the result for $\delta(t)$ into Eq. (5) gives the steel condensate-liquid sodium interface temperature

$$\frac{T_i - T_o}{T_{bp,ss} - T_o} = \frac{(1 + 4A)^{1/2} - 1}{2A} \tag{6}$$

where

$$A \equiv \frac{2}{\pi} \frac{(k\rho c)_{Na}}{(k\rho c)_{ss}} \cdot \frac{c_{ss}(T_{bp,ss} - T_o)}{L_{ss}} \tag{7}$$

Equation (7) is valid for thick thermal boundary layers in the condensate layer or, equivalently, when $c_{ss}(T_{bp,ss} - T_i)/L_{ss} << 1.0$. Fortunately, for the steel-sodium system treated here this inequality is always satisfied. Moreover, the parameter A is also a small quantity for the steel-sodium material pair so the Eq. (4) can be simplified by expanding the square-root term to obtain the final result.

$$\frac{T_i - T_o}{T_{bp,ss} - T_o} = 1 - A \tag{8}$$

Using Eq. (8), it is of interest to calculate the temperature T_i that would result from the filmwise condensation of steel vapor onto a liquid sodium surface at T_o = 500°C (subcooling ≈ 400°C). For this system A = 0.07 and from Eq. (8) we estimate T_i = 2640°C. Not only does the interface temperature exceed the sodium boiling point (∿ 900°C) but it exceeds its critical temperature (∿ 2784°C) as well. It is clear that under these conditions the foregoing analysis is inapplicable and that steel condensation without sodium vaporization is impossible.

It is interesting to note that sustained sodium vaporization in nearly pure steel vapor is also impossible. To demonstrate this let us suppose that liquid sodium can vaporize into pure hot steel vapor. The sum of the steel vapor partial pressure and the sodium vapor partial pressure at the liquid-vapor interface must equal the total system pressure (the steel vapor pressure far from the interface):

$$P = P_{ss} + P_{sat,Na}(T_i) \tag{9}$$

where P is the total pressure and is constant, P_{ss} is the partial pressure of steel vapor and $P_{sat,Na}(T_i)$ is the equilibrium partial pressure of sodium vapor and is strictly a function of the interface (sodium surface) temperature. We now ask the following question: How low can the liquid sodium surface temperature be before sustained sodium vaporization becomes impossible? This threshold temperature, T_i^*, should be the dew point temperature for steel vapor at the liquid sodium surface, defined by the condition $P_{sat,ss}(T_i^*) = P_{ss}$ where subscript sat,ss refers to the equilibrium partial pressure for steel vapor. If the steel vapor pressure at the sodium surface exceeds $P_{sat,ss}$ condensation of vapor on the liquid sodium surface will occur and sodium vaporization must terminate. This reasoning leads to an implicit relation between T_i^*, and the system pressure*:

$$P_{sat,ss}(T_i^*) + P_{sat,Na}(T_i^*) = P \tag{10}$$

Equation (10) reveals that sustained sodium vaporization is impossible when the liquid sodium-steel vapor interface temperature drops slightly below the sodium boiling point (by much less than 1°C) at the system P. Even accounting for the fact that radiation from "white-hot" steel fog particles will be the predominant form of energy transfer on the steel vapor side of the interface, because of the initial, highly subcooled state of liquid sodium at, say, 500°C. The energy requirements for maintaining the liquid sodium surface at its boiling temperature cannot be met. Thus, sufficient quantities of steel vapor will reach the liquid sodium surface such that steel condensation

*The essential difference between a two-component and a one-component system is that there is only one partial pressure interface temperature relation which determines whether the energy exchange leads to condensation or evaporation. Furthermore, in a one-component system phase change in only one direction is permissible.

upon the sodium surface will occur. The condensed steel will probably form "steel frost" on the surface, since the steel vapor temperature must fall below its triple point temperature (sublimation) as it diffuses through sodium vapor toward the vaporizing liquid surface. If the frost layer is sufficiently porous, stable counter-diffusion of steel and sodium vapor at uniform total pressure will occur. Alternatively, the liquid sodium surface may become unstable with respect to vaporization, frequently becoming superheated and shattering any condensed steel layer that tends to form on its surface, resulting in surface temperatures that oscillate about the sodium boiling point.

Regardless of the precise mechanism of energy exchange between hot steel vapor and subcooled sodium, it is clear that sodium evaporation must accompany steel vapor condensation. A simple energy balance reveals that this dual phase conversion process results in a vapor volume increase at constant pressure. For every 1.0 cm^3 of steel vapor condensed, 1.3 cm^3 of sodium vapor is produced from subcooled sodium at T_o = 500°C. In summary sodium re-entry into the core by rapid steel vapor depressurization is prevented by sodium vaporization.

Question CS760.178D8

What is your estimate of the force required to produce a mechanically induced relief path via upper internals structures displacement?

Response

Forces of structural significance to the upper internals structure (UIS) can only be produced by an energetic core disassembly, which is a very low probability event in the CRBRP. The Project approach to provide for structural margin beyond the design base (SMBDB) is presented in detail in Ref. QCS760.178D8-1. In summary, an extreme core temperature condition was chosen to both provide a substantial margin for the expected nonenergetic outcome of an HCDA, and to accommodate a large degree of uncertainty and conservatism (including potential work augmentation by sodium) for generic HCDA consequences. Included in the approach was the selection of a fuel isentropic expansion calculation for the thermal-to-mechanical energy conversion process. The UIS has been shown in scale model tests to accommodate the forces which result from the SMBDB specification without major deformation of the support columns, although limited buckling was observed (Ref. 760.178D8-1).

In direct response to the question an assessment of the forces required to significantly displace the UIS has been performed.

Based upon a finite element analysis (ANSYS computer program) of the UIS support columns and a failure mode due to plastic hinging, an estimated static force of 2.90×10^7 N (6.52×10^6 lbf) would be required to cause buckling and collapse of all four columns, producing a relief path via significant UIS displacement. The following assumptions were made in obtaining this force: (1) a column temperature of 538°C (1000°F), (2) average column dimensions of 30.5 cm id and 2.54 cm (1 in.) wall thickness, (3) a typical yield stress of 1.47×10^8 N/m^2 (1.25 times the minimum) Ref. QCS760.178D8-2, and (4) the UIS motion limited to the axial direction. The UIS is laterally restrained until key disengagement occurs at a displacement of 18.8 cm.

One way to help characterize the above force required to buckle the UIS columns is to assume that all of the above core structural flow paths are blocked, and that the structure is lifted up against the bottom of the UIS by a uniform core pressure. For this assumed configuration, the required pressure is calculated to be approximately 91 atm.

The ANSYS model utilizes plastic pipe elements for the support columns and elastic shell elements for the UIS structure. The columns are modeled with a slight initial deformation, which in combination with the geometry updating procedure allows column buckling to be analyzed. Figure QCS760.178D8-1 shows the resulting estimate of vertical force on the UIS versus vertical displacement. This result utilized a minimum yield stress of 1.17×10^8 N/m^2 and resulted in a maximum axial load of 2.32×10^7 N where column buckling occurred. Assuming a maximum value for the yield stress (Ref. QCS760.178D8-3), a maximum axial load of 5.03×10^7 N is expected when column buckling would occur. Figure QCS760.178D8-2 provides the bilinear stress-strain relationship used for 316 SS at 538°C in the ANSYS model. The bilinear curve is very good for strains below 0.05 and within 15% of expected values (Ref. QCS760.178D8-1) for strains below 0.10. Hence, a force of approximately

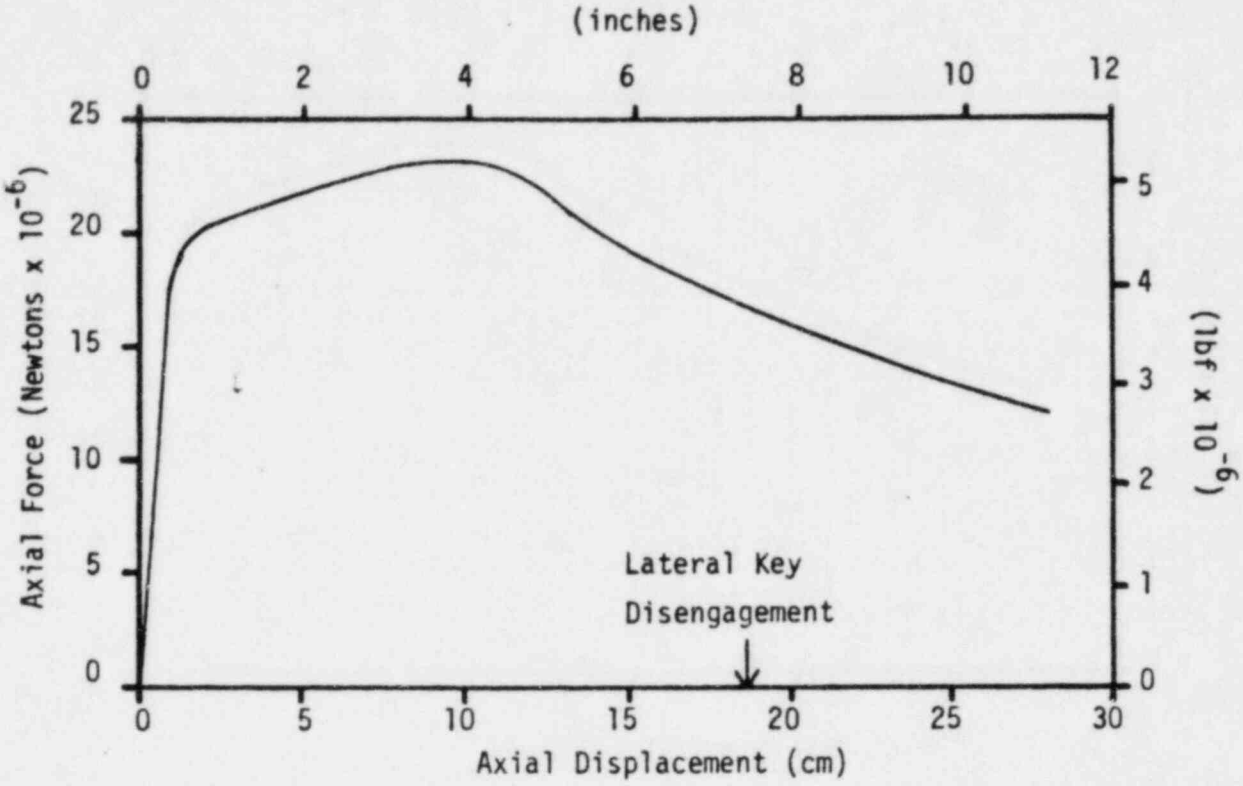

Fig. QCS760.178D8-1 Axial Force vs. UIS Axial Displacement.

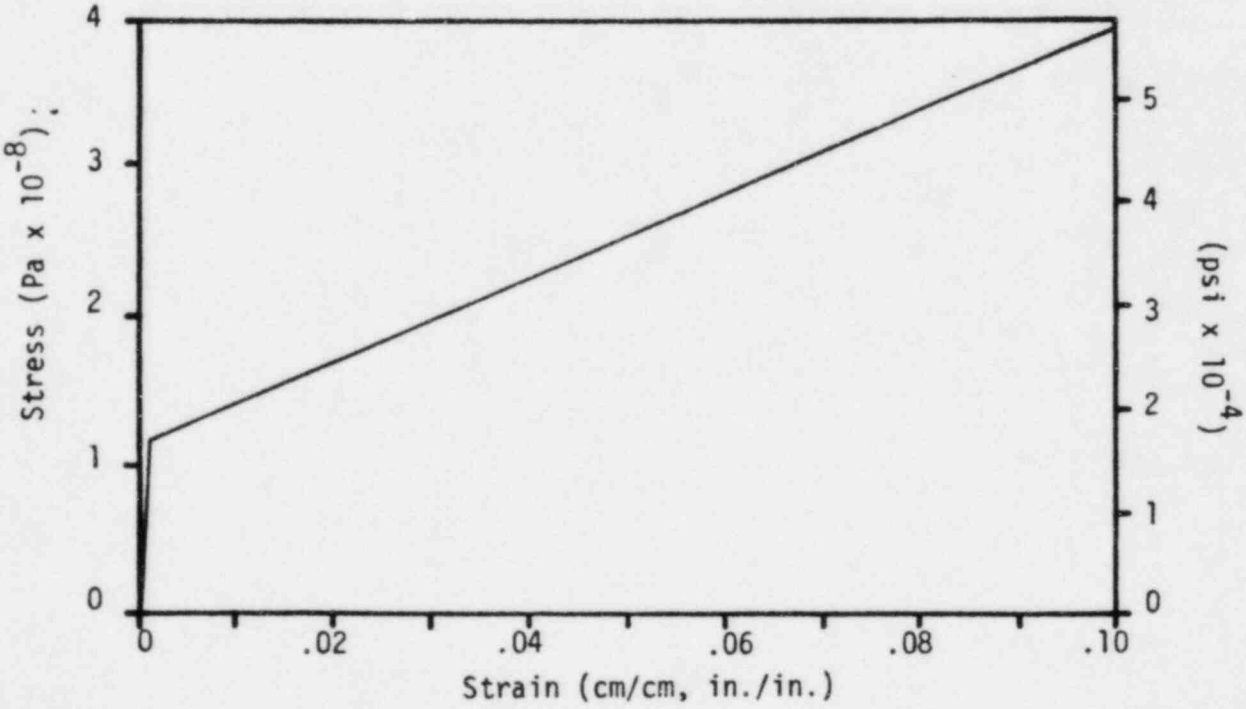

Fig. QCS760.178D8-2 Stress vs. Strain for 316 SS Used in Analysis.

2.7×10^7 N would cause gross upward displacement of the UIS. As stated previously, such large forces would be extremely unlikely in the CRBRP, even under HCDA considerations. The analysis and judgement which support the position that the defined SMBDB core thermal conditions envelope a very large range of uncertainty and conservatism in evaluating core behavior are presented in Ref. QCS760.178D-1. In addition, the choice of a core fuel isentropic expansion process to calculate the resulting structural loads contains further margin relative to real processes. The remainder of the response to this question provides the project basis which support the position that the estimate of the post-disassembly expansion (PDE) structural loads based on the assumption of an isentropic expansion of the fuel is conservative.

Studies, both experimental and analytical, have shown that non-isentropic hydrodynamic and heat transfer processes play a net mitigating role. The combined effect of the non-isentropic processes is to produce a work energy that is substantially lower than the isentropic value. The major non-isentropic processes are:

1. Fuel self-mixing.
2. Non-uniform bubble expansion.
3. Hydrodynamic effects of the UIS.
4. Heat transfer to sodium.
5. Heat transfer to structures.

These processes are discussed below, including a discussion of the supporting experimental and/or analytical evidence. All of these processes have been clearly shown to be mitigating in nature except for heat transfer to sodium which has the potential for work augmentation. The actual sodium work augmentation however, is considered to be negligibly small for expected CRBRP PDE conditions, and in the limit can be bounded via thermodynamic considerations.

1. Fuel Self-Mixing: The pressure gradients in the core and in the expanding bubble cause the higher temperature fuel to accelerate toward the colder fuel. The resulting mixing produces a net heat loss from the hot fuel to the cold fuel, thus reducing the temperature of the hot fuel. Since the fuel vapor pressure is an exponential function of the temperature and steep, local temperature gradients exist in the core, self-mixing has the effect of reducing the core pressurization, and therefore the mechanical loading on the vessel structures. The mitigating consequence of fuel self-mixing for the CRBRP PDE, although clearly based on physical principle and understanding, has not been currently quantified and substantiated for CRBRP. An analytical study did estimate the effect as a 15% to 35% reduction of isentropic potential due to axial or combined axial-radial self-mixing in the homogeneous core (Ref. QCS760.178D8-4).

2. Non-Uniform Expansion: The pressure gradients in the core, and the resultant pressure gradients inside the expanding two-phase bubble, cause the force acting on the sodium pool to be less than if all the fuel vapor was uniformly participating in accelerating the pool. In other words, the relatively low pressure fuel vapor near the

bubble/pool interface dominates the pool acceleration, while the higher pressure fuel vapor farther away from the interface plays a much smaller role in the pool acceleration, and therefore in the subsequent sodium slug impact on the vessel head. Also, vortexing occurs at the bubble/pool interface, which is dissipative.

The mitigating effects of non-uniform expansion were verified experimentally in Purdue University and SRI International nitrogen expansion tests (Refs. QCS760.178D8-5 and -6). These tests employed simple scaled-down models of the CRBRP vessel. The high pressure nitrogen was initially at room temperature. It was released into a water pool containing no structures at the start of the test. Both tests confirmed that the expansion work was substantially less (30%-40%) than the isentropic value. The reduction is attributed primarily to non-uniform expansion of the nitrogen, and to the compression of the cover gas. The non-uniformity in the bubble expansion for the CRBRP would be even greater due to the pressure gradients existing in the core, whereas the nitrogen expansion tests started with a uniform pressure of the nitrogen source.

Analysis of the Purdue tests using straightforward analytical models derived from basic hydrodynamic principles (Ref. QCS760.178D8-5) showed good predictability of the test results, and verified the mitigating role of non-uniform bubble expansion. Analysis of the SRI tests using the more complex SIMMER-II code (Ref. QCS 760.178D8-5) also confirmed the basic effect of non-uniform expansion.

3. Hydrodynamic Effects of UIS: The presence of the UIS alters the expansion of the bubble hydrodynamically by: (a) laterally diverting the flow beneath it, (b) throttling of the flow, and (c) impeding the fluid flow through friction. The lateral diversion of fluid flow (Item a) produces turbulence and vortexing that consumes energy without contributing to the acceleration of the pool and subsequent mechanical loading on the vessel head. This mechanism is very effective in reducing the PDE work energy. Throttling of the flow through the UIS (Items b and c) causes the expansion of the bubble to slow down and to act on a smaller mass of the pool (sodium above the UIS), with approximately the same acceleration as when the UIS is absent, such that the impact loading on the vessel head is reduced.

The hydrodynamic effects of the UIS have been experimentally confirmed via the previously referenced Purdue and SRI programs. Straightforward analyses of the bubble expansion in the presence of the UIS (Ref. QCS760.178D8-8) have verified a correct understanding of the basic flow effects. Again, the more complex analyses of the SRI experiments with SIMMER further substantiate the significant role of the UIS in reducing the isentropic work potential; analytically estimated as a 50% reduction for CRBRP geometries.

4. Heat Transfer to Sodium: This is the only mechanism identified as having a potential for significant augmentation of the PDE work energy relative to the isentropic expansion case. The thermal

interaction between fuel and sodium produces a mitigating factor; the cooling of the fuel due to net heat loss to sodium, and an augmenting factor; the vaporization of liquid sodium which increases the bubble pressure. The trade-off between the two factors is dependent on the relative masses of the sodium and fuel, the fuel temperature, and the compliant space available for component separation. As discussed in Ref. QCS760.178D8-9, Section 8.2.6, the preponderance of experimental evidence supports a benign or mitigating role for the sodium. Two contact modes of importance are the ejection of fuel from rods into sodium within fuel assembly geometry, and the entrainment of sodium into an expanding fuel bubble in the upper vessel sodium pool.

The highest fuel energy tests relevant to the first mode were the TREAT S-11, S-12 and Sandia PBE series, of which PBE-5S and -9S have been reviewed in additional detail. As discussed in the above reference, care must be used when interpreting energy conversion efficiencies in these limited compliance volume autoclave tests. Of the above tests, only PBE-9S reported a significant pressurization event after piston stoppage (i.e., constant volume system), which was interpreted by some as a pressure wave induced fragmentation FCI. However, the interpretation, stated in Ref. QCS760.178D8-9, is that the pressurization resulted from the constant volume enforced mixing and heating.

Some comparisons will help to illustrate this point. The specific sodium mass (defined as the mass of sodium per fuel mass) which is a measure of overall quenching potential has a value of 5 and 0.1 for tests S-11 and PBE-9S. Another comparison is offered by the specific displacement (defined as the compliant volume per fuel mass) which is a measure of the sodium ability to disengage from the hot liquid fuel. The S-11 and PBE-9S values are 1.2 and 0.25 while the corresponding CRBRP value is 3. These comparisons serve to demonstrate that the PBE-9S experiment was, relative to S-11 and CRBRP, an extremely constrained environment which strongly affects the potential for system pressurization. The more compliant S-11 experiment conditions, which are much closer to the CRBRP, resulted in substantially reduced work potential.

Based upon both simulant and real materials experiments wherein thermite produced high temperature fuel was injected into sodium pools (Ref. QCS760.178D8-10) no augmentation of fuel isentropic work potential is expected by sodium entrainment into an expanding fuel bubble. Additionally, the maximum effect of this augmentation process can be limited to a factor of two based on thermodynamic considerations (Ref. QCS760.178D8-11).

Heat Transfer to Structures: The UIS and above-core structure will have a substantial mitigation effect on the core work potential due to the net energy loss from the fuel and its synergistic effect on fuel self-mixing in the core. However, the non-isentropic mitigation role of the heat transfer mechanisms is currently less amenable to quantify and substantiate as compared to the hydrodynamic effects for the CRBRP.

In summary, non-isentropic processes during the post-disassembly expansion will produce a substantial reduction in the work energy from the isentropic value. Although a potential has been indicated for sodium to augment the fuel expansion work, it would be outweighed by the many demonstrated mitigation processes and be enveloped by the Project selection of an isentropic process. The net reduction is conservatively estimated to be at least 35% to 70%, based on only consideration of major contributing processes which can reasonably be quantified by analysis and/or experiments. Hence, the SMBDB specified forces on the UIS and other primary heat transport system components are considered appropriately conservative.

References

QCS760.178D8-1 "Hypothetical Core Disruptive Accident Consideration in CRBRP; Energetics and Structural Margin Beyond the Design Base," CRBRP-3, Vol. 1.

QCS760.178D8-2 Nuclear Systems Materials Handbook, Volume 1, Book 1 Property Code 2107 for 304 SS, Rev. 2, 12/74.

QCS760.178D8-3 Aerospace Structural Metals Handbook, Syracuse University Research Institute, March 1963.

QCS760.178D8-4 Nuclear Reactor Safety, Quarterly Progress Report, July-September, 1977, Los Alamos Scientific Laboratory, p. 24, LA-7039-PR, January 1978.

QCS760.178D8-5 J. Simpson, M. Saito, and T. G. Theofanous, "The Termination Phase of Core Disruptive Accidents in LMFBRs, 1980 Annual Report," Purdue University, PNE-81-151, June 1981.

QCS760.178D8-6 R. J. Tobin and D. J. Cagliostro, "Effects of Vessel Internal Structures on Simulated HCDA Bubble Expansions," SRI International, Technical Report No. 5, November 1978.

QCS760.178D8-7 T. F. Bott and C. R. Bell, "SIMMER Analysis of SRI Post-Disassembly Expansion Experiments," Los Alamos National Laboratory Report LA-9452-MS, June 1982.

QCS760.178D8-8 A. M. Christie, "Low Risk Energetics Definition for Design Application," WARD-SR-94000-23, September 1981.

QCS760.178D8-9 S. K. Rhow, et al., "An Assessment of HCDA Energetics in the CRBRP Heterogeneous Reactor Core,"CRRP-GEFR-00523, General Electric Company, December 1981.

QCS760.178D8-10 R. E. Henry, et al., "Large Scale Vapor Explosions," Proc. Fast Reactor Safety Meeting, p. 922, Beverly Hills, California, April 1974.

QCS760.178D8-11 D. H. Cho and M. Epstein, "Work Potential from a Mechanical Disassembly at the Voided FFTF Core," Argonne National Laboratory, ANL/RAS 74-17, August 1974.

Question CS760.179

Dimensioned design layout drawings are required by the staff and its consultants to provide an accurate basis for the geometries used in analysis of hypothetical core disruptive accident energetics. Please provide design layout drawings, including dimensions, materials and weldments, for all the components and structures in the reactor vessel including:

a) fuel, blanket, control and removable radial shield assemblies;

b) the upper internal structure and all its components;

c) the core support plate and all its components;

d) the reactor vessel inlet plenum, including the inlet piping and core support cone;

e) the core barrel, the core formal rings, the fixed radial shielding, the horizontal baffle, the fuel transfer and storage assembly (FT&SA) the bypass flow modules, the reactor vessel thermal liner, and any component or structure connected to the core barrel; and

f) the reactor closure head, with its 3 rotating plugs, including the reactor vessel walls, the reacor vessel thermal liner, the gas intrainment suppressor plate, the thermal and radiological shielding plates, the upper internal structure (UIS) jacking mechanisms, the liquid level monitor plugs, the vessel flange, the riser assemblies (inner and outer for all plugs), the riser dip seals, the riser elastomer seals, any component or structure conncted to the reactor closure head, and all penetrations thereof.

Response

The requested design layout drawings have been supplied under separate cover in Reference QCS760.179-1.

References

QCS760.179-1. Letter HQ:S:82:085, J. Longenecker (DOE) to P. Check (NRC), "Transmittal of Information", dated August 20, 1982.

LIST OF DRAWINGS PROVIDED IN RESPONSE TO QUESTION CS760.179

Drawing No.	Rev.	Title
138J501	4	Upper Control Rod Drive Mechanism Design Layout
138J502	4	Lower Control Rod Drive Mechanism Design Layout
138J503	4	Lower Control Rod Drive Design Layout
273R225	17	Secondary Control Rod System Design Layout
766J611	12	Primary Heat Transport System Design Layout
766J613	44	Reactor Closure Head Small Rotating Plug
766J614	78	Reactor Closure Head Intermediate Rotating Plug
766J615	77	Reactor Closure Head Large Rotating Plug
766J616	22	Reactor Closure Head Arrangement
766J648	15	Upper Internals Structure Design Layout
766J653	2	Core Support Structure Module Liner Design Layout
766J662	13	Bypass Flow Module Design Layout
766J667	12	Lower Inlet Module Layout
766J681	12	Core Former Structure Design Layout
766J688	12	Primary Control Assembly Design Layout
766J689	11	Radial Blanket Assembly Design Layout
766J697	9	Fuel Assembly Design Layout
766J723	4	Removable Radial Shield Design Layout
766J839	3	Inner Blanket Assembly Design Layout
1182E31	78	Reactor Vessel Design Layout
1182E55	6	Core Support Structure Design Layout
1182E86	4	Fuel Rod Design Layout
1183E16	82	Riser Design Layout
1183E25	5	Radial Blanket Rod Assembly Design Layout
1184E21	7	Fixed Radial Shield Design Layout
1184E56	13	Horizontal Baffle Assembly Design Layout
1535E45	21	Reactor Closure Head Assembly